Low-Cost Micromechanically Tunable Optical Devices: Strained Resonator Engineering, Technological Implementation and Characterization

Vom Fachbereich Elektrotechnik / Informatik
der Universität Kassel
zur Erlangung der Würde eines
Doctor-Ingenieurs (Dr.-Ing.)
genehmigte

Dissertation

von

Dipl.-Ing. Amer Tarraf

Kassel, im November 2005

Doctoral adviser	Prof. Dr. rer. nat. H. Hillmer
Referee	Prof. Dr. rer. nat. H. Hillmer
Co-Referee	Prof. Dr. -Ing. P. Meißner

Examiners	Prof. Dr. rer nat. H. Hillmer
	Prof. Dr. -Ing. P. Meißner
	Prof. Dr. -Ing. S. Hentschke
	Prof. Dr. -Ing A. Zündorf

Day of defense: 30.11.2005

For my mother Mantoura
and my father Antoine

Danksagung

Ich möchte mich ganz herzlich bei Herrn Prof. Dr. rer. nat. Hartmut Hillmer für die Themenstellung und die Betreuung dieser Arbeit bedanken. Weiterhin bedanke ich mich bei ihm für sein Engagement, die Schaffung der notwendigen Arbeitsvoraussetzungen und sein stets förderndes Interesse.

Herrn Prof. Dr. -Ing. Peter Meißner danke ich für die fruchtbare Kooperation zwischen dem INA und der Technischen Universität Darmstadt, sowie für die Referierung meiner Arbeit und die wissenschaftliche Unterstützung. Den Mitarbeitern seines Institutes, Herrn Frank Riemenschneider und Herrn Hubert Halbritter danke ich ebenfalls.

Mein weiterer Dank gilt Prof. Dr. rer. nat. Rainer Kassing für seine wissenschaftlichen Hilfestellungen und seine persönliche Unterstützung.

Ohne die tatkräftige Unterstützung aus dem Technikbereich und dem Sekretariat des INA, den Damen Heike Schröter-Hohmann, Ina Kommallein und Ina Wensch, sowie den Herren Dietmar Gutermuth, Albert Malkomes, Michael Plätzer und Dirk Albert, wäre die Durchführung meiner Experimente und die Anfertigung dieser Arbeit nicht möglich gewesen. Ihnen allen gebührt mein besonderer Dank.

Meinen Kollegen und Freunden Dr. -Ing. Jürgen Daleiden, Sören Irmer und Friedhard Römer danke ich für zahllose fruchtbare Diskussionen, fachliche Unterstützung und Hilfestellung bei der Durchführung von Experimenten.

Dr. -Ing. Martin Strassner unterstützte mich durch Überlassung von Probenmaterial und Einweisung in Fertigungsprozesse.

Weiterhin möchte ich mich bei Herrn Prof. Dr. rer. nat. Josef Salbeck und seiner Forschungsgruppe für die Zusammenarbeit bedanken. Namentlich möchte ich Herrn Dr. rer. nat. Fuhrmann-Lieker und Herrn Till Spehr erwähnen.

Mein Dank gilt Herrn Ludwig Söhngen, der mir bei der Aufnahme meines Studiums in Deutschland und bis heute stets zur Seite stand.

Mein ganz besonderer Dank gilt meiner verstorbenen Mutter Mantoura, die mich im Verlauf dieser Promotionsarbeit sicher oft vermisst hat, sowie meinem Vater Antoine, der mir immer zur Seite stand und mich unterstützte.

Abstract

The rapid growth of the optical communication branches and the enormous demand for more bandwidth require novel networks such as dense wavelength division multiplexing (DWDM). These networks enable higher bitrate transmission using the existing optical fibers.
Micromechanically tunable optical microcavity devices like VCSELs, Fabry-Pérot filters and photodetectors are core components of these novel DWDM systems. Several air-gap based tunable devices were successfully implemented in the last years. Even though these concepts are very promising, two main disadvantages are still remaining. On the one hand, the high fabrication and integration cost and on the other hand the undesired adverse buckling of the suspended membranes.
This thesis addresses these two problems and consists of two main parts:

- PECVD dielectric material investigation and stress control resulting in membranes shape engineering.
- Implementation and characterization of novel tunable optical devices with tailored shapes of the suspended membranes.

For this purposes, low-cost PECVD technology is investigated and developed in detail. The macro- and microstress of silicon nitride and silicon dioxide are controlled over a wide range.
Furthermore, the effect of stress on the optical and mechanical properties of the suspended membranes and on the microcavities is evaluated. Various membrane shapes (concave, convex and planar) with several radii of curvature are fabricated. Using this resonator shape engineering, microcavity devices such as non tunable and tunable Fabry-Pérot filters, VCSELs and PIN photodetectors are succesfully implemented. The fabricated Fabry-Pérot filters cover a spectral range of over 200 nm and show resonance linewidths down to 1.5 nm.
By varying the stress distribution across the vertical direction within a DBR, the shape and the radius of curvature of the top membrane are explicitely tailored. By adjusting the incoming light beam waist to the curvature, the fundamental resonant mode is supported and the higher order ones are suppressed. For instance, a tunable VCSEL with 26 nm tuning range, $400\mu W$ maximal output power, 47 nm free spectral range and over 57 dB side mode suppresion ratio (SMSR) is demonstrated.
Other technologies, such as introducing light emitting organic materials in microcavities are also investigated.

Zusammenfassung

Die faseroptische Datenübertragung hat sich als äußerst vielversprechendes Verfahren erwiesen, um den steigenden Ansprüchen der sich rasant entwickelnden Informationstechnik gerecht zu werden. Dies trifft besonders auf die Übertragungsbandbreite und -bitrate zu. Die Übertragungsbandbreite des bereits vorhandenen Einkanalsystems reicht jedoch nicht aus, um den steigenden Bedarf an Datenübertragung zu decken. Die Wellenlängenmultiplextechnik (engl. dense wavelength division multiplexing, DWDM) ermöglicht eine Erhöhung der Übertragungskapazität dieser Faserstrecken, ohne dass zusätzliche Faserverlegungen notwendig sind.

Für neuartige DWDM-Systeme bieten abstimmbare vertikale mikro -opto -elektro -mechanische (engl. micro-opto-electro-mechanical, MOEM) Bauelemente entscheidende Vorteile. Zu diesen Bauelementen zählen auf der Sendeseite Vertikalresonator emittierende Luftspalt-Laser (engl. air-gap vertical cavity surface emitting laser, VCSEL) und empfängerseitig Luftspalt-Filter und Luftspalt-Photodetektoren (engl. air-gap filter, air-gap receiver).

Herkömmliche kantenemittierende Laserdioden weisen Chip-Faser Koppelverluste und eine große Divergenz des austretenden Lichts auf. Oberflächenemittierende Mikrolaser mit vertikalem Resonator (VCSEL) ermöglichen demgegenüber eine verbesserte Koppeleffizienz in eine Glasfaser durch geringere Divergenz, symmetrische Modenprofile und eine flexible laterale Strukturierung der Austrittsfläche des Lasers. Im Einsatz befindliche DWDM-Systeme benötigen bis zu 80 Laserdioden mit unterschiedlichen Trägerwellenlängen auf der Sendeseite und ebenso viele Photodetektoren auf der Empfangsseite. Für diese DWDM-Netze werden abstimmbare Bauelemente benötigt, um auf die Ausfälle einzelner Kanäle flexibel reagieren zu können. Die Abstimmung der Laserdioden und Filter erfolgt in dem in dieser Arbeit verfolgten Konzept durch eine Änderung der Resonatorlänge, realisiert durch thermische oder kapazitive mikromechanische Aktuation einer der beiden Resonatorspiegel.

Obwohl dieses Konzept erhebliche Vorteile in sich bringt, ist die Serienfertigung solcher Bauelemente bislang immer noch eine technologische, wissenschaftliche und finanzielle Herausforderung. Ein Schlüsselaspekt ist dabei die gezielte Einstellung optischer und mechanischer Eigenschaften aktuierbarer Bragg-Reflektoren. Dabei wird die Krümmung der beweglichen Membran gezielt durch eine Verspannung der einzelnen Bragg-Schichten eingestellt. Dies geschieht, ohne die optischen Eigenschaften des Bauele-

mentes negativ zu beeinflussen. Die Entwicklung einer kostengünstigen Implementierungstechnologie ist ebenso eine notwendige Voraussetzung für eine erfolgreiche Serienfertigung.

Die vorliegende Arbeit befasst sich mit dieser Problematik und bearbeitet systematisch zwei Themenbereiche:

- Die Untersuchung der Verspannung und deren Einfluss auf die Membrankrümmung und darausfolgend auf die optischen Eigenschaften des Resonators.
- Die Herstellung und Charakterisierung von mikromechanisch abstimmbaren Bauelementen durch eine gezielte Stresseinstellung der oberen Membran.

Zunächst untersucht die vorliegende Arbeit das plasmaunterstützte Abscheideverfahren (engl. plasma enhanced chemical vapor deposition, PECVD) und diskutiert die daraus resultierenden Ergebnisse. Die Abscheidung beeinflussende Parameter, wie Gasfluss, Druck, Temperatur, etc. besitzen einen starken Einfluss auf die optischen Eigenschaften (Brechungsindex und Absorption), jedoch kaum auf die Verspannung.

Durch eine Modulation der Plasmaanregungsfrequenzen des Abscheideverfahrens kann hingegen eine gezielte Verspannungseinstellung der dielektrischen Bragg-Schichten erreicht werden. Die Untersuchung dieser Verspannung erfolgte parallel mit einem Verfahren, das die Verspannung im makroskopischen Bereich erfasst sowie mit einer Methode, die die Mikroverspannung analysiert.

Die Makroverspannung ergibt sich jeweils aus der Messung der Krümmung vor und nach der Beschichtung eines Wafers. Daraus resultiert eine Kenngröße, welche über die gesamte Länge entlang einer Richtung auf dem Wafer gemittelt wird. Diese Methode erlaubt allerdings keine Ortsauflösung der Verspannung. Aber gerade dies ist besonders bedeutend für die Mikrokomponenten, die sich an unterschiedlichen Orten auf dem Wafer befinden.

Die Mikroverspannung wird in dieser Arbeit mit Mikrostrukturen analysiert, welche durch einen oberflächenmikromechanischen Prozess (engl. surface micromachining) mit konventionellem Photolack als Opferschicht hergestellt wurden.

Beide Methoden wurden verglichen und auf ihre Relevanz untersucht. Dabei konnte gezeigt werden, dass die Plasmaanregungsfrequenz eine wesentliche Rolle bei der Verspannungseinstellung von Siliziumnitrid spielt. So wurden mit Siliziumnitrid (300 °C) Makroverspannungen zwischen -300 MPa (Zugverspannung) und +850 MPa (Druckverspannung) erreicht. Bei niedrigen Temperaturen (60 °C) weist die Verspannung von Siliziumnitrid ähnliche Zusammenhänge auf, während die Verspannung von Siliziumdioxid in beiden Temperaturbereichen nur eine sehr schwache Frequenzabhängigkeit zeigt. Die Untersuchung der Mikroverspannung bestätigte die Ergebnisse der Makroverspannungsuntersuchung.

Weiterhin ist der Einfluss der Verspannung auf die Krümmung der Membran und deren Auswirkung auf die Geometrie des Resonators systematisch untersucht worden. Dank dieser Erkenntnisse ist es gelungen, gezielte Membranformen (konkav, konvex und planar) mit verschiedenen Krümmungsradien zu entwickeln um damit diverse Resonatorgeometrien zu realisieren.

Zahlreiche nicht abstimmbare und abstimmbare Bauelemente mit einer angepassten Resonatorgeometrie konnten im Rahmen dieser Arbeit gezeigt werden. Die realisierten Fabry-Pérot Filter mit einem Luftspalt und einer gekrümmten Membran weisen eine spektrale Spannweite von über 200 nm und Linienbreiten bis 1.5 nm auf.

Mit derselben Technologie wurden im Rahmen einer engen Zusammenarbeit mit der Technischen Universität Darmstadt (Fachgebiet Optische Nachrichtentechnik) und dem Königlichen Technologischen Institut in Schweden (KTH) neuartige abstimmbare optische Bauelemente wie Fabry-Pérot Filter, VCSEL und Photodetektoren angefertigt.

Der monolithische Fabry-Pérot Filter ist thermoelektrisch durch mäanderförmige Mikrowiderstände aus Chrom abstimmbar, welche auf die gekrümmten Membran aufgebracht sind. Dabei wurde ein Abstimmbereich von 15 nm bei 1 mA Stromfluss und 2 kΩ Chrom-Dünnfilmwiderstand erzielt.

Durch eine gezielte Verspannungseinstellung und die sich ergebende Krümmung der oberen Membran eines abstimmbaren VCSELs konnte der fundamentale Mode gezielt unterstützt und so eine hohe Nebenmodenunterdrückung erreicht werden. Der realisierte Laser besitzt einen Abstimmbereich von über 26 nm und eine Seitenmodeunterdrückung von 57 dBm.

Durch eine Kombination eines abstimmbaren Fabry-Pérot Filters mit einem Photodetektor, ist ein spektral selektiver Empfänger für DWDM Systeme entstanden. Hier konnte eine Abstimmbarkeit der spezifischen Empfindlichkeit (0.3 A/W) über den freien Spektralbereich ($>$ 35 nm) hinaus mit einer Einfügedämpfung von 3.5 dB demonstriert werden.

Die mit dieser Technologie erzielten Ergebnisse dienten als Motivation, um neue Materialien und Ansätze zu untersuchen. So wurde ein organisch lichtemittierendes Material (Makromoleküle) in eine Mikrokavität erfolgreich eingesetzt und eine Linienbreitenverengung erreicht.

Im Rahmen dieser Arbeit ist es gelungen, Verspannungen gezielt einzustellen, um beliebige Resonatorgeometrien anzufertigen. Abstimmbare Mikrokavitätsbauelemente mit optimierten Resonatoren wurden so erfolgreich demonstriert. Die Technologie auf PECVD-Basis bildet dabei die Grundlage eines kostengünstigen Produktionsprozesses.

Erwähnt sei an dieser Stelle ein redaktioneller Bericht über Teile dieser Arbeit in "Photonics Spectra" (Juni 2004), der das internationale Interesse an diesem Forschungsthema dokumentiert.

Weitere Vertiefungen dieser Arbeit könnten zu einer Industrialisierung dieser Technologie führen und dadurch zur Massenproduktion kostengünstiger Mikrokavitätsbauelemente wie beispielsweise ein monolithischer abstimmbarer elektrisch gepumpter VCSEL. Ein Schwerpunkt weiterer Forschungen könnte die Herstellung von passiven und aktiven organisch basierenden abstimmbaren Elementen sein, welche in verschiedenen Bereichen wie der Sensorik, der Medizintechnik und der Unterhaltungstechnologien eingesetzt werden könnten.

List of own journal publications and conference papers

1. J. Daleiden, M. Strassner, N. Chitica, J. Pfeiffer, **A. Tarraf**, F. Römer, B. Ayele, C. Prott, and H. Hillmer, "Micromachined Multi-Airgap Bragg Mirrors for VC-SELs," *European Semiconductor Laser Workshop*, Berlin, September 2000.

2. J. Daleiden, N. Chitica, M. Strassner, C. Prott, F. Römer, **A. Tarraf**, and H. Hillmer, "Micromechanically Tunable Optical Devices," *Summer School and European Optical Society Topical Meeting on Semiconductor Microcavity Photonics*, Technical Digest, Ascona, October 2000.

3. J. Daleiden, **A. Tarraf**, E. Ataro, N. Chitica, S. Irmer, C. Prott, F. Römer, M. Strassner, H. Hillmer, "Micromechanically Tunable Filters for Optical Communication Systems," *Proceedings of the 1st Int. Workshop on Optical MEMS and Integrated Optics*, Dortmund, June 2001.

4. J. Daleiden, S. Irmer, H. Hohmann, D. Feili, **A. Tarraf**, E. Ataro, F. Römer, C. Prott, H. Hillmer, "Trockenätzen von phosphidischen III-V Halbleitern," *Workshop dry etching for III-V semiconductors*, Ulm, April 2001.

5. H. Hillmer, C. Prott, F. Römer, **A. Tarraf**, S. Irmer, M. Strassner, N. Chitica, and J. Daleiden, "Continuously tunable 1.55 μm vertical air cavity filters and VCSELs using micromachined electrostatic actuation," *European Semiconductor Laser Workshop*, Berlin, September 2001.

6. J. Daleiden, **A. Tarraf**, F. Römer, N. Chitica, S. Irmer, C. Prott, M. Strassner, H. Hillmer, "Continuously Tunable Air Gap Devices," *Proceedings of the IEEE / LEOS International Conference on Optical MEMS*, Technical Digest, Okinava, 2001.

7. J. Daleiden, V. Rangelov, S. Irmer, F. Römer, M. Strassner, C. Prott, **A. Tarraf**, H. Hillmer, "Record tuning range of InP-based multiple air-gap MOEMS filter," *Electronic Letters*, vol.38, no.21, pp.1270-1271, October 2002.

8. **A. Tarraf**, S. Irmer, E. Ataro, J. Daleiden, D. Gutermuth, C. Prott, V. Rangelov, F. Römer, H. Schröter-Hohmann, H. Hillmer, "Bionik: Erfolgsrezepte der Natur-Anwendungsbeispiele in der Mikrosystem- und Datenübertragungstechnik," *Tag*

des Wissenschaftlichen Nachwuchses, Universität Kassel, 2002 (POSTERPREIS 2002)

9. J. Daleiden, S. Irmer, **A. Tarraf**, F. Römer, C. Prott, E. Ataro, M. Strassner, H. Hillmer, " Multiple air-gap InP-based VCSELs and filters with ultra-wide wavelength tuning - flexibility and shape of the membranes," *Proceedings of the Optical MEMS Conference*, Hawai, August 2003.

10. F. Römer, C. Prott, J. Daleiden, S. Irmer, M. Strassner, **A. Tarraf**, H. Hillmer, "Micromechanically tunable air gap resonators for long wavelength VCSEL's," *IEEE LEOS International Semiconductor Laser Conference*, Garmisch, September 2003.

11. **A. Tarraf**, J. Daleiden, F. Römer, C. Prott, V. Rangelov, S. Irmer, E. Ataro and H. Hillmer, "A novel low-cost tunable dielectric air-gap filter," *Proceedings of the Optical MEMS Conference*, Lugano, August 2003.

12. M. Joodaki, **A. Tarraf**, M. Salih, D. Albert, H. Schröter-Hohmann, W. Scholz, G. Kompa, H. Hillmer, and R. Kassing, "Improvements of thermal resistance and thermal stress in quasi-monolithic integration technology (QMIT) with a new fabrication process," *European Microwave Week*, Milan, September 2002.

13. H. Hillmer, J. Daleiden, C. Prott, F. Römer, **A. Tarraf**, S. Irmer, V. Rangelov, S. Schüler, M. Strassner, "Ultra-wide continuously tunable 1.55 μm vertical air-cavity filters and VCSEL's based on micromachined electrostatic actuation," *Proceedings of the SPIE*, series 4646 (Photonics West), San Jose, 2002.

14. H. Hillmer, J. Daleiden, C. Prott, F. Römer, S. Irmer, V. Rangelov, **A. Tarraf**, S. Schüler and M. Strassner, "Potential for micromachined actuation of ultra-wide continuously tunable optoelectronic devices," *Applied Physics B*, vol. 75, 2002.

15. M. Strassner, N. Chitica, **A. Tarraf**, "Investigations of growth conditions for InP suited for Micro Opto Electro Mechanical Systems for data communication," *Proceedings of the 14th International Conference on InP and related Materials*, Stockholm, 2002.

16. J. Daleiden, S. Irmer, E. Ataro, C. Prott, V. Rangelov, F. Römer, M. Strassner, **A. Tarraf**, and H. Hillmer, "Continuously tunable air-gap micro-cavity devices for optical communication systems," *Proceedings of the SPIE*, series 4871 (IT-COM), Boston, 2002.

17. J. Daleiden, S. Irmer, V. Rangelov, F. Römer, **A. Tarraf**, C. Prott, M. Strassner and H. Hillmer, "Record wavelength tuning of 127nm for vertical cavity Fabry-Pérot filter," *Proceedings of the Optical MEMS Conference*, Lugano, August 2002.

18. M. Strassner, C. Luber, **A. Tarraf**, N. Chitica, "Widely tunable - constant bandwidth monolithic Fabry-Pérot filter with a stable cavity design for WDM

systems," *IEEE Photonics Technology Letters*, vol. 14, No. 11, pp. 1548-1550, 2002.

19. H. Hillmer, J. Daleiden, S. Irmer, F. Römer, C. Prott, **A. Tarraf**, M. Strassner, E. Ataro and T. Scholz, "Potential of micromachined photonics: miniaturization, scaling and applications in continuously tunable vertical air-cavity filters," *Proceedings of the SPIE*, series 4947 (Photonics Fabrication Europe), pp. 197-211, 2002.

20. S. Irmer, J. Daleiden, V. Rangelov, C. Prott, F. Römer, M. Strassner, **A. Tarraf**, H. Hillmer, "Continuously tunable InP based multiple air-gap MOEMS filters with ultra wide tuning range", *Proceedings of SPIE*, Series 4945 (Photonics Fabrication Europe), 2002.

21. C. Prott, F. Römer, E. Ataro, J. Daleiden, S. Irmer, M. Strassner, **A. Tarraf**, H. Hillmer, "Model calculations of vertical cavity air-gap filters and VCSEL's for ultra-wide continuous tuning," *International Conference on Numerical Simulation of Semiconductor Optoelectronic Devices (NUSOD)*, Zürich, September 2002.

22. F. Römer, C. Prott, S. Irmer, J. Daleiden, **A. Tarraf**, H. Hillmer, "Tuning efficiency and linewidth of electrostatically actuated multiple air-gap filters," *Applied Physics Letters*, vol. 82, no. 2, pp. 176-178, January 2003.

23. H. Hillmer, J. Daleiden, C. Prott, S. Irmer, F. Römer, E. Ataro, **A. Tarraf**, H. Rühling, M. Maniak, M. Strassner, "Bionics: Precise color tuning by interference in nature and technology - applications in surface-micromachined 1.55ţm vertical air-cavity filters," *Proceedings of the SPIE*, series 4983 (Photonics West), pp. 203-214, 2003.

24. S. Irmer, J. Daleiden, V. Rangelov, C. Prott, F. Römer, M. Strassner, **A. Tarraf**, H. Hillmer, "Ultra low biased widely continuously tunable Fabry-Pérot Filter," *IEEE Photonics Technology Letters*, vol. 15, no. 3, pp 434-436, March 2003.

25. **A. Tarraf**, J. Daleiden, S. Irmer, V. Rangelov, F. Römer, C. Prott, E. Ataro, H. Hillmer, T. Fuhrmann, T. Spher, J. Salbeck, "A novel low-cost and simple fabrication technology for tunable dielectric active and passive optical air-gap devices," *Proceedings of the SPIE*, series 4945 (Photonics fabrication Europe), pp. 9-20, 2003.

26. J. Daleiden, **A. Tarraf**, S. Irmer, F. Römer, C. Prott, E. Ataro, M. Strassner, H. Hillmer, "Wide and continuous wavelength tuning of microcavity devices for optoelectronic applications," *Journal of Microlithographie, Microfabrication, Microsystems*, vol. 2 no. 4, pp. 265-274, October 2003.

27. C. Prott, F. Römer, E. Ataro, J. Daleiden, S. Irmer, **A. Tarraf**, H. Hillmer, Modeling of Ultra-Widely Tunable Vertical Cavity Air-Gap Filters and VCSEL's,"

IEEE Journal of Selected Topics in Quantum Electronics, vol. 9, no. 3, pp. 918-928, 2003.

28. H. Hillmer, J. Daleiden, C. Prott, F. Römer, S. Irmer, E. Ataro, **A. Tarraf**, D. Gutermuth, I. Kommallein, and M. Strassner, "Ultra-wide continuously tunable 1.55 μm vertical air-cavity wavelength-selective elements for VCSELs using micromachined electrostatic actuation," *Proceedings of the SPIE*, series 4871 (IT-COM), Boston 2003.

29. H. Halbritter, M. Aziz, F. Riemenschneider, **A. Tarraf**, M. Strassner, O.P. Daga, and P. Meißner, "Performance Evaluation of WDM Components based on Tunable Dielectric Membrane Technology", *IEE Circuits, Devices and Systems*, vol. 150, no. 6, pp. 501-505, December 2003

30. H. Halbritter, C. Dhanavantri, M. Strassner, **A. Tarraf**, M. Aziz, F. Riemenschneider, S. Syguda, B.R. Singh, and P. Meißner, "Tunable and wavelength selective PIN diodes", *Proceedings of SPIE*, series 5277 (Microelectronics, MEMS and Nanotechnolgoy), pp. 129-137, December 2003

31. H. Halbritter, F. Riemenschneider, M. Strassner, **A. Tarraf**, I. Sagnes, and P. Meißner, "Properties of micromechanically tunable VCSEL," *Proceedings of the SPIE*, series 5277 (Microelectronics, MEMS, and Nanotechnology), pp. 292-301, December 2003

32. H. Halbritter, F. Riemenschneider, S. Syguda, C. Dhanavantri, M. Strassner, **A. Tarraf**, B.R. Singh, I. Sagnes and P. Meißner, "Tunable and wavelength selective pin photodiode," *Electronics Letters*, vol. 40, no. 6, pp. 388-390, March 2004.

33. **A. Tarraf**, F. Riemenschneider, M. Strassner, J. Daleiden, S. Irmer, H. Halbritter, H. Hillmer, and P. Meißner, "Continuously Tunable 1.55 ţm VCSEL implemented by Precisely Curved Dielectric Top DBR Involving Tailored Stress," *IEEE Photonics Technology Letters*, vol. 16, no. 3, pp. 720-722, March 2004.

34. **A. Tarraf**, J. Daleiden, S. Irmer, D. Prasai and H. Hillmer, "Stress investigation of PECVD dielectric layers for advanced optical MEMS," *Journal of Micromechanics and Microengineering*, vol. 14, no. 3, pp. 317-323, 2004.

35. S. Irmer, K. Alex, J. Daleiden, I. Kommallein, M. Oliveira, F. Römer, **A. Tarraf**, H. Hillmer, "Surface micromachined optical low-cost all-air-gap filters based on stress optimized Si3N4 layers," *Journal of Micromechics and Microengineering*, vol. 15, no. 4, pp. 867-872, April 2005.

36. H. Halbritter, F. Riemenschneider, B. Kögel, **A. Tarraf** , M. Strassner, S. Irmer, H. Hillmer, I. Sagnes, and P. Meißner, "MEMS-Tunable and Wavelength Selective Receiver Front End," *Proceedings of the 18th IEEE Conference on Micro Electro Mechanical Systems*, pp. 68-71, Miami, Jannuary 2005

37. **A. Tarraf**, M. Nestler, S. Martin, U. Poll, D. Roth, J. Dienelt, H. Neumann, B. Rauschenbach, S. Irmer, F. Römer, V. Daneker, H. Hillmer, "Dual Ion Beam Sputter Deposition System for EUVL Masks," *XUV Technologies and Applications workshop*, Bad Honnef, June 2004.

38. **A. Tarraf**, M. Nestler, H.-U. Poll, D. Roth, J. Dienelt, H. Neumann, B. Rauschenbach, S. Irmer, F. Römer, H. Hillmer, "A novel dual ion beam sputter deposition system for implementing low defect density and high-quality EUVL masks," *3rd International EUVL Symposium*, Miyazaki, November 2004.

39. **A. Tarraf**, M. Nestler, H.-U. Poll, S. Martin, D. Roth, J. Dienelt, H. Neumann, E. Schubert, B. Rauschenbach, M. Schulze, V. Daneker, S. Irmer, F. Römer, H. Hillmer, "Innovative concept for implementing particle free EUVL masks by novel dual ion beam sputter deposition systems," *SPIE Photo Mask Japan*, Yokohama, April 2005.

40. **A. Tarraf**, "Organic and inorganic tunable photonic micro-cavity devices for optical communications," *Surface Technologies with Plasma and Ion beam Processes*, Mühlleithen , March 2004.

41. J. Dienelt, H. Neumann, F. Scholze, E. Schubert, B. Rauschenbach, M. Nestler, **A. Tarraf**, M. Schulze, "In-situ ellipsometry and beam profile controlled linear ion beam source - screening for the IBD EUV-mask blank deposition," *MNE 2004*, Rotterdam, September 2004.

42. **A. Tarraf**, "Particle free MoSi mask blanks for the EUVL: Implementation and Metrology," *Surface Technologies with Plasma and Ion beam Processes*, Mühlleithen , March 2005.

43. H. Hillmer, **A. Tarraf**, S. Irmer, F. Riemenscheider, H. Halbritter, F. Römer, J. Daleiden, E. Ataro, C. Prott, M. Strassner, A. Hasse, S. Hansmann, and P. Meißner, "Wide continuously tunable 1.5mm vertical air-cavity wavelength selective elements for filters and VCSELs using micromachined actuation," *Proceedings of the SPIE*, Series 5825A (OPTO Irland 2005), April 2005.

44. J. Dienelt, H. Neumann, M. Kramer, E. Schubert, F. Scholze, M. Nestler, **A. Tarraf**, M. Schulze, and B. Rauschenbach, "EUV-mask blanks by ion beam sputter deposition: A novel tool concept and first results," *4th International EUVL Symposium*, San Diego (USA), November 2005.

Patents submissions

1. H. Hillmer, J. Daleiden, C. Prott, J. Daleiden, F. Römer, S. Irmer, D. Gutermuth, **A. Tarraf**, E. Ataro, "Optimierung eines mikromechanischen Bauelements mit Hilfe eines Ätzstern," DE: AZ 103 57 421.2-33

2. S. Irmer, J. Daleiden, **A. Tarraf**, H. Hillmer "Leitfähige Haltepfosten in luftspaltbasierenden, optoelektronischen Bauelementen," DE: AZ 10353546.2

3. H. Hillmer, J. Daleiden, C. Prott, F. Römer, **A. Tarraf**, S. Irmer, S. Schüler, V. Rangelow "Bauelement mit "chirped" DBR-Spiegeln," PCT: AZ PCT / DE2004 / 000605, DE: AZ 10318767.7

Contents

1 Background and Introduction **1**
- 1.1 Background 1
- 1.2 State of the art 3
  - 1.2.1 Brief presentation 3
  - 1.2.2 Highlights 4
- 1.3 Introduction and content 6

2 Basics of tunable microcavities **8**
- 2.1 Optical properties 8
  - 2.1.1 Bragg reflectors 8
  - 2.1.2 Fabry-Pérot filter 12
  - 2.1.3 Resonator stability 14
  - 2.1.4 Active devices 16
  - 2.1.5 Photodetector devices 18
- 2.2 Mechanical properties 19
  - 2.2.1 Micromechanical tuning 19
  - 2.2.2 Stress in thin films 21

3 PECVD technology: basics and material properties **25**
- 3.1 Basics 25
  - 3.1.1 Configuration of the involved PECVD 25
  - 3.1.2 Background of PECVD layer deposition 26
- 3.2 Material investigation (stress, composition and optical properties) . . . 28
  - 3.2.1 Silicon nitride 28
  - 3.2.2 Silicon dioxide 30
  - 3.2.3 Bragg mirrors 32

4 Technology for air-gap based microcavity devices **36**
- 4.1 Bulk and surface micromachining 36
  - 4.1.1 Photoresist based novel technology 37
  - 4.1.2 PECVD dielectric membrane 37

5 PECVD stress engineering **40**
- 5.1 Stress control of PECVD dielectric material 40
- 5.2 Impact of stress on optical and mechanical layer properties 46

5.2.1 Cavity length 48
5.2.2 Radius of curvature 50
5.2.3 Filter characteristics 52

6 Results of microcavity devices 56
6.1 Non tunable Fabry-Pérot filter 56
6.1.1 Solid stack filters 56
6.1.2 Air-gap filter 57
6.2 Tunable Fabry-Pérot filter 59
6.3 Non tunable VCSELs 61
6.4 Tunable VCSEL 65
6.5 Tunable high end receiver 68

7 Related applications 71
7.1 Organic microcavities 71
7.1.1 PECVD materials and DBRs 71
7.1.2 Organic half cavity 74

8 Conclusion 80

Bibliography 81

A State of the art: detailed description 97
A.1 Fabry-Pérot filter 98
A.2 Vertical cavity surface emitting laser 99

B Diagram supplements 103
B.1 PECVD technological investigation 103
B.2 Stress investigations 106
B.3 Stress impact on mechanical and optical properties 108

C Technological process flow 111
C.1 Air-gap Fabry-Pérot filters 111
C.1.1 Design IMA2 111
C.1.2 Design IMA3 113
C.2 Process flow of the tunable Fabry-Pérot filter 115
C.3 Process flow of the non tunable VCSEL 117

D DBRs for the blue wavelength range 118

E Abbreviations 119

F Stress impact on the ROC, L_{cav}, RW and FWHM 121

Chapter 1

Background and Introduction

1.1 Background

Who has not made this experience before? You just bought a mobile phone a few weeks ago and the next model with more advanced features is already available on the market for the same price! This trend can also be observed in other technological branches. Thus, faster personal computers and internet, novel cars electronics and optoelectronics, better medical and telecommunications technologies and smaller, more sophisticated personal electronics as well as highly precise sensors are needed in order to satisfy the demands of the society in the 21th century. Furthermore, these more stringent requirements are expected at low-cost.

However, in the last decades, the main focus was on information techology. Thus at the beginning of the 19^{th}century, a worldwide telephone network based on copper cables was established. The main purpose was the transmission of voice and text data. To meet the increasing demand for more capacity, high frequency communication (via coaxial cable) was introduced around 1940. With the first semiconductor computer in the early 1980s, a new area of semiconductor based communication and data transfer was ushered in. The rapid development of the semiconductor industry, resulted in the demand for large data transmission. This leads to the further development of the local networks (e.g. firstly within a company) and eventually to the a world wide web (WWW).

Nowadays, with the internet well established as the main communication tool worldwide (for private as well as for business purposes), a huge capacity for data transmission is needed. The more people are involved, the more data should be processed and the more bandwidth is required. In order to transmit the huge volumes of data, optical communication via glass fibers is used.

The introduction of the erbium doped fiber amplifier (EDFA) at the beginning of the 1990s enabled the development of the wavelength division multiplexing (WDM) and dense wavelength division multiplexing (DWDM) technologies, that ensure transmission rates up to 1 Tbp/s. This technology exploits the bandwidth of the existing fiber

network in a efficient manner without deploying further ones. Thus, this technology recently became very attractive for long distance data transmission. An introduction to the DWDM technology can be found elsewhere [1].

The boom of the optical networking [2] market in 2000 lead to overcapacity which consequently cooled down this market at the end of the year [3]. Due to this enormous overcapacity of the telecommunication industry, the infrastructure investment shrank worldwide [4]. A recent surge in optical communication was seen in the metropolitan area networks (MAN), where capacity on demand and dynamic network flexibility play major roles. Deploying more fiber is the most economical solution for transmission distances under 20 km, whereas the metro DWDM represents the optimum economic solution[1] above 50 km [5] (The metropolitan network is considered to be up to 150 km [6]).

Many market analyses forecast a growth in the investments in the metro DWDM systems. For instance, Pioneer Consulting predicts an increase in market opportunities from 1.4 billions dollars in 2001 to 12.6 billions by 2006. According to a market study by ElectroniCast Corp. [7], which presents a forecast for the consumption of major DWDM components and optical add/drop multiplexers, the growth will reach the amount of 34.6 billions dollars in 2009 (54% North America, 21% Europe, 23% Japan and Pacific Rim and 2% the rest of the world). According to this study, the consumption of components was in the order of 2.85 billions dollars in the year 2000 (17% Europe, 13% Japan and Pacific Rim, 70% North America and 1% the rest of the world).

The report by KMI Corp. [8] predicts a compound annual growth rate (CAGR)[2] of 43% in 2005 for DWDM systems, which corresponds to a market volume of 54 billions of dollars. However, by 2005, the short distance investments will represent only 18% of the mentioned market.

Further development of the market is conditional on the implementation of low-cost solutions [6]. The cost of the components is essential in deciding which kind of systems should be used. The adoption of coarse wavelength division multiplexing (CWDM) or DWDM, for instance, for metropolitan networks depends mainly on the costs of optical filters [6]. Even though that DWDM filters are key components in the novel DWDM systems, their per-channel cost is lower than those of the transmitters and receivers.

Stephen Montgomery, ElectroniCast president, noticed "while the per-channel cost of transmitter/receiver (T/Rs) pairs at a fixed wavelength will drop more rapidly than filter cost, there will be a strong countering trend toward deployment of higher data rate, more expensive T/Rs" [7]. The consumption forecast of DWDM components in the ElectroniCast study shows that 62% of all the DWDM components in 2000 are

[1] Best solution for both, overall costs and costs per wavelength.

[2] Rate at which a given present value would grow to a given future value within a difined period of time. $CAGR = \left(\frac{FV}{PV}\right)^{\frac{1}{ny}} - 1$, where FV is the future value, PV is the present value and ny is the time period in years

T/Rs and integrated optoelectronics (wavelength converter 6%, integrated optoelectronics smaller than 1%, multiwavelength transmitter 50%, DWDM filter module 13%, optical amplifier 19% and multichannel receiver 12%). In the year 2009, these modules will reach 85% of the needed DWDM components (wavelength converter 1%, integrated optoelectronics 37%, multiwavelength transmitter 39%, DWDM filter module 8%, optical amplifier 5% and multichannel receiver 9%).

Micro-electro-mechanical-systems (MEMS) and micro-opto-electro-mechanical systems (MOEMS) are potential key components of an effective low-cost solution for the metropolitan networks. However, these devices need to satisfy severe requirements set by the international telecommunication union (ITU). In contrast to the amplifiers and the receiver photodiodes, the transmitter and filter modules of the DWDM systems should operate very precisely according to the stringent requirements [7]. Thus, the transmitter and filter sets should provide several operating wavelengths with precise channel spacing and very narrow spectral linewidth. A major challenge worldwide is the development and implementation of low-cost components fulfilling these tough requirements. One solution for reducing the overall costs is to utilize tunable devices, allowing a probable wavelength shift to be spectrally corrected without replacing these components. This solution avoids the expensive costs incurred by having to store the same modules operating with different wavelengths. Another approach reducing the costs is to establish a low-cost technology for implementing these tunable devices.

1.2 State of the art

1.2.1 Brief presentation

The simplest microcavity device, presented during this thesis, is a Fabry-Pérot filter (FPF). It consists of a microcavity (solid or air) embedded between two distributed Bragg reflectors (DBRs). Each DBR is commonly fabricated by alternating two materials (the optical thickness is a quarter wavelength) having high and low refractive indices (n_H and n_L). A DBR consists of several periods and each period comprises two different layers (Figure 1.1). In this case, an in-phase construction of reflections at the consecutive interfaces between the layers ensures a strong reflection at the desired wavelength and a stop band can be formed.

A Fabry-Pérot resonator is shown in Figure 1.2 (a). It consists of two mirrors and a cavity. In this example, three modes (standing waves) can oscillate within the resonator. Figure 1.2 (b) shows the modes as spectral lines. Combining high reflective DBRs (instead of normal mirrors) with a cavity (of length L_{cav}), both spectra (DBR and Fabry-Pérot modes) overlap resulting in a single mode selection. Thus an optical Fabry-Pérot filter is formed. A detailed theoretical study can be found in chapter 2. Figure 1.3 shows a cross section of the optically used part of such a filter as well as several common lateral designs, which have been frequently used in the literature. Introducing a light emitting or a light absorbing material in the cavity, VCSELs and

photodetectors could be fabricated. By changing the cavity length L_{cav}, a spectral shift of the selected mode occurs. This effect is called spectral tuning.

1.2.2 Highlights

Tunable MEMS and MOEMS microcavity devices (e.g. vertical cavity surface emitting lasers (VCSELs), Fabry-Pérot filters (FPFs) and photodetectors) are the core of new dynamic dense wavelength division multiplexing (DWDM) systems. Over the past years, countless works dealing with tunable active and passive microcavities have been published. Relevant devices are those combining the advantages of the mechanical tuning with the optimized optical properties.

Concerning tunable Fabry-Pérot filters, the devices differs by the tuning concept and the technological implementation. Based on the InP material system, Irmer et. al. [9] present recently a continuously widely tunable InP/air based filter with 140 nm tuning range. The tuning (electrostatic) voltage is 3.2 V, whereas the FWHM is between 3 nm and 5 nm. A filter with a GaAs/AlAs bottom DBR and an Au/SiN_xH_y/GaAs top movable membrane is presented by Larson et. al. [10], and exhibits a tunability of 32 nm by a 14 V tuning voltage at a central wavelength of 932 nm. The membrane is actuated electrostatically and the FWHM of the filter resonance is 3 nm. A hybrid concept using a semiconductor cavity and dielectric mirrors ist presented by Hohlfeld et. al. [11]. The filter, based on the thermooptical effect, consists of a silicon cavity and two Si_3N_4/SiO_2 DBRs and shows a tunability of 3.5 nm and a FWHM of 1.19 nm. Low-cost all dielectric air-gap tunable filters are rare and difficult to implement due to the stress induced buckling of the top membrane. A novel 1.55 μm Fabry-Pérot filter with a stable half symmetric cavity design [12], shows a tunability of 70 nm by a tuning voltage of 14 V. The filter consists of two SiO_2/TiO_2 DBRs separated by an air-gap cavity. The radius of curvature of the top membrane is around 310 μm. The FWHM of the filter characteristics is 0.27 nm.

Using the same concept, Vakhshoori et. al. [13] presented a 1.55 μm tunable cw VCSEL with 2 mW output power and 50 nm tuning range. The novelty of this work was the implementation of a stable resonator by a curved top DBR with a radius of curvature (ROC) of 300 μm. The tuning occurs electrostatically. However, the authors did not reveal either the material system nor the technological implementation details of the curved mirrors. Recently, electrically pumped tunable VCSEL have been presented: Maute et. al. [14] produced an electrically tunable VCSEL, whose active region has already been described in [15]. The bottom mirror consists of CaF_2/a-Si multilayer and gold, the top movable mirror is a doped GaAs/AlGaAs DBR. The tuning of the two-chip based device [16] is done electrothermally. The device shows a single mode operation across 30 nm tuning with a SMSR better than 30 dB and a maximum output power of 76 μW. By the same technological implementation process, Riemenschneider et. al. [17] increased the tunability to 40 nm and the output power to 100 μW.

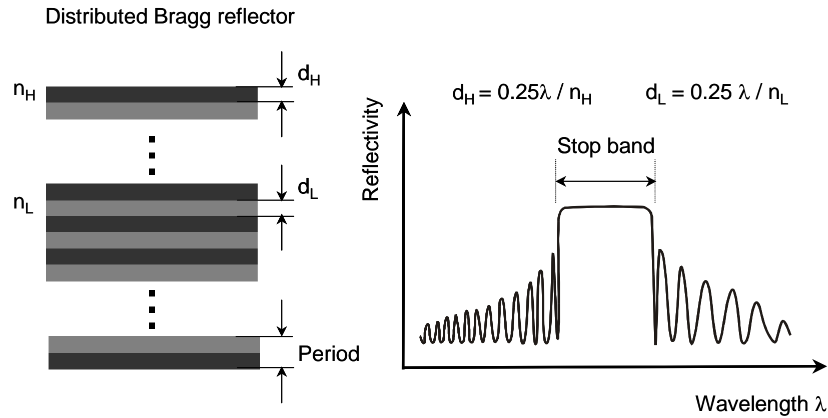

Figure 1.1: *A distributed Bragg reflector (DBR) consists of alternating layers of high and low refractive indices. The optical thickness of each layer is a quarter wavelength. Due to the constructive interference, a stop band with high reflection values can be formed.*

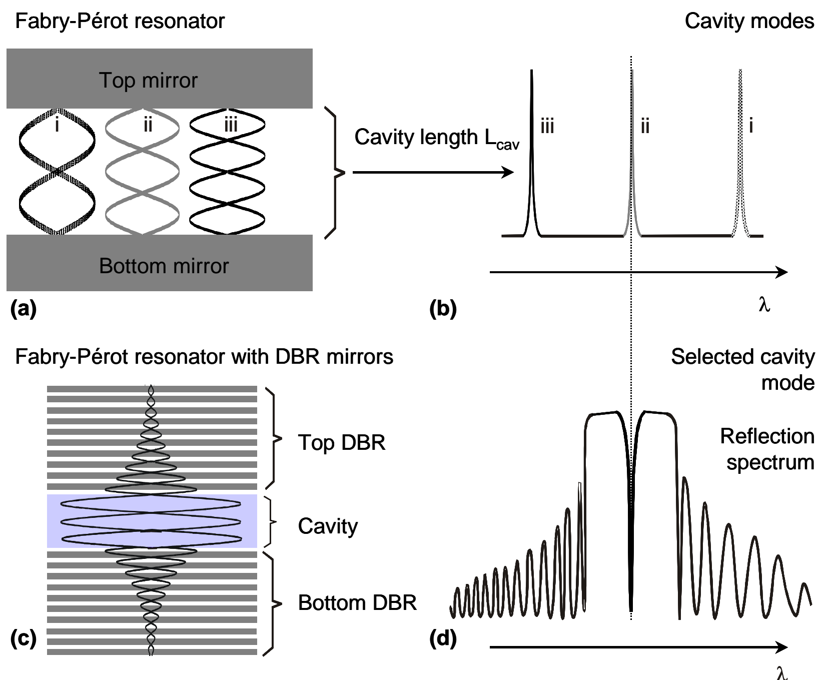

Figure 1.2: *(a) Fabry-Pérot resonator with common mirrors and schematically standing waves (modes) within the cavity, (b) Fabry-Pérot modes (spectral lines), (c) Fabry-Pérot filter with two DBRs. Due to the DBR spectral stop band, one mode can be selected (overlap of DBR stop band and Fabry-Pérot resonator modes).*

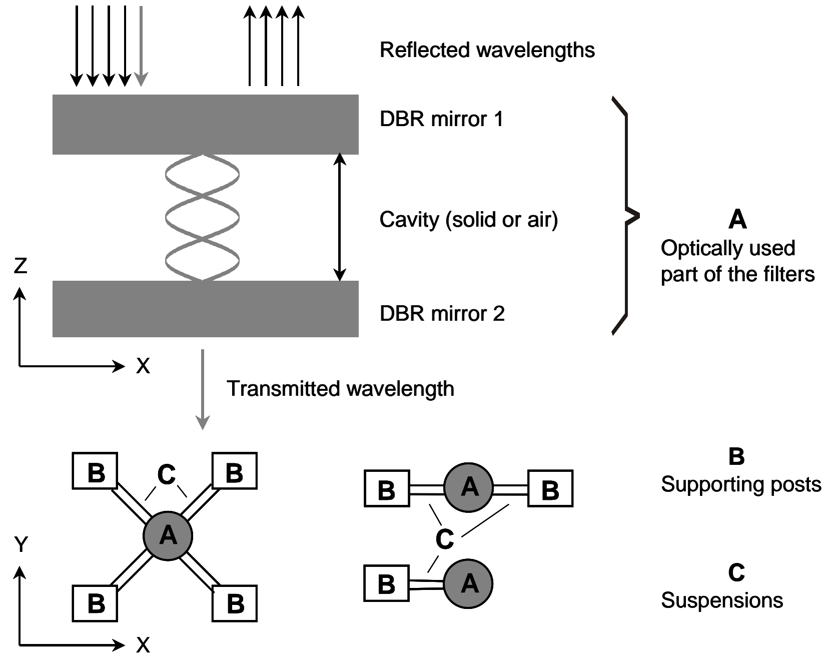

Figure 1.3: The optically used part of the Fabry - Pérot filter (Z-axis) consists of the cavity and two DBRs. This direction is called "vertical direction" during this thesis. The optical pass (light input and light output) occurs in this direction. In the XY plane (top view), the lateral design of the filter unit is shown. Several frequently published designs are illustrated. The optically used part "A" is positioned by suspensions "C". The suspensions are fixed to the substrate by supporting posts "B". The parts "A" and "C" may be suspended or attached to the substrate.

1.3 Introduction and content

Even though the progress in microcavity devices seems to meet soon the stringent optical communications requirements, two main problems remain. The first one is the immense costs resulting from the implementation process and the non economic concepts used, and the second one is the control of the stress induced buckling of the membranes leading often to unproper operation of these devices.

These two aspects are the core of this thesis. Thus, the aim is to develop a low-cost technology enabeling the fabrication of such devices in an economic way with high yield and to control and taylor the buckling of the released membranes. Seven chapters of this thesis deal with these issues.

In chapter 1, a survey of market analysis is presented to evoke the importance and the necessity of low-cost microcavity devices. It is shown that these devices claim a considerable part of the market. However, the economic yield of these devices can be reached only when a low-cost solution is available.

Chapter 2 presents the theoretical basics of the microcavity devices. In this chapter, the existing theory is extended and is explained in respect to the devices described in this thesis.

PECVD technology is investigated in chapter 3, with the goal to indentify a suitable technology enabling the implementation of novel low-cost devices, able to contribute to the economic boom of the optical communications. For this a common parallel plate reactor is used. The dependence of the mechanical (e.g. bulk stress) and the optical (e.g. refractive index) properties on the reactor parameters (e.g. gas flow, pressure, temperature, etc.) is investigated. It is shown that the optical properties can be readily affected by varying these parameters, whereas the mechanical properties (e.g. bulk stress) are less affected.

The stress control (especially the microstress) requires the development of a novel microscale technology, presented in chapter 4. Here, the deposition of dielectric PECVD layers on top of a common photoresist is demonstrated for the first time.

Chapter 5 presents the results of the dependence of macro- and microstress on plasma excitation frequency. For this purpose, different measurement techniques are used, and stress control in a wide range is achieved. Furthermore, the effect of stress on the mechanical properties of the suspended dielectric membranes is discussed. Thus, differently shaped membranes (planar, convex and concave) with several radii of curvature are implemented. A wide range of cavity length variation is demonstrated.

In the second part of the thesis, the knowledge acquired during the investigations is used for the implementation of several microcavity devices. Thus, in chapter 6, different microdevices like non tunable and tunable vertical cavity surface emitting lasers (VCSELs), non tunable and tunable Fabry-Pérot filters (FPFs) as well as tunable PIN photodiodes are presented. Furthermore, based on the results in chapter 6, the implementation of light emitting organic materials in microcavities is addressed in chapter 7. First promising results are presented and discussed. Finally, the whole work of this thesis is concluded in chapter 8.

Chapter 2

Basics of tunable microcavities

2.1 Optical properties

2.1.1 Bragg reflectors

Micromechanically tunable vertical cavity devices for the DWDM systems (e.g. FPFs, VCSELs and photodetectors) consist among other parts of an air-cavity embedded between two DBRs. The complete theory of these devices can be found elsewhere [18–22].

A distributed Bragg reflector consists of a periodic alternating layers of a high (n_H) and low (n_L) refractive index material. In analogy to the diffraction of X-ray light at atomic planes of a solids, the Bragg condition for a periodic multilayer is given by

$$\Lambda = \frac{\lambda_B}{N_{eff}} \cdot \frac{\Theta_{br}}{2} \tag{2.1}$$

where Λ is the grating period, λ_B the wavelength in vacuum, N_{eff} the effective refractive index of the alternating materials and Θ_{br} the Bragg order. Constructive interference occurs when Θ_{br} takes an odd integer values $(1, 3, 5, ...)$. By considering the physical thickness of the high and low refractive index materials, d_H and d_L, respectively, equation 2.1 can be rewritten as

$$\frac{\Theta_{br} \cdot \lambda_B}{4} = d_H \cdot n_H = d_L \cdot n_L \tag{2.2}$$

A frequent method for calculating the reflectivity of a DBR is the transmission or transfer matrix method. This considers the electric (E) and magnetic (H) fields of a transverse electromagnetic wave propagating in a layer (see Figure2.1).

By using the Maxwell´s equations, the following transmission matrix for the layer b can be found [19]

$$\begin{pmatrix} E(0) \\ \eta_o H(0) \end{pmatrix} = \begin{pmatrix} \cos(k_b d_b + i\alpha_b d_b) & \frac{i}{n_b}\sin(k_b d_b + i\alpha_b d_b) \\ i n_b \sin(k_b d_b + i\alpha_b d_b) & \cos(k_b d_b + i\alpha_b d_b) \end{pmatrix} \cdot \begin{pmatrix} E(d_b) \\ \eta_o H(d_b) \end{pmatrix} \tag{2.3}$$

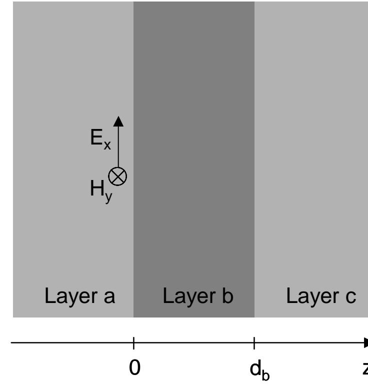

Figure 2.1: *A layer b is embedded between two layers, a and c, respectively. The layer has a physical length d_b and a refractive index n_b. The electromagnetic fields at positions 0 and d_b are $E(0)$, $H(0)$, $E(d_b)$ and $H(d_b)$, respectively. The direction Z is often described as vertical direction during this thesis.*

$E(0)$	is the electric field at position 0
$H(0)$	is the magnetic field at position 0
η_o	is the impedance of the free space
n_b	is the refractive index of layer b
d_b	is the physical thickness of the layer b
α_b	is the amplitude absorption coefficient in layer b
$k_b = 2\pi/\lambda_0 n_b$	is the phase propagation constant in the layer
λ_0	the wavelength in the free space

For a DBR with p periods and $2p$ layers and a total length L_{DBR}, a total transmission matrix M_{total} can be introduced. Thus, we can write

$$\begin{pmatrix} E(0) \\ H(0) \end{pmatrix} = M_{total} \cdot \begin{pmatrix} E(L_{DBR}) \\ H(L_{DBR}) \end{pmatrix} \tag{2.4}$$

$$M_{total} = \prod M_{layers} = \begin{pmatrix} m_{11} & m_{12} \\ m_{21} & m_{22} \end{pmatrix} \tag{2.5}$$

With Y_0 and Y_s the wave admittances of the ambient and substrate media respectively, the reflection coefficient can be written as

$$r = \frac{Y_0 m_{11} + Y_0 m_{12} - m_{21} - Y_s m_{22}}{Y_0 m_{11} + Y_0 m_{12} + m_{21} + Y_s m_{22}} \tag{2.6}$$

Frequently, the DBR used in such devices is mostly implemented by using quarter wavelength ($\Theta_{br} = 1$) thick layers. The incident electromagnetic wave is reflected and transmitted at each interface. The partial reflection (r) and transmission (t) coefficients of the wave at the interfaces are given respectively as

$$r = \frac{n_H - n_L}{n_H + n_L} \tag{2.7}$$

$$t = \frac{2n_L}{n_H + n_L} \tag{2.8}$$

The waves are not phase shifted by passing the interfaces of the layers with high refractive indices to the layers with the lower ones. However a phase shift π occurs in the other case. In this case, the partially reflected waves from the interfaces recombine constructively resulting in high reflection within a wavelength range (stop band). Beyond this range, a destructive interference ensures a low reflectivity.

The reflectivity of a DBR comprising p periods of lossless quarter wavelength layers (short: lossless p period quarter wavelength DBR) can be concluded from the reflectivity at the central wavelength. At this wavelength, the amplitude of the reflection coefficient [20] is given by

$$r_{2p} = \frac{1 - \frac{n_S}{n_0}\left(\frac{n_1}{n_2}\right)^{2p}}{1 + \frac{n_s}{n_0}\left(\frac{n_1}{n_2}\right)^{2p}} \tag{2.9}$$

Where n_0, n_S, n_1 and n_2 are the refractive index of the ambient, of the substrate, and the two different DBR materials, respectively. For the case of an additional layer, that means for a $2p+1$ periodic DBR, the reflection coefficient can be written as

$$r_{2p+1} = \frac{1 - \frac{n_1^2}{n_0 \cdot n_S}\left(\frac{n_1}{n_2}\right)^{2p}}{1 + \frac{n_1^2}{n_0 \cdot n_S}\left(\frac{n_1}{n_2}\right)^{2p}} \tag{2.10}$$

The reflectivity at the central wavelength can be calculated by $R = |r|^2$. Thus, the reflectivity of a lossless p period quarter wavelength DBR can be rewritten, by substituting from 2.9, as

$$R = \tanh^2\left[\frac{1}{2}\ln\left(\frac{n_0}{n_S}\right) + p\ln\left(\frac{n_1}{n_2}\right)\right] \tag{2.11}$$

By applying the equations 2.9 and 2.10, and by disregarding the term $(n_L/n_H)^4$, the following approximations for the reflectivity could be found [20] for $n_1 = n_L$ and $n_1 = n_H$, alternatively and respectively.

$$R_{2p} \approx 1 - 4\frac{n_S}{n_0}\left(\frac{n_L}{n_H}\right)^{2p} \tag{2.12}$$

$$R_{2p} \approx 1 - 4\frac{n_0}{n_S}\left(\frac{n_L}{n_H}\right)^{2p} \tag{2.13}$$

$$R_{2p+1} \approx 1 - 4\frac{n_L^2}{n_0 n_S}\left(\frac{n_L}{n_H}\right)^{2p} \tag{2.14}$$

$$R_{2p+1} \approx 1 - 4\frac{n_0 n_S}{n_H^2}\left(\frac{n_L}{n_H}\right)^{2p} \tag{2.15}$$

In the case of lossy DBRs [19], by assuming that $\alpha_i d_i < 1$, and by neglecting the the second and higher order terms in $\alpha_i d_i$ which leads to $\cosh \alpha_i d_i = \sinh \alpha_i d_i \approx 1$ (i indicates the layer number), we obtain the reflectivity R by multiplying matrices as in 2.3. Let $\gamma = n_2/n_1$, we have

$$R = \tanh^2 \left\{ \frac{1}{2} \ln \left[\left(\frac{(\alpha_2 d_2 n_1 + \alpha_1 d_1 n_2)(\gamma^{1-p} - \gamma^{p+1}) + n_S \gamma^{-p}(1-\gamma^2)}{\left(\frac{\alpha_2 d_2}{n_1} + \frac{\alpha_1 d_1}{n_2}\right)(\gamma^{1-p} - \gamma^{p+1}) + n_0 \gamma^{p}(1-\gamma^2)} \right) \right] \right\} \tag{2.16}$$

For $\Theta_{br} = 1$, large p and small constant α values in all layers, the reflectivity becomes

$$R = 1 - \frac{2\alpha\lambda_0 (n_1^2 + n_2^2)}{2n_0 |n_1^2 - n_2^2|} \tag{2.17}$$

However, due to different phenomena like material growth uncertainties and refractive index changes, a wavelength deviation $\delta\lambda$ from the Bragg wavelength λ_B may occur. A deviation in the wavelength implies a change in the refractive index in form of dispersion δn_1 and δn_2. By considering the equations 2.3 and 2.5, a new matrix can be adopted

$$M = (M_a \cdot M_b)^p \tag{2.18}$$

$$M_a = \begin{pmatrix} -\frac{\pi\delta\lambda}{2\lambda_B}\left(1 - \frac{\delta n_1}{n_1}\lambda_B\right) & \frac{i}{n_1} \\ i n_1 & -\frac{\pi\delta\lambda}{2\lambda_B}\left(1 - \frac{\delta n_1}{n_1}\lambda_B\right) \end{pmatrix}$$

$$M_b = \begin{pmatrix} -\frac{\pi\delta\lambda}{2\lambda_B}\left(1 - \frac{\delta n_2}{n_2}\lambda_B\right) & \frac{i}{n_2} \\ i n_2 & -\frac{\pi\delta\lambda}{2\lambda_B}\left(1 - \frac{\delta n_2}{n_2}\lambda_B\right) \end{pmatrix}$$

Using equation 2.9 and neglecting the second and higher terms of $\delta\lambda$, the reflectivity R for a large number p of periods is given by

$$R = \pm 1 \pm i\frac{\pi\delta\lambda}{\lambda_B n_0} \cdot \frac{(n_2 + n_n) n_2 n_1 - \lambda_B (n_1^2 \delta n_2 + n_2^2 \delta n_1)}{|n_2^2 - n_1^2|} \tag{2.19}$$

A high reflectivity of a DBR can be achieved by increasing either the number of periods p or the contrast between the refractive indices of the DBR layer pairs. However, absorption limits the reflectivity even when the number of periods p is increased [23,24].

The effect of absorption on the reflectivity for a given number p of periods can be reduced by choosing alternating material layers with high refractive index contrast. This is related to the optical penetration depth of the wave into the DBR. The optical penetration depth [20] P_e in quarter wavelength $\lambda/4n$ is given by

$$Pe = \frac{\lambda}{4n} \cdot \frac{\frac{n_L}{n_H}\left[1+\frac{n_L^2}{n_S^2}\left(\frac{n_0}{n_H}\right)^{2p-1}\right]\left[1-\left(\frac{n_0}{n_H}\right)^{2p}\right]}{1-\frac{n_0}{n_H}\left[\left(1+\frac{n_L^4}{n_H^2 n_S^2}\left(\frac{n_0}{n_H}\right)^{4p-2}\right)\right]} \tag{2.20}$$

The shorter the penetration depth, the lower is the total absorption within the optical path of the wave. On the other hand, an increase in the contrast between the refractive indices contributes to a larger bandwidth of the DBR. This can be deduced from the following equation, where $\Delta\omega$ and ω_0 are the frequency bandwidth and the central frequency of the DBR stop band, respectively.

$$\Delta\omega = \frac{4\omega_0}{\pi} \arcsin\left(\frac{n_H - n_L}{n_H + n_L}\right) \tag{2.21}$$

2.1.2 Fabry-Pérot filter

A simple Fabry-Pérot filter consists of a single or multiple optical half wavelength cavity embedded between two planar DBRs, oriented parallel to each other. The destructive and constructive interference of the waves in this cavity cause the filter characteristic. Thus, the reflectivity in the stop band tends towards zero for a few wavelengths, which leads to a high transmission. A deep theoretical study of FPF can be found in [18,22]. Beginning with the FP resonator with planar mirrors, the essential characteristics will be summarized. The free spectral range (FSR), which is important for the tuning later on, is the distance separating two neighboring filter characteristics. The FSR of a Fabry-Pérot filter can be written, in terms of the cavity length L_{cav}, the light velocity c and a refractive index n_{cav}, as

$$FSR = \frac{c}{2 \cdot n_{cav} \cdot L_{cav}} = \frac{\lambda \cdot \nu}{2 \cdot n_{cav} \cdot L_{cav}} \tag{2.22}$$

The finesse of a Fabry-Pérot filter, a figure of merit of the optical performance, indicates the ability to transmit several channels without serious interference among them. The finesse F can be expressed as a function of the reflectivity of both mirrors (R_1, R_2) and the absorption α_{cav} of the cavity, by

$$F = \frac{\pi \sqrt[2]{R_1 R_2 \cdot e^{-2\alpha_{cav} L_{cav}}}}{1 - (R_1 R_2 \cdot e^{-2\alpha_{cav} L_{cav}})} \tag{2.23}$$

The term $R_1 \cdot R_2 \cdot e^{-2\alpha_{cav} L_{cav}}$ is a factor correlated to the intensity variation for a round trip at the resonance frequency. The FWHM of a filter characteristic is affected by the cavity losses, the absorption in the material and the geometry of the resonator.

Thus the scattering of waves within a resonator is directly related to its geometry. Furthermore, the transversal mode in the cavity should match with the filter aperture in order to avoid diffraction losses.

$$FWHM = \frac{FSR}{F} = \frac{c \cdot \left[1 - \left(R_1 R_2 \cdot e^{-2\alpha_{cav} L_{cav}}\right)\right]}{(2 \cdot n_{cav} \cdot L_{cav}) \cdot \left(\pi \sqrt[2]{R_1 R_2 \cdot e^{-2\alpha_{cav} L_{cav}}}\right)} \tag{2.24}$$

The maximum transmission T_{max} and the residual reflectivity R_{res} at resonance are given, respectively, by

$$T_{\max} = -\frac{T_1 T_2}{\sqrt[2]{R_1 R_2}} \frac{\sqrt[2]{R_1 \cdot R_2 \cdot e^{-2\alpha_{cav} L_{cav}}}}{1 - \left(R_1 \cdot R_2 \cdot e^{-2\alpha_{cav} L_{cav}}\right)} \tag{2.25}$$

$$R_{res} = R_1 - \frac{T_1^2}{R_1} \frac{\left(R_1 \cdot R_2 \cdot e^{-2\alpha_{cav} L_{cav}}\right)}{1 - \left(R_1 \cdot R_2 \cdot e^{-2\alpha_{cav} L_{cav}}\right)} \tag{2.26}$$

For low loss optical resonators, we introduce the δ symbol to represent small deviations from unity at high reflectivity of the DBRs. In this case, we can write $R_1 = 1 - \delta_1$. A general definition for high and low reflective mirrors is given by

$$R \equiv e^{-\delta} \tag{2.27}$$

The total cavity loss δ_{cav} is given by the round trip loss δ_0 and the mirror losses δ_1 and δ_2

$$\delta_{cav} = \delta_0 + \delta_1 + \delta_2 = 4 \cdot \alpha \cdot L_{cav} + \ln\left(\frac{1}{R_1 R_2}\right) \tag{2.28}$$

This formula can also be rewritten to take into account the negative loss $-\delta_{act}$ (gain) of an active medium

$$\delta_{cav} = \delta_0 + \delta_1 + \delta_2 - \delta_{act} \tag{2.29}$$

Referring to 2.28, the finesse can be written as

$$F = \frac{2\pi}{\delta_{cav}} \tag{2.30}$$

The quality factor Q_{cav} of the cavity is a relation between the stored power in the resonator and the dissipated one per cycle of light.

$$Q_{cav} = \frac{4\pi L_{cav}}{\lambda \delta_{cav}} \tag{2.31}$$

2.1.3 Resonator stability

A highly important criteria for the fibre-filter coupling is the stability of the filter resonator. This stability is related to the radius of curvature of the bent membrane, to the cavity length as well as to the geometric alignment of the curved DBR[1]. Three main resonator configurations are possible, with a stable resonator being desirable. A resonator is stable when the distribution of the electric field remains unchanged after one round trip, which requires the curvature of the phase front of the electric field to agree with the radius of curvature of the mirror membrane. This can only occur in resonators fulfilling the equation 2.32 [25].

$$0 < \left(1 - \frac{L_{cav}}{ROC_1}\right) \cdot \left(1 - \frac{L_{cav}}{ROC_2}\right) < 1 \tag{2.32}$$

Unstable half symmetric resonators are shown in Figures 2.2(e) and 2.2(f). In the first case, the radius of curvature of the DBR2 is infinite ($ROC_2 = \infty$) whereas the radius of curvature of the DBR1 is smaller than the cavity length L_{cav} ($ROC_1 < L_{cav}$). In this case, equation 2.32 is clearly not satisfied. In the second case, equation 2.32 is also not satisfied since $ROC_2 = \infty$ and $ROC_1 < 0$. A stable half symmetric resonator satsfying equation 2.32 can be found in Figure 2.2(d). Here, we have $ROC_1 > L_{cav}$ and the $ROC_2 = \infty$. Figure 2.2(b) and Figures 2.2(a and c) show symmetric resonators that correspond to equations 2.33 and 2.34, respectively. These resonators are described as "nearly stable", since the smallest change in their curvature could lead to a unstable operation.

$$\left(1 - \frac{L_{cav}}{ROC_1}\right) \cdot \left(1 - \frac{L_{cav}}{ROC_2}\right) = 0 \tag{2.33}$$

$$\left(1 - \frac{L_{cav}}{ROC_1}\right) \cdot \left(1 - \frac{L_{cav}}{ROC_2}\right) = 1 \tag{2.34}$$

Thus, the symmetric concentric resonator (Figure 2.2(a)) with $ROC1 = ROC_2 = L_{cav}/2$ satisfies the condition of equation 2.34. The symmetric confocal resonator (Figure 2.2(b)) with $ROC1 = ROC_2 = L_{cav}$ corresponds to equation 2.33. The plane-plane symmetric resonator described in Figure 2.2(c) with $ROC1 = ROC_2 = \infty$ also satisfies equation 2.34.

In a stable half symmetric resonator (Figure 2.2(d)), the frequency of the resonant cavity mode [26] can be calculated by

$$\omega_{res} = \frac{c_0}{2L_{cav}} \left(m_l + \frac{2m_r + m_a + 1}{\pi} \arccos \sqrt[2]{1 - \frac{L_{cav}}{ROC_1}} \right) \tag{2.35}$$

[1] A curved DBR is possible when we consider a FPF with an air-gap cavity. This will be the subject of through study in this thesis.

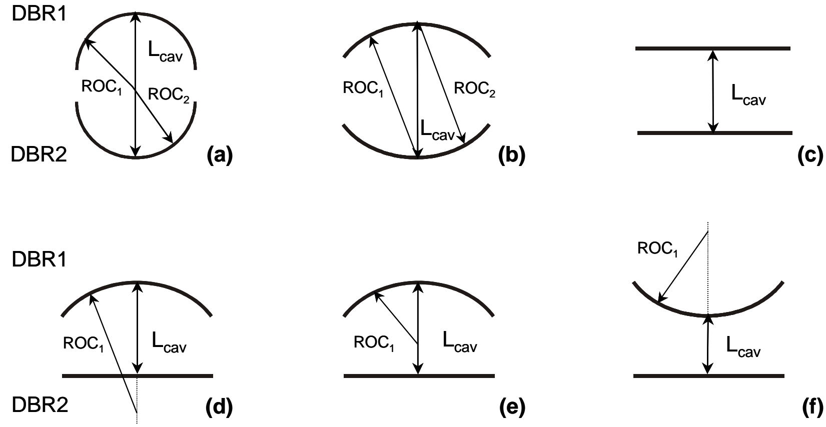

Figure 2.2: *Different geometrical configurations of resonators with partially or fully curved mirrors: (a) symmetric concentrical nearly stable resonator with* $ROC_1 = ROC_2 = L_{cav}/2$*; (b) symmetric confocal nearly stable resonator with* $ROC_1 = ROC_2 = L_{cav}$*; (c) plane nearly stable resonator; (d) stable half symetric resonator with* $ROC_1 > L_{cav}$*; (e) non stable resonator with* $ROC_1 < L_{cav}$*; (f) unstable resonator with negative* ROC_1 *values.*

where m_l, m_r and m_a are the longitudinal, the radial and the angular mode numbers. For a symmetric geometry of the bent DBR_1 and a given fundamental mode number m_l, numerous side modes with higher and lower resonance frequencies are available. In this case, no fundamental mode operation can occur and an arbitrary excitation leads to a multi mode operation. However, a fundamental mode operation occurs if the beam waist of the incoming Gaussian light beam (outcoming from the fibre) satisfies the condition

$$B_w^2 = \frac{\lambda}{\pi} \sqrt[2]{L_{cav}\left(ROC_1 - L_{cav}\right)} \tag{2.36}$$

Angular modes with mode numbers $m_a \neq 0$ occur by a geometrically non symmetric bent DBR_1 or by a non symmetric profile of the incoming light beam. In other words, in order to reach fundamental mode operation in a half symmetric stable resonator, either an appropriate fibre collimator should be used or a symmetric tailored radius of curvature of the bent membrane should be technologically implemented.

If the spectral spacing between several neighboring wavelengths is smaller than the central wavelength λ_0, we can convert the frequency spacing into wavelength spacing by using

$$\Delta\lambda = \frac{\lambda_0^2}{c}\Delta\omega \tag{2.37}$$

For a symmetric geometry of the bent DBR_1 and a tailored light beam profile, and by assuming that $ROC_1 \gg L_{cav}$ (the case for most of the devices technologically implemented in this thesis), a fundamental mode operation can occur ($m_r = m_a = 0$).

The wavelength spacing of the fundamental modes $\Delta\lambda_{fund}$ is given by incrementing the fundamental mode number m_l (in our case $m_l = 1$) by using equation 2.35 as

$$\Delta\lambda_{fund} = \frac{\lambda_0^2}{2L_{cav}} \tag{2.38}$$

For the case where the symmetric incoming beam profile matches with the symmetric geometry of the bent DBR1 membrane (but where the conditions of equation 2.36 are not fulfilled), a radial mode operation beside the fundamental mode occurs. The spacing $\Delta\lambda_{side}$ of neighboring side modes is calculated by incrementing m_r at a fixed mode number m_l and for $m_a = 0$. In this case , the radial mode spacing $\Delta\lambda_{radial}$, is

$$\Delta\lambda_{radial} = 2\Delta\lambda_{side} \tag{2.39}$$

Thus the spacing of the neighboring side modes is given by

$$\Delta\lambda_{side} = \frac{\lambda_0^2}{2\pi L_{cav}} \arccos \sqrt[2]{1 - \frac{L_{cav}}{ROC_1}} \tag{2.40}$$

However, equations 2.35 and 2.40 are not valid for active devices like VCSELs. Here, bulk material (active and non active) as well as quantum wells could be included. In this case, several factors such as the group refractive index (dependent on the wavelength) for example should be considered.

2.1.4 Active devices

The major difference between passive (e.g. Fabry-Pérot filter) and active devices (e.g. VCSEL) is, in a first estimation, the active light emitting material within the resonator. In this case, most of the relations concerning modes spacing in the Fabry-Pérot resonator are not applicable. However, the relations between the incoming beam waist, the geometry of the top DBR as well as the modes propagation remain valid in this case. The emphasis of this thesis is put on devices with curved top DBRs. The interest in the active region play in this case a minor role. A detailed study of active regions in lasers can be found elsewhere [19–21, 27]. Nevertheless, the fundamental properties of the VCSEL will be summarized.

A VCSEL with a bulk active region of gain g is considered. The VCSEL is embedded between two mirrors of reflectivities R_1 and R_2, respectively. The photon density ρ, which is induced by an electromagnetic wave in the active material, increases proportionally with the penetration depth and the total round trip of the wave in the resonator. By considering the gain distance d_{gain} and the loss factor α_{total}, a distance related photon density $\rho(d_{gain})$ can be defined [19] as follows

$$\rho(d_{gain}) = \rho_0 e^{(g-\alpha_{total})d_{gain}} \tag{2.41}$$

The threshold gain g_{th} is the gain level which overcomes the overall losses α_{total} in the VCSEL. It is expressed as a function of the cavity length L_{cav}, the transverse confinement factor Γ_t, R_1 and R_2 [19].

$$g_{th} = \alpha_{total} + \frac{1}{2L_{cav}\Gamma_t} \ln \frac{1}{R_1 R_2} \tag{2.42}$$

The threshold current I_{th} of a VCSEL is given by [27]

$$I_{th} = \pi \left(\frac{D}{2}\right)^2 J_{th} = \frac{eVN_{th}}{\eta_i \tau_s} \cong \frac{eVB_{eff}}{\eta_i \eta_{spon}} \tag{2.43}$$

D is the diameter of the circular active region (the most common shape)
J_{th} is the threshold current density
e is the electron charge
V is the volume of the active region
N_{th} is the threshold carrier density
η_i is the injection efficiency
η_{spon} is the spontaneous emission efficiency
τ_s is the recombination lifetime
B_{eff} is the effective recombination coefficient
where

$$N_{th} = N_t + \frac{\alpha_a + \alpha_d + \alpha_{1,2}}{\bar{A}_0 \Gamma_{opt}} \tag{2.44}$$

N_t is the transparent carrier density
α_a is the absorption loss coefficient averaged per unit length
α_d is the diffraction coefficient averaged per unit length
$\alpha_{1,2}$ is the DBRs loss coefficient
$\bar{A}_0$ is the gain coefficient expressing the differential gain $\dot{G} = d\dot{g}/dN$
$\dot{g}$ is the optical gain per cm
Γ_{opt} is the optical energy confinement factor, $\Gamma_{opt} = \Gamma_t \Gamma_l$
Γ_l is the longitudinal confinement factor

The optical output power P_{out} [20] of a VCSEL can be expressed in terms of the band gap energy E_g, the spontaneous emission factor $\acute{S}$, the driving current I, the threshold current I_{th}, the differential quantum efficiency η_d, the spontaneous emission efficiency η_{spon} and the injection efficiency η_i, as follows

For $I \leq I_{th}$

$$P_{out} = \eta_d \cdot \eta_{spon} \cdot \acute{S} \cdot E_g \cdot I \tag{2.45}$$

For $I \geq I_{th}$

$$P_{out} = \eta_d \cdot E_g \cdot (I - I_{th}) + \eta_d \cdot \eta_{spon} \cdot \acute{S} \cdot E_g \cdot I_{th} \tag{2.46}$$

where η_d is the differential quantum efficiency

$$\eta_d = \frac{\alpha_{1,2}}{\alpha_a + \alpha_d + \alpha_{1,2}} = \eta_i \frac{\left(\frac{1}{L_{cav}}\right) \ln \left(\frac{1}{R_1}\right)}{(\alpha_a + \alpha_d) + \left(\frac{1}{L_{cav}}\right) \ln \left(\frac{1}{\sqrt[2]{R_1 R_2}}\right)} \quad (2.47)$$

The power conversion efficiency η_p [20] for $I \gg I_{th}$ is given in terms of the output power, the driving current and the bias voltage V_b, as

$$\eta_p = \frac{P_{out}}{V_b I} = \left[\eta_i \frac{\left(\frac{1}{L_{cav}}\right) \ln \left(\frac{1}{R_1}\right)}{(\alpha_a + \alpha_d) + \left(\frac{1}{L_{cav}}\right) \ln \left(\frac{1}{\sqrt[2]{R_1 R_2}}\right)} \right] \cdot \frac{E_g}{V_b} \cdot \left(1 - \frac{I_{th}}{I}\right) \quad (2.48)$$

2.1.5 Photodetector devices

An important use for photodiodes is in combination with tunable filters. By using these novel devices, we can lower the overall costs of the DWDM systems. Several approaches have been suggested and discussed in the literature [28–31]. In particular, the two-chip concept described in [16] allows independent optimization of the various parts and parameters of the system (e.g. buckling of the membranes, wavelength tuning, selectivity and responsivity, etc.). Thus, an optimum functionality of the devices can be reached.

The main characteristics of a PIN photodiode are the responsivity, the junction capacitance and its influence on the demodulation bandwidth and the signal to noise ratio. The responsivity R_{resp} is the ratio of the generated current, I_{out}, to the optical input power, P_{in}. The responsivity can be written as a function of the quantum efficiency η, the elementary charge e, Planck´s constant h and the frequency w.

$$R_{resp} = \eta \frac{e}{hw} = \frac{I_{out}}{P_{in}} \quad (2.49)$$

The frequency $w = c_0/\lambda_0$ is inversely correlated to the wavelength. Therefore, for $\lambda_0 = 1550$ and $\eta = 1$, the maximum responsivity, which can be reached, is $R_{resp,max} = 1.25$ A / W. However, this theoretical value, can never be practically reached due to the light backscattering (between the layers), material absorption and absorption mechanisms like recombinations on the layer surfaces.

The junction capacity is given as

$$C_j = A \sqrt[2]{\frac{\varepsilon e N_D}{2(U_D - U)}} \quad (2.50)$$

Where A is the area of the diode, ε is the dielectric number, N_D is the donator concentration and $(U_D - U)$ is the potential difference applied to the diode. If we

consider a diode under potential, the capacity can be written as a function of the depletion region l_{zone} and ε_0 and ε_r, the dielectric constants for air and the pin diode material, respectively.

$$C_j = \frac{\varepsilon_0 \varepsilon_r A}{l_{zone}} \tag{2.51}$$

The bandwidth of the pin photodiodes is given as

$$BW_{3dB} = \frac{1}{2\pi R_s C_j} \tag{2.52}$$

where, R_s is the serial conductance of the diode. Substituting from equation 2.51, the bandwidth can be written as follows

$$BW_{3dB} = \frac{l_{zone}}{2\pi \varepsilon_0 \varepsilon_r A R_s} \tag{2.53}$$

Generally, the signal to noise ratio is given as

$$SNR_{pin} = \frac{I_{out}^2}{I_{noise}^2} \tag{2.54}$$

where I_{noise}, the noise current of the pin photodiode, is a function of the quantum noise of the photocurrent I_{out} and the dark current I_{dark}.

$$I_{noise} = \sqrt[2]{2eBW_{3dB}(I_{out} + I_{dark})} \tag{2.55}$$

If we also consider the thermal noise current I_{th} in a pin photodiode, the overall signal to noise ratio can be written as follows

$$SNR_{pin} = \frac{I_{out}^2}{I_{noise}^2 + I_{th}^2} \tag{2.56}$$

with I_{th} given by

$$I_{th} = \sqrt[2]{\frac{4kTBW_{3dB}}{R_s}} \tag{2.57}$$

where k is the Boltzmann constant and T is the temperature.

2.2 Mechanical properties

2.2.1 Micromechanical tuning

Tunable microdevices for the optical communication technology are often associated with active devices like lasers; in the last decades, several tunable laser sources have been commercially available on the market. These sources are used in medical engineering, sensing, spectroscopy, and material diagnostics. A thorough study of such devices

can be found in [32]. Nowadays, as the devices became smaller and more complicated, their tuning occurs often by micromechanical actuation (especially vertical cavity based devices). Thus, MEMS and MOEMS devices like micromirror arrays, sensors, alignment systems, as well as active and passive devices for optical communication [33, 34] are emerging.

Micromechanical tuning of the devices investigated in this thesis, namely FP filters, VCSELs and photodiodes occurs either electrostatically or electrothermally. Electrostatic tuning is carried out by a potential difference between two conducting or semiconducting layers, whereas thermal tuning is based on the expansion of a material through heating by a current. Mechanical actuation of a layer automatically implies that the layer should be movable. Commonly, the top DBR of such devices is underetched and encloses an air-gap cavity. Figure 2.3 shows the tuning principle in such devices.

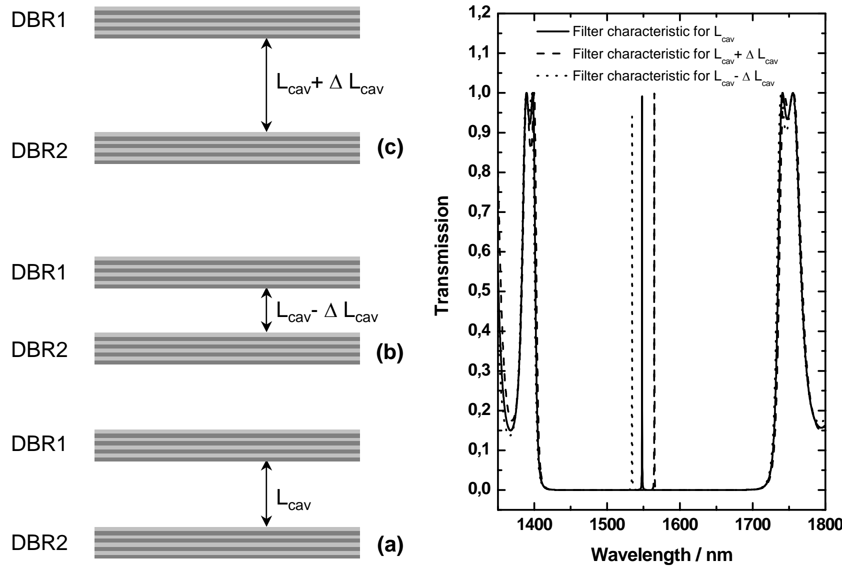

Figure 2.3: *Tuning principle of a Fabry-P érot filter with physical cavity length L_{cav} (a). A physical shift of the cavity length (b and c) $\pm\Delta L_{cav}$ implies a spectral shift in the wavelength by $\pm\Delta\lambda$.*

A physical change of the cavity length results in spectral displacement of the central resonance wavelength of the filter. However, the sensitivity of the spectral wavelength displacement strongly depends on the cavity length and the geometry of the resonator. This is captured by the tuning efficiency [35]

$$\text{Ŧ} = \frac{\Delta\lambda}{\Delta L_{cav}} \tag{2.58}$$

Although the technological implementation of tunable devices by bulk or surface micromachining has been well investigated and advanced, the performance of these

devices is still significantly restricted by fabrication issues, such the adverse effects of residual stress. In particular, devices involving air-gaps and suspended membranes (FPFs,VCSELs and photodiodes) require a precise stress control for a successful implementation [36, 37]. Due to the high sensitivity of these devices to stress, stress engineering is indispensable. Undesired buckling and bending of released micromachined structures (e.g. top DBRs) may be caused by compressive stress, whereas cracking may occur if the tensile stress is too high [38]. Several approaches reducing the effect of the overall stress on the released membranes have been proposed and successfully demonstrated [39–42]. They use additional stress compensation layers and suitable mechanical designs. However, these approaches do not directly deal with the origin of the residual stress and may be unsuitable for a wide range of optical devices. Thus, additional stress compensation layers in released distributed Bragg reflectors (DBRs) may induce phase shifts in the light path, thus disturbing functionality of the device. Other approaches using an appropriate mechanical design suitable for stress reduction in such devices, could be incompatible with the optical requirements, thus leading to undesired side and angular modes in the cavities. Consequently, the main goal of stress engineering is to control the stress in optical air-gap devices without modifying the mechanical or optical designs.

2.2.2 Stress in thin films

The distinction between stress and strain is clearly explained in the literature [43–46]. Strain is defined as the change in dimensions of a body under an external force and is expressed as the extension per unit length. Stress is the internal pressure of a body when submitted to external forces. When a body is placed under stress, strain results. Thus the strain ξ and the stress σ are related by the biaxial modulus Y [47].

$$\sigma = Y \cdot \xi \tag{2.59}$$

When the stress is homogeneous and biaxial, Y can be expressed in terms of the Youngs modulus E and the Poisson ratio ν of a material.

$$Y = \frac{E}{1 - \nu} \tag{2.60}$$

When the body is no longer subjected to external forces, it tends to relax and dissipate the internal stress. In the case of thin semiconductor and dielectric films, the overall stress is mostly described as residual stress. The residual stress, which is highly undesirable, is the tension or compression pre-existing in a bulk material (when the external force is zero). The origins of the residual stress in such films are mostly process related phenomena like defects, mismatching of the materials during the growth, ions implantation, thermal effects and boundary conditions. In this thesis the residual stress is devided into an intrinsic and an extrinsic stress. The intrinsic stress is due to the morphology and the dynamic composition of the material during the process,

whereas the extrinsic stress occurs after the dynamic process is accomplished. However, the extrinsic stress is not decoupled from the intrinsic one. The best example of an extrinsic stress is the thermal stress which results from the temperature change between deposition and characterization and the difference in thermal expansion coefficients of the film and the substrate [48–51]. The intrinsic stress, which is strongly related to the process parameters, influences the thermal expansion coefficients. In order to avoid obscurities, this thesis handles two different kinds of stress: the overall lateral bulk stress (described as homogeneous stress in several publications) and the vertical spatial stress variation (less precise but short: gradient stress). The overall lateral bulk stress $\sigma_{bulk,total}$ consists of the intrinsic stress σ_{int} and the thermal stress σ_{th}.

$$\sigma_{bulk,total} = \sigma_{int} + \sigma_{th} \tag{2.61}$$

In contrast to the intrinsic stress, the thermal stress can be calculated by the thermo dynamical equation

$$\sigma_{th} = \frac{E_f}{1-\nu_f} \cdot (\alpha_s - \alpha_f) \cdot \Delta T \tag{2.62}$$

in terms of the Young´s modulus E_f, the Poisson ratio ν_f and the thermal expansion coefficient α_f of the film, the thermal expansion coefficient of the substrate α_s and the difference in temperature ΔT between deposition and characterization.

The vertical spatial stress, referred to in some publications as gradient stress or strain, is the vertical variation of the internal force potentials which causes the deflection of the released cantilevers. Note that the overall bulk stress may also cause a deflection of structures that are fixed at all their extremities. In this case, it is difficult to find out which kind of stress is responsible for the deflection.

During the investigation within this thesis, the overall bulk stress is characterized at two levels: macroscopically averaged stress and microscopically detected stress [52]. The first quantity is calculated from the measured curvature of the wafer, and results in global values. The macroscopic stress measurement set-up is based on the optical imaging method [53]. It consists mainly of a HeNe laser source, a diffraction grid and a detector array [54]. The collimated laser beam travels through a telescope and a transmission grating and generates a spatial diffraction pattern on the wafer (one dimensional array). If the wafer is bent, these light spots are then reflected under slightly different angles and are observed on a distant screen. The position of the spots on the screen are evaluated and compared to their positions originating from the blank wafer before the deposition. If the wafer bends due to compressive thin film stress, the wafer acts as a convex mirror and the reflected laser beam diverges. Thus, in this case, bending of the substrate increases the distance between the separated diffraction structures. In case of a tensile stress, the wafer acts as a concave mirror. The total stress of the deposited dielectric layers can be calculated, based on the radii of curvature before and after the deposition, by Stoney´s equation as

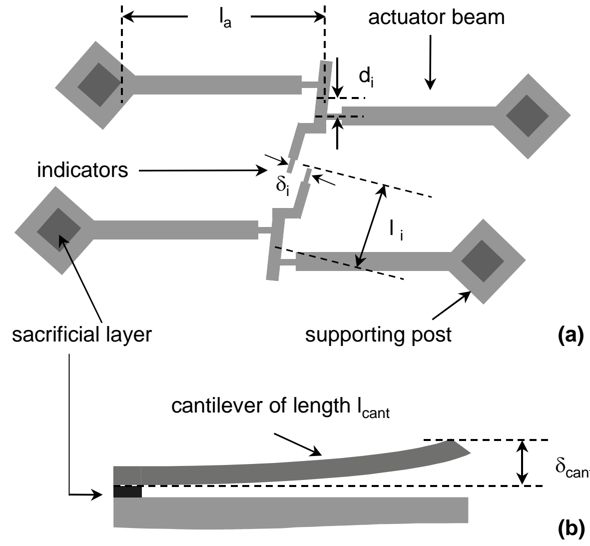

Figure 2.4: *MEMS structures for stress detection: (a) top view of a microstructure for microscopic stress detection, (b) cross section of a microstructure (cantilever) for detecting the vertical variation (short: gradient stress) of the stress.*

$$\sigma_{bulk,total} = \frac{E_s}{6\left(1-\nu_s\right)}\frac{d_s^2}{d_f}\left(\frac{1}{ROC_1}-\frac{1}{ROC_2}\right) \tag{2.63}$$

where E_s and ν_s are the Young modulus and the Poisson ratio of the substrate, d_s and d_f the thickness of the substrate and the film, ROC_1 and ROC_2 are the radii of curvature before and after the deposition, respectively.

The microscopically detected stress is monitored by MEMS structures [52] and describes the stress topography and thus delivers precise local values. These structures were first proposed by Ericson et. al. [55]. In the literature, several MEMS approaches have been proposed for stress diagnostics [36, 55–61] as well as for the characterization of the physical parameters of the films (e.g. thermal expansion coefficient, Young modulus, elastic modulus and fracture strength) [62–66]. The MEMS structure used for the bulk stress evaluation during this thesis is described in Figure 2.4(a).

The technological implementation of these structures is described in detail in chapter 4. The structure is completely underetched except under the supporting posts at the end of the actuator beams. After releasing the structure, the thin films tend to relax and can expand or shrink according to the nature of the stress. The magnitude of the stress is proportional to the rotation of the indicators. The direction of the rotation indicates whether the local stress in the lateral direction is compressive or tensile: the indicators rotate clockwise if the stress is compressive, and counter clockwise if tensile. In the case of stress free thin films, no rotation of the indicator beams occurs. The local stress can be calculated according to equation 2.64.

$$\sigma_{bulk,total} = \frac{E_f}{6\left(1-\nu_f\right)}\frac{d_i}{2l_il_a}\delta_i \tag{2.64}$$

The vertical spatial stress of a given film, can be calculated by evaluating the deflection of a released cantilever (2.4(b)) according to equation

$$\frac{\partial \sigma}{\partial d_{cant}} = \frac{E_f}{(1 - \nu_f)} \frac{2}{l_{cant}^2} \delta_{cant} \tag{2.65}$$

where σ is the internal stress of the film, d_{cant} and l_{cant} the thickness and the length of the cantilever and δ_{cant} is the deflection of the cantilever. Positive values of the gradient are associated with upwards deflection whereas negative values correspond to downwards deflection. Figure 2.5(a) shows a white light interferometer picture of released cantilevers with positive gradient value. A negative gradient is shown in Figure 2.5(b).

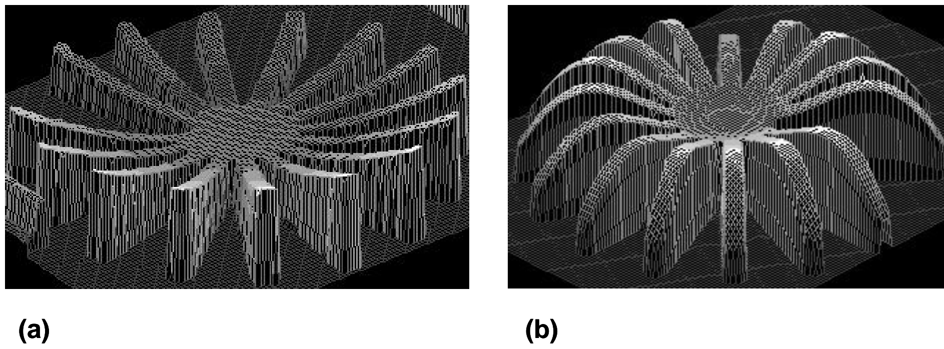

Figure 2.5: *White light interferometer pictures of: (a) released cantilevers with a positive stress gradient, (b) released cantilevers with a negative stress gradient.*

Chapter 3

PECVD technology: basics and material properties

3.1 Basics

3.1.1 Configuration of the involved PECVD

In this thesis, a plasma enhanced chemical vapor deposition technology (PECVD) is used for implementing dielectric layers. The system is a standard simple capacitively coupled parallel plate reactor (Plasma Lab 80 plus) from Oxford Instruments. Figure 3.1 shows a schematic layout of the system. The deposition chamber consists of a parallel plate reactor driven by a low (130 kHz) and a high (13.56 MHz) frequency generator. The high frequency generator is matched to the chamber trough an automatic matching unit (AMU). The duty cycle[1] of the plasma excitation frequency is varied during the process by an automatic switching unit (SWI). The substrate holder is grounded and can be heated up to 400 °C. Three mass flow controllers (MFC) ensure precise proportioning of the reactive gases. The radicals and ions that do not contribute to the deposition are eliminated by a root and a dual stage rotary pump.

Amorphous silicon nitride, silicon dioxide, silicon oxynitride and silicon can be deposited by the system. Two percent silane diluted in nitrogen and ammonia are used for silicon nitride whereas silicon dioxide results from the same silane and nitrous oxide. Other process gases like nitrogen (N_2), Argon (Ar), Oxygen (O_2) and a cleaning gas like carbon tetrafluoride with oxygen (CF_4+O_2) are also available. In this thesis we concentrate on the materials silicon nitride and silicon dioxide. Table C.7 shows the standard process parameters used for the deposition of silicon nitride and silicon dioxide at 300 °C. In order to study the dependence of the material properties, namely deposition rate, refractive index and stress, on the process parameters, one parameter is varied at a time while keeping the remaining parameters unchanged.

[1] The frequency duty cycle is defined in this thesis as: The time ratio between the high and the low frequency during the deposition process.

Table 3.1: Standard PECVD process parameters for silicon nitride and silicon dioxide deposited at 300 °C.

Process parameters	$Si_3N_4 : H_x$	SiO_2
2% SiH_4–N_2 flow / sccm	1000	430
NH_3 flow / sccm	20	0
N_2O flow / sccm	0	710
HF-power / W	20	20
LF-power / W	20	20
Duty cycle Ψ	0.538	1
Temperature / $°C$	300	300
Pressure / torr	0.65	1

3.1.2 Background of PECVD layer deposition

Plasma enhanced chemical vapor deposition is a very common, simple and reliable technique for implementing dielectric layers. Yet even by using the same technological process, different reactor configurations result in different material properties. Thus in the literature, different results for the same deposition process could be found. The main advantage of the PECVD technology is its ability to deposit dielectric materials at low temperatures (250 °C–400 °C), compared to the LPCVD. Hence, PECVD technology is used in a wide range of applications. However, this advantage negatively affects the properties of the materials. Thus silicon nitride deposited at lower temperatures may not be stoichiometric and may contain a high[2] concentration of hydrogen. The incorporation of hydrogen in silicon dioxide is not a main issue in the literature. An overview dealing with PECVD deposition and material properties can be found in [67,68].

Based on several publications, Habracken et. al. [67] reviewed the mechanical and optical properties of silicon nitride. They found that the properties of the plasma nitrides depend on the Si/N concentration ratio, on the hydrogen content as well as the concentration ratio of the Si-H/N-H bonds [69–71]. Furthermore, the N/Si ratio decreases by increasing the deposition temperature and the process pressure [72]. However, the N/Si ratio is proportional by the square root to the precursors ratio of NH_3/SiH_4 [73]. By increasing the deposition temperature, the hydrogen concentration decreases [72,74]. The incorporation of hydrogen in silicon nitride derived from SiH_4 and NH_3 precursors can be as high as 39% [75]. This hydrogen is mostly bonded to the silicon and nitrogen as Si-H and N-H compounds. Thus, the N/Si ratio and consequently the N-H/Si-H ratio defines the dominant hydrogen compound in the films. A strong concentration of N-H bonds can be found in nitrogen rich films, otherwise Si-H bonds dominate [71,72]. The N/Si ratio as well as the hydrogen concentration strongly affect the refractive index and the stress of the films. However, statements on the morphology of thin films deduced from measuring the refractive index are mostly incorrect since different film compositions may result in the same refractive index value [70].

[2] The concentration depends on several factors, e.g. the deposition temperature and the plasma conditions.

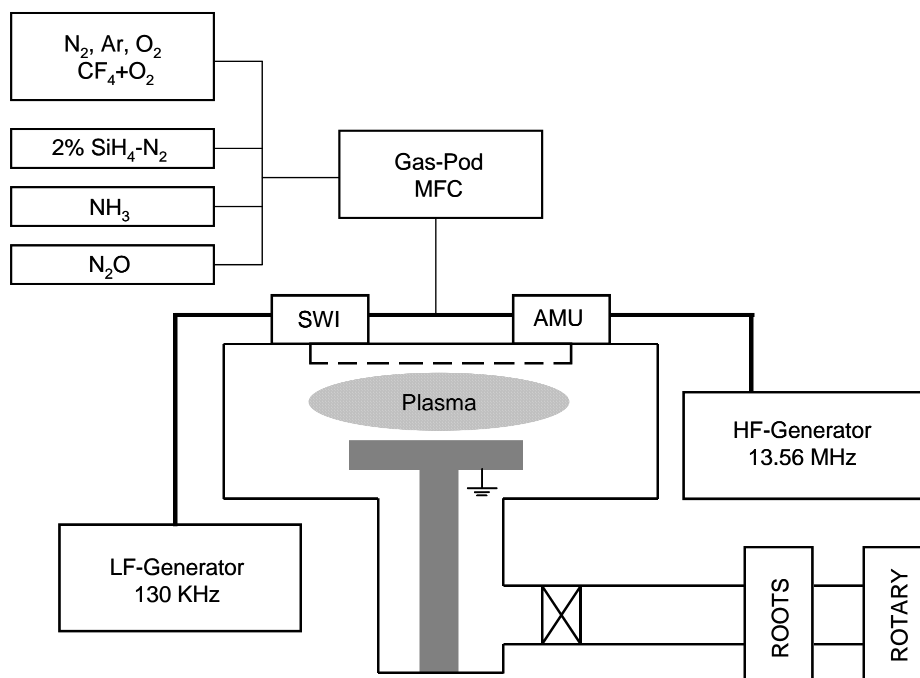

Figure 3.1: *Configuration of the plasma enhanced chemical vapor deposition (PECVD) machine used (Plasma Lab 80 plus, Oxford Instruments).*

For a given hydrogen content, the variation of the refractive index is proportional to the N/Si ratio. By increasing the nitrogen content, the refractive index decreases. Incorporating larger amounts of Si in the films lead to a higher refractive index. On the other hand, for a constant N/Si ratio, the variation in the refractive index value is inversely proportional to the hydrogen concentration. Thus by increasing the hydrogen content in the films, the refractive index decreases. The refractive index is strongly related to the dynamic process conditions and parameters like deposition temperature, process gas flow and pressure.

Concerning the mechanical properties of thin films, different correlations between the stress and the films composition is made in the literature [74, 76]. However, the stress seems to be strongly related to the dynamic of the deposition process (ion energy and the atomic architecture of the films). The stress control by tuning the layer morphology (via the plasma frequency) is thoroughly discussed in this thesis (chapter 5).

These correlations will be used to comment on the results found during the PECVD investigation in section 3.2. However, while discussing the results, I will not refer again to these references.

3.2 Material investigation (stress, composition and optical properties)

For the PECVD material investigation, the process parameters described in table C.7 are used. The behavior of the refractive index, the deposition rate and the stress[3] of the silicon nitride and silicon dioxide films as a function of various process parameters is studied. For this, a single parameter is varied at a time whereas the rest is kept unchanged.

3.2.1 Silicon nitride

Throughout this series of experiments, both the high and low frequency power are fixed at 20 W. The frequency duty cycle Ψ is fixed at 0.538. Figure 3.2 exhibits the behavior of silicon nitride for varying the process temperature. The deposition temperature varies between 230 °C and 320 °C. The silane and ammonia flows are 1000 sccm and 20 sccm, respectively. The deposition occurs at a pressure of 0.65 torr. The refractive index increases (1.928 to 1.984) with increasing the deposition temperature. This is due to the decrease of the hydrogen concentration in the film. In this case, the density became higher, and consequently the deposition rate lower since higher matter per unit volume is reached. The effect of the temperature on the total bulk stress variation is rather weak. In this case, the stress is tensile for the whole temperature range. Stress values between −11 MPa and −100 MPa were found. However by increasing the deposition temperature, the stress tend to get less tensile. This is probably due to the decrease of the hydrogen content, and the increase of the density. The break down of the refractive index trend at 300 °C is also been noticed in [68].

By varying the silane flow from 800 sccm to 1200 sccm (Figure 3.3) which corresponds to a variation of the N/Si ratio between 0.025 and 0.0166, a strong change in the refractive index is observed (1.93 to 2.0). The refractive index is strongly related to the N/Si ratio. The ammonia flow is 20 sccm. The deposition occurs at 0.65 torr.The tensile stress behavior (−12 MPa to −130 MPa) and the deposition rate show no constant corrolation with the N/Si ratio variation.

Furthermore, a decrease of the refractive index (2.01 to 1.91) is observed by increasing the ammonia flow (Figure 3.4). Since the temperature has a fixed value of 300 °C, the refractive index depends in this case on the N-H/Si-H ratio only. Thus by varying the ammonia flow range between 15 sccm and 30 sccm, the N/Si ratio varies between 0.015 and 0.03. A higher N/Si ratio means a higher concentration of nitrogen and thus a lower refractive index. In this experiment, the silane flow is 1000 sccm. The deposition occurs at a pressure of 0.65 torr. The stress varies from −60 MPa to −200 MPa, which can be explained by assuming that decreasing the Si content in the

[3] In this chapter, the measured bulk stress is reported as a result of varying the process parameters. The stress control by varying the duty cycle of the PECVD plasma excitation frequencies is reported in chapter 5.

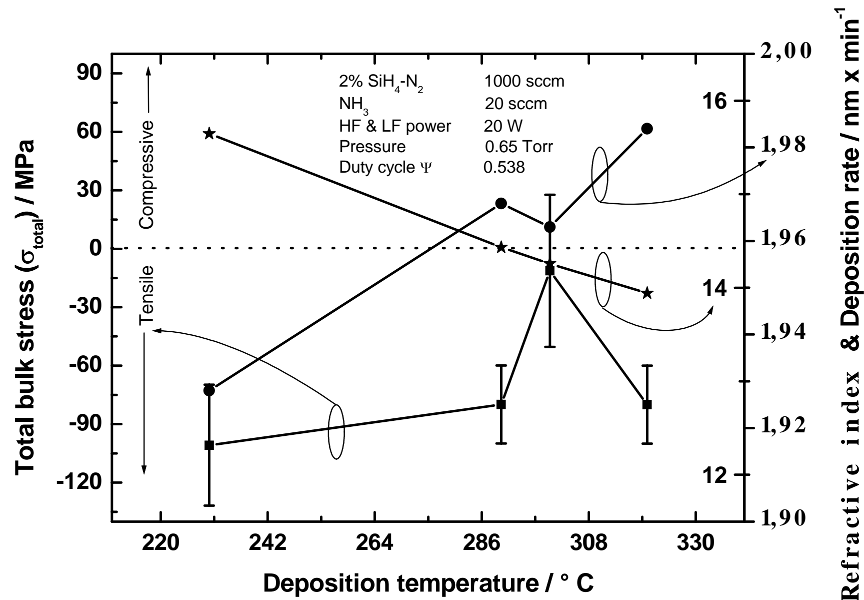

Figure 3.2: *The dependence of the bulk stress σ_{total}, the refractive index $n_{\mathrm{Si}_3N_4}$ and the deposition rate of silicon nitride on the PECVD process temperature. The values of the data plotted in the diagram can be found in table B.2.*

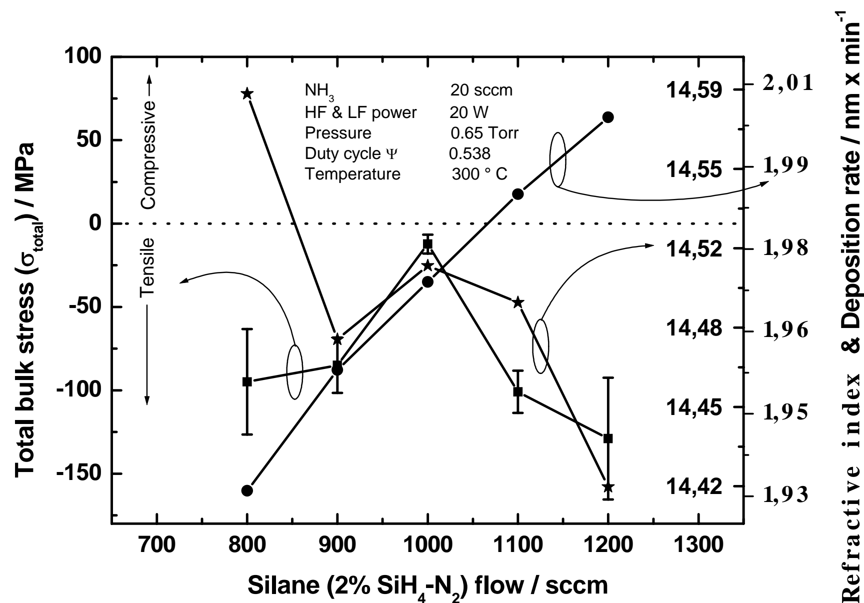

Figure 3.3: *The dependence of the bulk stress σ_{total}, the refractive index $n_{\mathrm{Si}_3N_4}$ and the deposition rate of silicon nitride on the silane flow. The values of the data plotted in this diagram can be found in the table B.3.*

films leads to higher N-H bonds and thus less dense films. This fact forces the films to contract causing tensile stress. Higher N-H bonds concentration leads normally to higher tensile stress.

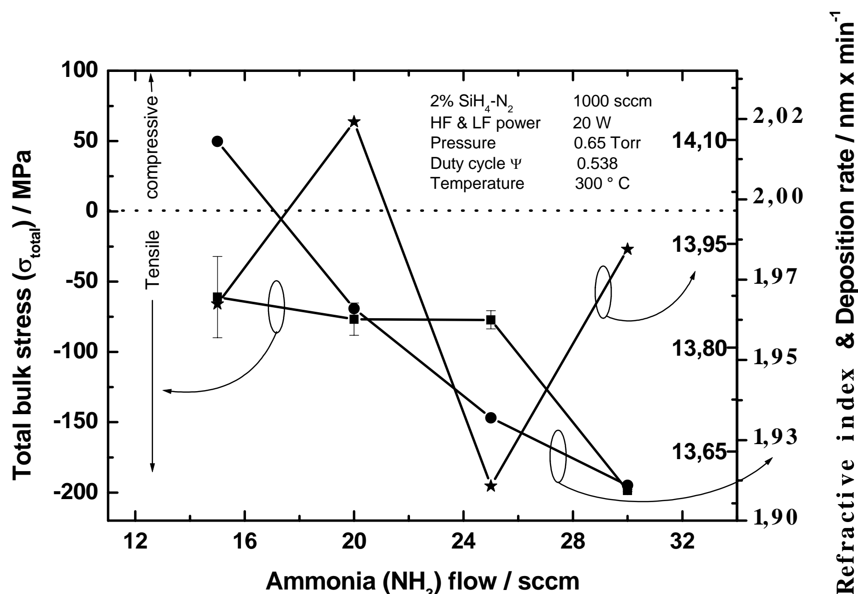

Figure 3.4: *The dependence of the bulk stress σ_{total}, the refractive index $n_{Si_3N_4}$ and the deposition rate of silicon nitride on the ammonia flow. The values of the data plotted in this diagram can be found in the table B.4.*

Figure 3.5 shows the dependence of the optical and mechanical properties of silicon nitride on the process pressure. The temperature is fixed at 300 °C. The silane and ammonia flows are 1000 sccm and 20 sccm, respectively. The pressure varies between 0.5 torr and 1.1 torr. The refractive index is observed to increase (1.9 to 2.0) with increasing the process pressure. Since the ammonia and silane flows as well as the temperature are constant, and the NH_3/SiH_4 ratio is 0.02 and proportional to the N/Si, the refractive index should not vary based on the previous assumption. However, it seems that the retention time of N and Si behave differently at different pressure, which leads to a variation of the N/Si ratio and thus the refractive index. The stress and the deposition rate varies arbitrarily with the pressure.

3.2.2 Silicon dioxide

Concerning the deposition of silicon dioxide, the incorporation of hydrogen in the layers is rarely described in the literature. When silane is cracked in the plasma, hydrogen ions and radicals are present so that in the absence of oxygen (N_2O in this case), hydrogenized amorphous silicon films will result. On the other hand, in the presence of oxygen, any stoichiometry from hydrogenated to nearly pure silicon dioxide can be deposited. This flexibility is a real process challenge. Good control of the gas mixtures is required to deposit pure, hydrogen free silicon dioxide. An excess of silane leads to Si-H bonds in the films, whereas too much oxygen delivers Si-OH compounds [77].

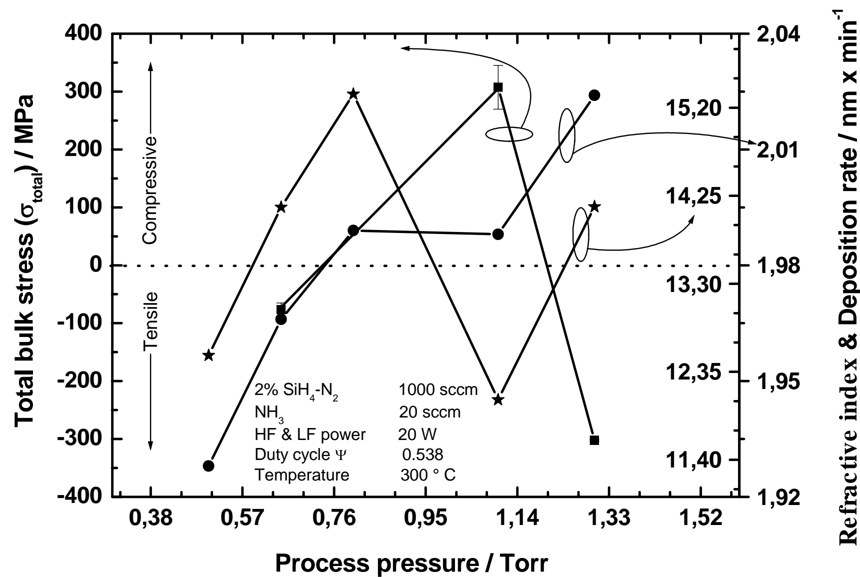

Figure 3.5: *The dependence of the bulk stress σ_{total}, the refractive index $n_{Si_3N_4}$ and the deposition rate of silicon nitride on the process pressure. The values of the data plotted in this diagram can be found in B.5.*

The refractive index and the deposition rate vary with changing process parameters. The bulk stress of silicon dioxide, on the other hand, does not seem to depend on the process parameters and exhibits compressive values with rather low variation (Figures 3.6, 3.7, 3.8 and 3.9). This effect is most probably due to the strong Si-O bonds, that seems to be stronger then the tension in the films.

Figure 3.6 shows the dependence of the refractive index, the bulk stress and deposition rate of silicon dioxide deposited by changing the deposition temperature between 230 °C and 320 °C. The silane and nitrous oxide gas flows are 430 sccm and 710 sccm, respectively. The high and low frequencies power are 20 W, whereas the process pressure is 1 torr. The frequencies duty cycle Ψ is 1 in this case. The stress is compressive and varies between +232 MPa and +135 MPa. The refractive index increases weakly from 1.464 to 1.467 with increasing temperature. The determining factor here is the hydrogen concentration in the films; the higher the temperature, the lower the hydrogen content and thus the higher the refractive index. The very small variation in the refractive index ($33.3E^{-6}$ °C^{-1}) is due to the low hydrogen content in the films for these process parameters. The deposition rate increases from 63.4 nm / min to 69 nm / min.

By varying the silane flow between 400 sccm and 520 sccm only (Figure 3.7), the stress shows no strong dependence (compressive, +164 MPa to +83 MPa). However, the refractive index increases from 1.468 to 1.487 by increasing the silane flow. This is due to the higher Si content in the films. The deposition rate increases from 66 nm / min to 70 nm / min.

Figure 3.8 exhibits the dependence of the bulk stress, refractive index and the deposition rate on the nitrous oxide flow (650 sccm and 850 sccm).

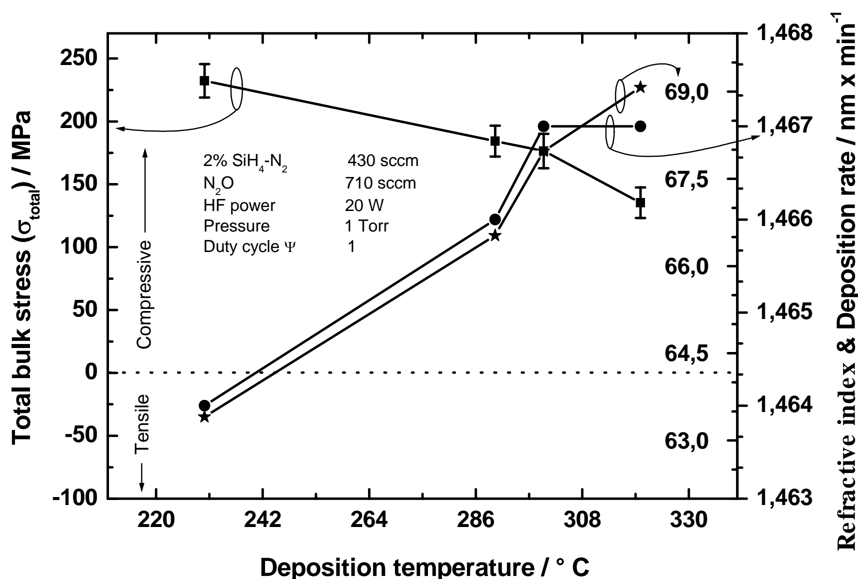

Figure 3.6: The dependence of the bulk stress σ_{total}, the refractive index n_{SiO_2} and the deposition rate of silicon dioxide on the process temperature. The values of the data plotted in this diagram can be found in the table B.6.

The refractive index and the deposition rate are inversely proportional to the nitrous oxide flow. The higher the nitrous oxide flow, the higher the oxygen content and the lower the refractive index. However, by varying the process pressure (Figure 3.9), the refractive index and deposition rate seem to vary arbitrarily. This observation can be explained only if we consider the dwell time of the reactive ions in the deposition chamber.

3.2.3 Bragg mirrors

The main task in this thesis is to establish a PECVD technology enabling the implementation of differently stressed DBR without affecting the optical properties. This is rather complicated task since the optical and mechanical properties are correlated. However, based on this investigation and the stress study later on (see chapter 5), the mechanical and optical properties have been tuned independently. Thus I tailor the DBRs precisely to fulfil the requirements for several applications. Figure 3.10 shows the shematic cross section of a PECVD DBR implemented by differently stressed silicon nitride and silicon dioxide layers. The first 3 periods consist of compressively stressed silicon nitride (+850 MPa) and silicon dioxide (+517 MPa). The rest of the DBR is implemented by nearly stress free silicon nitride (+20 MPa) and compressively stressed silicon dioxide (+517 MPa).

The DBR is designed to be implemented as a bent membrane (after bulk releasing) in a two chip VCSEL (see chapter 6). Therefore, a precise tailoring of the stress across the vertical structure of the DBR is needed. Thus, a defined radius of curvature as well as a desired cavity length could be obtained. However, this mechanical tailoring

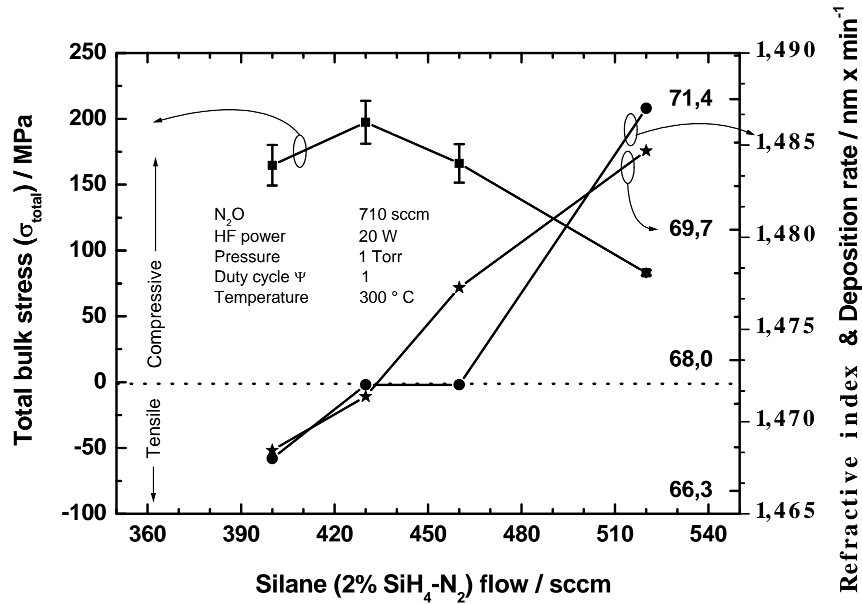

Figure 3.7: The dependence of the bulk stress σ_{total}, the refractive index n_{SiO_2} and the deposition rate of silicon dioxide on the silane flow. The values of the data plotted in this diagram can be found in the table B.7.

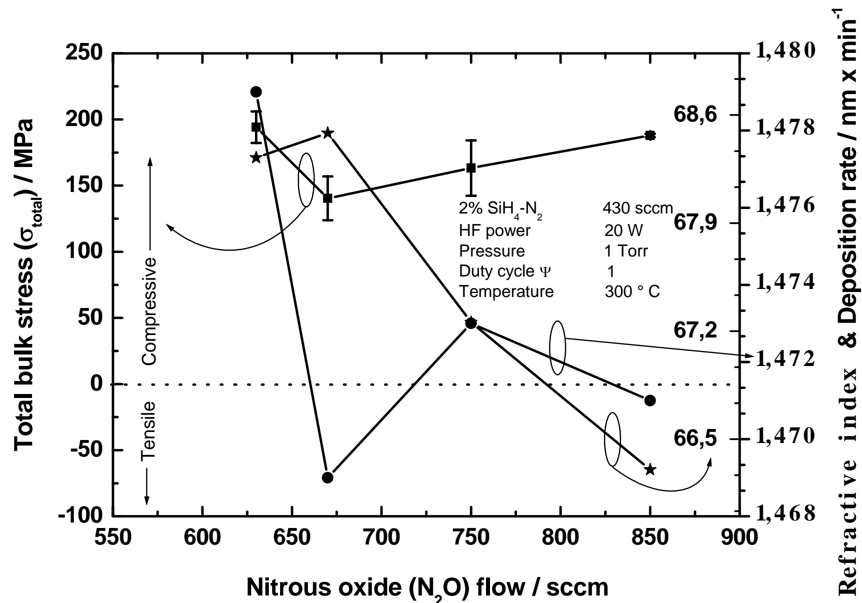

Figure 3.8: The dependence of the bulk stress σ_{total}, the refractive index n_{SiO_2} and the deposition rate of silicon dioxide on the nitrous oxide. The values of the data plotted in this diagram can be found in the table B.8.

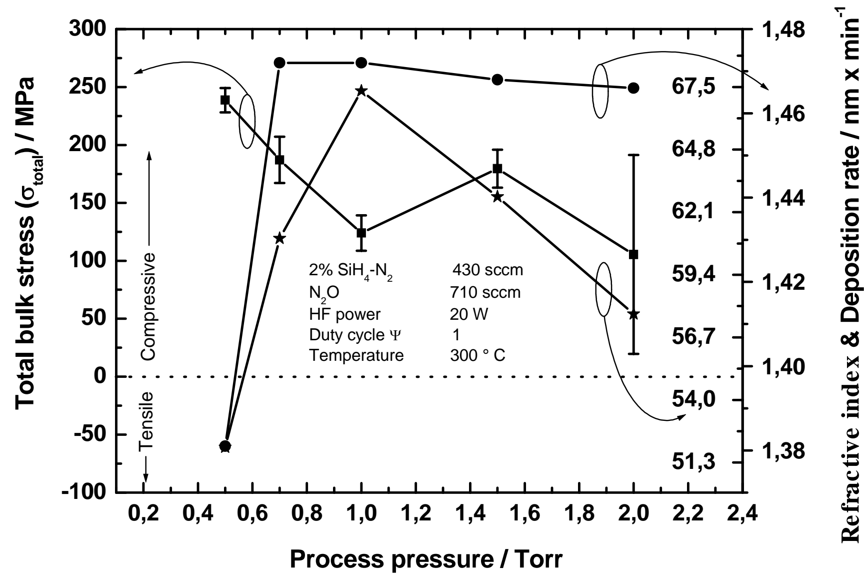

Figure 3.9: *The dependence of the bulk stress σ_{total}, the refractive index n_{SiO_2} and the deposition rate of silicon dioxide on the process pressure. The values of the data plotted in this diagram can be found in the table B.9.*

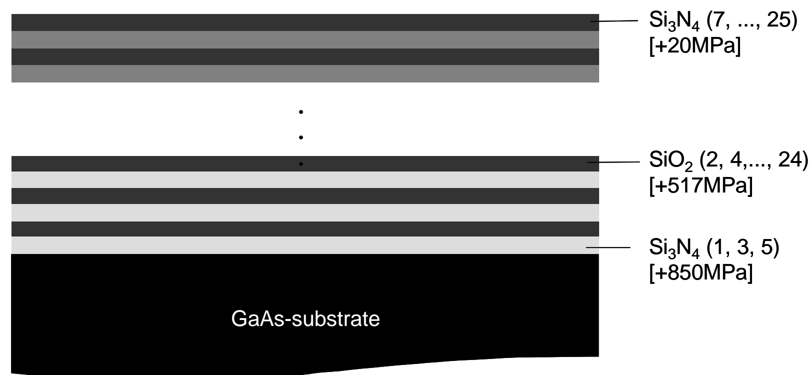

Figure 3.10: 12.5 *periods PECVD DBR implemented by differentely stressed silicon nitride and silicon dioxide layers.*

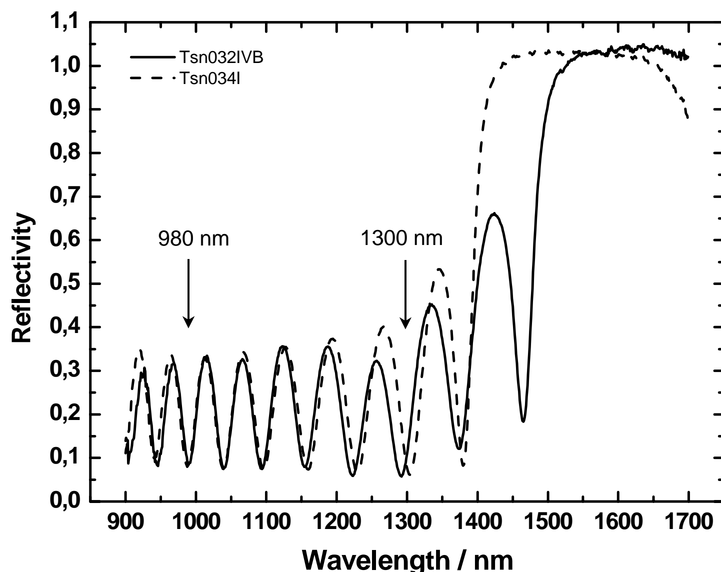

Figure 3.11: *Optical spectra of two DBRs with the same mechanical properties and different optical requirements.*

should not affect the optical properties of this DBR. By considering both, the optical investigation in this chapter and the mechanical study (see chapter 5), all requirements have been fulfilled. Figure 3.11 shows as an example the optical spectra of two DBRs, which have the same structure described in Figure 3.10. However, the first DBR (Tsn032IVB) is designed for an optically pumped VCSEL with a central wavelength of 1610 nm, whereas the second DBR (Tsn034I) is intended for the use in a VCSEL emitting at 1550 nm. Even though the stop band spectra are shifted to fulfill the optical requirements, the reflectivity of both DBRs at the pumping laser wavelengths (980 nm & 1300 nm) is very low, enabling a good coupling of the pumping light in the VCSEL. Furthermore, an optical pumping at 980 nm is also possible due to the low reflectivity of the DBR at this wavelength. After release, both membranes exhibit the same mechanical properties. This example, among several others, demonstrate the ability to control the optical and mechanical properties of the DBRs independently.

Chapter 4

Technology for air-gap based microcavity devices

4.1 Bulk and surface micromachining

For the implementation of MEMS and MOEMS, two different technological approaches are relevant: bulk micromachining and surface micromachining [78]. In the first case, e.g., backside etching of the substrate is necessary to form microstructures and free standing membranes. MEMS for optical communication systems are implemented based on this technology [79]. However, using bulk micromachining technology, only a single free standing membrane or a multi layer stack can be fabricated. In order to implement multiple free standing membranes (e.g. multi air-gap Fabry-Pérot filter [24]), surface micromachining, a totally different concept, is needed. For this, sacrificial layers are used to form microstructures from the deposited or grown thin films on the substrate. This involves several technological and fabrication steps [80]. Fabrication steps like lithography, dry etching, deposition, annealing, sputtering are well studied and controlled. Nevertheless, surface micromachining still presents a challenge since crucial techniques like wet chemical etching of the sacrificial layer, stiction and stress engineering of the released membranes have not been properly controlled up to now. Even though the sacrificial layer is removed during the structuring process, it plays a major role in determining the quality of the resulting microstructures. Thus, the sacrificial layer defines the geometrical and structural as well as the optical properties of the released membranes. In crystalline semiconductor systems, the sacrificial layer should be lattice matched to the grown films in order to avoid strain and fractures. Several microstructures involving sacrificial layers were implemented based on the III-V compound system [81–83]. For microstructures based on amorphous thin films, different materials can be used for the sacrificial layers [84–94]. After the release of the thin films by wet chemical etching of the sacrificial layer, two main technological phenomena lead to a malfunctioning of the structures: stiction and buckling. Stiction occurs due to capillary, electrostatic and Van der Waals forces as well as hydrogen bridging [95], whereas buckling occurs due to compressive intrinsic stress. Stiction can be avoided by using a CO_2 critical point drying techniques, which are commercially available. Buck-

ling control is the subject of active research and is thoroughly investigated later on in this thesis.

4.1.1 Photoresist based novel technology

For further investigations in this work, both bulk and surface micromachining are used. Applying surface micromachining, MEMS structures designed for stress evaluation (Figure 2.4) and process control are implemented. For this, the technology steps described in Figure 4.1 (a-d) are used: the wafer is first coated with a photoresist acting as sacrificial layer (Figure 4.1a). A PECVD process for a low temperature (60°C) deposition on the photoresist is developed. After the deposition of a dielectric layer at low temperatures (PECVD) (Figure 4.1b) on top of the photoresist, the lateral structure is lithographically defined. A reactive ion etching process using trifluromethane (CHF_3) and argon (Ar) is used to perform the vertical structuring (Figure 4.1c). Afterwards, the membrane is chemically underetched, wet or dry (Figure 4.1d), and remains fixed by the residual sacrificial layer parts underneath the larger supporting posts. The underetching process is isotropic and can be controlled by the etch time. The wet chemical underetching involves a solution of isopropanol and acetone followed by a CO_2 critical point drying process to avoid stiction of the suspended membrane. Dry chemical underetching is obtained by a microwave barrel O_2-plasma process.

Another technological approach, where the sacrificial layer can be completely removed is presented in Figure 4.1 (e-h). This technology is used for the tunable and non tunable optical devices presented in this work. After coating the substrate with an arbitrary photoresist (here AZ1518), an optical lithography step is used to define structures in this sacrificial layer (Figure 4.1e). In this case, the dielectric layer is deposited simultaneously, both on the photoresist and the substrate. Since the deposition is isotropic, the side walls of the photoresist are also coated with dielectric material (Figure 4.1f). The lateral and vertical structure definition (Figure 4.1g) is implemented by the same lithographic and dry etching steps used in the first approach. Finally, the photoresist can be removed completely since the membrane is still fixed by the coated holes defined by the first lithographic step (Figure 4.1h). The advantage of the second approach compared to the first one is that rapid thermal annealing can be used afterwards to reduce the material absorption. Furthermore, this approach has a higher process feasibility since it does not depend on the underetching time.

4.1.2 PECVD dielectric membrane

Based on the surface micromachining technologies described in Figure 4.1, free standing dielectric membranes are implemented. For this, different technological silicon nitride and silicon dioxide PECVD processes enabling a low temperature plasma enhanced deposition in a parallel plate reactor on common photoresist are developed. This deposition is crucial since the plasma and the ion bombardment could damage the photoresist. However, the processes were optimized enabling a smooth deposition.

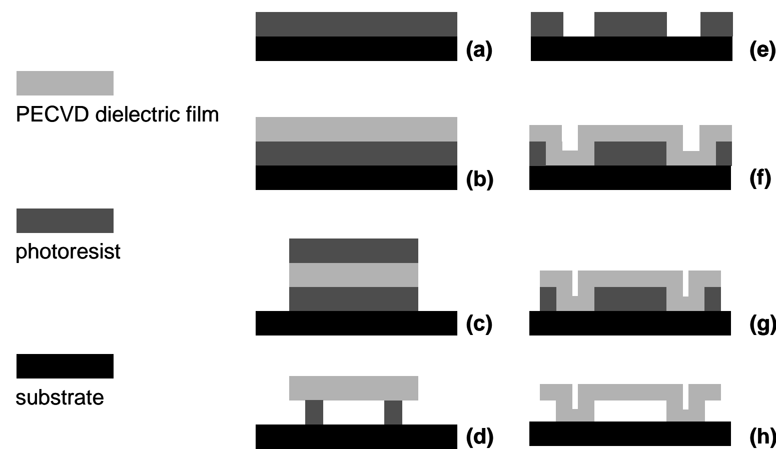

Figure 4.1: *Two technological approaches for implementing optical devices and stress evaluation MEMS structures. Both are based on surface micromachining. (a-d) the sacrificial layer is partially removed, (e-h) the sacrificial layer is completely removed.*

Figure 4.2(a) shows a silicon nitride membrane implemented according to the technological steps described in Figure 4.1 (a-d). The square membrane is positioned by four suspensions connected to supporting posts. The posts are fixed to the substrate by the residual photoresist sacrificial layer after the membrane release. A membrane implemented by the technology described in Figure 4.1 (e-h) is shown in Figure 4.2(b). The circular membrane and the suspensions are fixed by supporting posts with post holders. This technology enables the fabrication of suspended membranes with surface micromachining and a complete removal of the sacrificial layers by using a dry or wet chemical sacrificial layer etching.

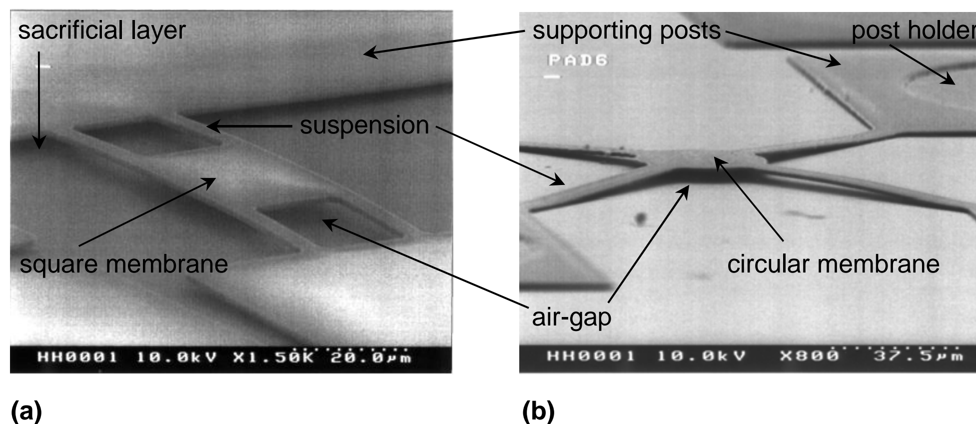

Figure 4.2: *Scanning electron micrographs of - (a) free standing silicon nitride membrane implemented by the technology described in figure 4.1(a-d). The supporting posts of this membrane are fixed by the residual sacrificial layer. (b) Silicon nitride membrane implemented by the second approach 4.1(e-h). The supporting posts are fixed by the post holders.*

These two scanning electron micrographs show that in both cases, stiction can be

avoided. However, the stress related buckling due to the intrinsic stress is observed in both cases. This buckling affects the mechanical (tuning) and the optical (cavity length, wave propagation, etc.) properties of the tunable optical devices. Therefore, complete control of the buckling is highly desired. This control problem is a main focus in this thesis (see chapters 5 and 6).

Chapter 5

PECVD stress engineering

5.1 Stress control of PECVD dielectric material

The material properties of dielectric material were described in chapter 3.2. Stress, composition, and optical properties of thin films were investigated by varying the common PECVD parameters such as temperature, pressure, and gas flow.

This chapter deals with the specific material stress engineering and the influence on the device relevant properties (cavity length, radius of curvature and filter characteristics). The stress contol is achieved by tuning the plasma excitation frequency.

The strain in crystalline semiconductors results from a mismatch in the lattice constant of two different materials. Thus, by varying the alloy composition of the crystalline material, the strain induced stress can be controlled. Unlike in semiconductor materials, the stress of amorphous materials is quite difficult to control, since no defined internal lattice structure is involved. Furthermore, the influence of the process parameters (e.g. gas flow, pressure, temperature, etc.) on the stress is negligible (see chapter 3). Generally, bulk stress control in dielectric amorphous layers can be achieved by tuning either the thermal or the intrinsic component. Changing the deposition temperature provides considerable composition changes in the stoichiometry of the layers. Therefore, it is highly preferable to tune the intrinsic part without changing the deposition temperature.

In this case, the plasma excitation frequency, which influences the ion bombardment energy, is the key parameter in controlling the material intrinsic stress [96, 97]. The influence of the frequency on the intrinsic stress of thin silicon nitride and silicon dioxide films was described in earlier studies [98]. It has been shown that at high frequencies (13.56 MHz) the stress of silicon nitride is tensile whereas at low frequencies (50 kHz) the stress is compressive. The lower the excitation frequency the more ions in the plasma are able to oscillate according to the alternating electric field and, hence, transfer energy to the growing silicon nitride film, causing a densification. Due to both, the "ion peening" process and the implementation of high energetic H^+ ions with low atomic mass into spaces in the growing film, the film will tend to stretch out with

respect to the substrate, and causes compressive stress. At high frequencies, not all the ions can follow the alternating field; there is less significant ion energy transfer, and the film is less dense and contains an amount of microvoids and hydrogen atoms. The resulting Si-N-H bonds tend to contract causing a tensile stress. On the other hand, studies showed that the stress of silicon dioxide is not strongly affected by the RF frequencies.

For the macroscopically averaged stress investigation, a PECVD is used for implementing thin silicon nitride and silicon dioxide films at low (60 °C) and high (300 °C) temperatures on silicon wafers. The homogeneous intrinsic bulk stress is adjusted by varying the duty cycle Ψ of the low (130 kHz) and the high (13.56 MHz) frequencies. The duty cycle Ψ is given in equation 5.1, where t_{HF} and t_{LF} represent the time periods of the high and low plasma excitation frequencies of one cycle during the deposition process, respectively.

$$\Psi = \frac{(t_{HF} - t_{LF})}{t_{HF} + t_{LF}} \tag{5.1}$$

All other parameters are kept constant throughout the investigation. Table 5.1 shows the deposition parameters of silicon dioxide and silicon nitride used for this investigation. The thermal stress of the deposited silicon dioxide and silicon nitride is calculated according to equation 2.62. For $E_{Si_3N_4} = 304$ GPa, $\nu_{Si_3N_4} = 0.24$, $\alpha_{Si_3N_4} = 3.3 \cdot 10^{-6}$ °C^{-1}, E_{SiO_2}= 73.1 GPa, $\nu_{SiO_2} = 0.17$, $\alpha_{SiO_2} = 0.5 \cdot 10^{-6}$ °C^{-1} and $\alpha_{Si} = 2.6 \cdot 10^{-6}$ °C^{-1}, the thermal stress of silicon nitride deposited at 300 °C and 60 °C is found to be −78.4 MPa (tensile) and −11.2 MPa (tensile), respectively. For silicon dioxide, the thermal stress is +51.78 MPa (compressive) at 300 °C and −7.4 MPa (tensile) at 60 °C.

Table 5.1: *PECVD process parameters for silicon nitride and silicon dioxide deposited at 300 °C and 60 °C for the stress investigation.*

Process parameters	$Si_3N_4:H_x$		SiO_2	
2% SiH_4–N_2 flow / sccm	1000	1500	430	430
NH_3 flow / sccm	20	5	0	0
N_2O flow / sccm	0	0	710	710
HF-power / W	20	20	20	20
LF-power / W	20	20	20	20
Duty cycle Ψ	Variable			
Temperature / °C	300	60	300	60
Pressure / torr	0.65	0.65	1	1

Using the set-up described in 2.2.2, the stress is measured along three directions on the wafer. For this, the one dimensional array of the reflected spot pattern is aligned along different directions (< 010 >, < 001 >, < 011 >) which refer to the

crystal structure of the substrate. The three resulting stress values are averaged and the standard deviations are taken as error bounds.

Figure 5.1 shows the total macroscopically averaged bulk stress of silicon nitride and silicon dioxide deposited at 300 °C. In this diagram, the stress is plotted as a function of the duty cycle of the plasma excitation frequencies. Three main regions of this diagram are interesting and correspond to the compressive (positive values), tensile (negative values) and low (±25 MPa) stress region. The total bulk stress of silicon nitride deposited at 300 °C is varied in a wide range between +850 MPa ($\Psi = -1$) compressive and −300 MPa tensile ($\Psi = 1$). Applications requiring stress free silicon nitride layers, corresponds to the region between $\Psi = 0.43$ and $\Psi = 0.54$. The total macroscopically averaged bulk stress of silicon dioxide shows, as expected, no strong dependence on the plasma excitation frequencies. The stress values of silicon dioxide deposited at 300 °C are for the most Ψ range nearly +200 MPa. This seems to be the result of the composition and the bonds morphology of the material. Regarding the thermal stress values, the intrinsic stress of silicon nitride deposited at 300 °C varies between +930 MPa and −220 MPa, whereas the intrinsic stress of silicon dioxide is approximately +150 MPa.

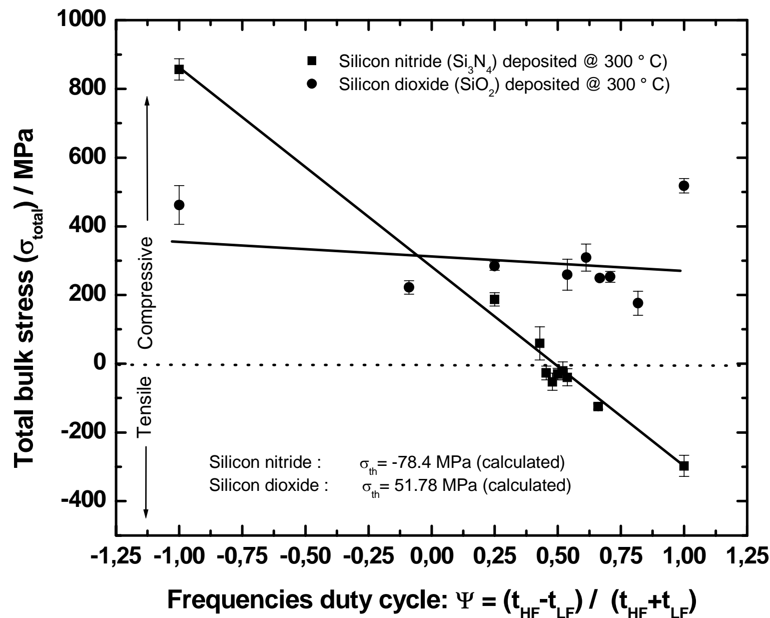

Figure 5.1: *The dependence of the total macroscopically averaged bulk stress of silicon nitride and silicon dioxide deposited at* 300 *°C on the PECVD plasma excitation frequencies (duty cycle* Ψ*).*

Similar stress measurements are performed on silicon nitride and silicon dioxide layers deposited at 60 °C. The total macroscopically averaged bulk stress is investigated in a range of $0.55 < \Psi < 0.61$, and varies from +121 MPa compressive ($\Psi = 0.55$) to −36 MPa tensile ($\Psi = 0.61$) (Figure 5.2). At this temperature, silicon dioxide shows a low thermal stress value of +7.4 MPa. Thus, an average value of +17 MPa can be deduced for the intrinsic stress.

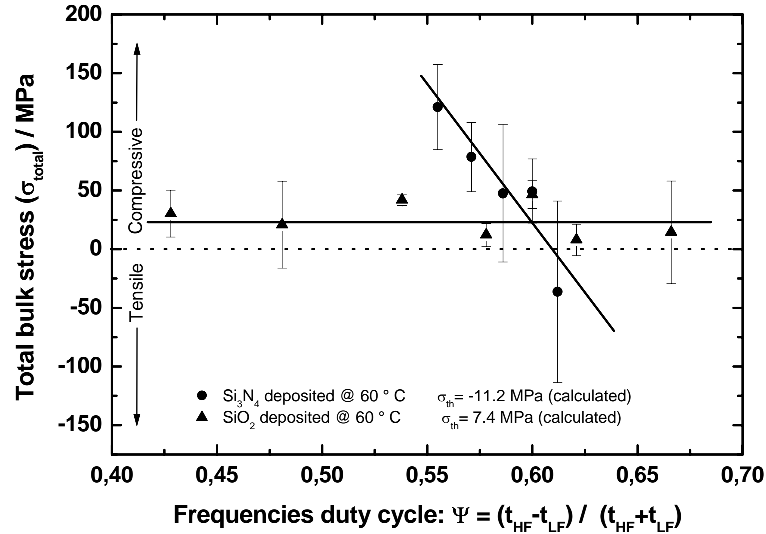

Figure 5.2: *The dependence of the total macroscopically averaged bulk stress of silicon nitride and silicon dioxide deposited at* $60\,^\circ C$ *on the PECVD plasma excitation frequencies (duty cycle* Ψ*).*

Macroscopically averaged stress results provide an overview of the stress in PECVD dielectric layers and enable coarse stress control in a wide range. However, this method of stress evaluation does not meet the requirements for microscale applications, since several crucial issues in the implementation of microdevices cannot be addressed by considering only the macroscopically averaged stress measurement. For example, inhomogeneities within the layers, as well as wafer border effects contributing to the averaged stress values, can not be distinguished. The effects of the layer interfaces (e.g. the sacrificial medium) and of the process steps on the stress are crucial in micromachined fabrication. Therefore, an in-process technology for monitoring the stress as a function of the lateral position with high spatial resolution (microscopically detected stress) is required.

For this purpose, the structures described in 2.2.2 are used. The microdetected stress is evaluated using equation 2.64, with $E_{SiO_2} = 73.1$ GPa, $E_{Si_3N_4} = 304$ GPa, $\nu_{SiO_2} = 0.17$, $\nu_{Si_3N_4} = 0.24$, $d_i = 10\,\mu$m (the distance between the anchor of the actuator beam and the center of rotation), l_a (value to be measured (approximately $500\,\mu$m), the length of the actuator beams), $l_i = 228\,\mu$m (the length of the indicator beams) and δ_i (the deflection between the two indicators). The lateral extension of the MEMS structure is given by $2l_a$ and $2l_i$.

Using these microstructures, the microdetected stress can be adjusted in a range of interest. Several structures were implemented by differently stressed silicon nitride and silicon dioxide layers deposited at low temperatures. Figure 5.3(a) shows a microscope image of such a MEMS structure fabricated from stress free silicon dioxide deposited at 60 °C. In this case, the perfectly facing two indicator beams indicate very low bulk stress in the lateral direction. The released actuators tend to neither expand nor to contract and thus, the indicators do not rotate. This result is in agreement with

macroscopically averaged stress measurements of silicon dioxide (Figure 5.2) showing low stress values.

However, in some cases, unexpectedly stressed structures implemented by the same material are observed. These structures were located close to the wafer border where the layer deposition is laterally inhomogeneous because of the "border effect". Figures 5.3(b) and 5.3(c) show such stressed silicon dioxide layers, with +70 MPa and +100 MPa, respectively. The released actuators expand due to the compressive bulk stress and thus rotate the indicators in clockwise direction.

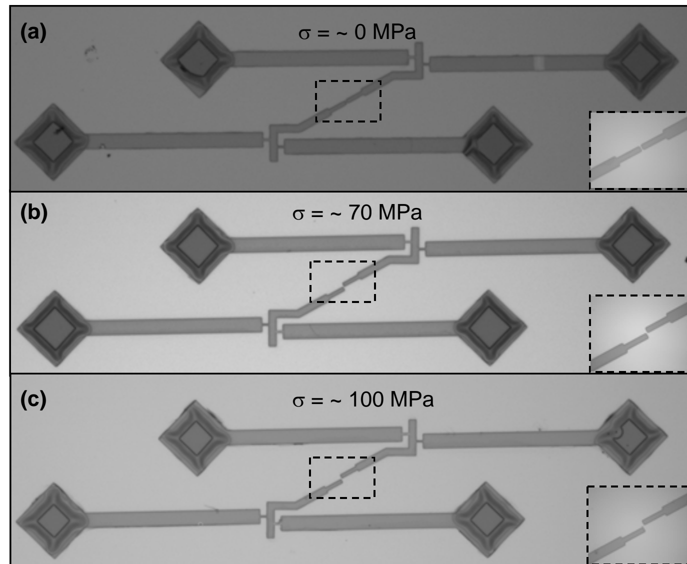

Figure 5.3: *MEMS structures for detecting silicon dioxide microstress at different lateral positions on the wafer. (a) silicon dioxide layer deposited at* 60 °*C with very low bulk stress. (b) and (c) show stressed layers with* +70 MPa *and* +100 MPa*, respectively.*

The microstress of silicon nitride deposited at 60 °C is also studied. Figures 5.4(a), (b) and (c) show stress detection microstructures implemented by silicon nitride layers deposited using different duty cycle values of $\Psi = -1$ (+130 MPa), $\Psi = 0.567$ (+715 MPa) and $\Psi = 0.588$ (+980 MPa), respectively.

For certain duty cycles Ψ, different local stress values are observed at different positions on the wafer. This stress variation can reach 15% for silicon nitride and 30% for silicon dioxide. A relation between the position of the MEMS structures on the wafer and the related stress is observed. However, this correlation is not due to physical effects such as crystal orientation and lattice mismatch; stability and reliability of the process, as well as homogeneity of the dielectric layers (thickness and density) strongly affect the lateral stress variation across the wafer. The sacrificial layer also plays a major role. These stress fluctuations (15% for silicon nitride and 30% for silicon dioxide) are deduced by studying several process runs. These deviations, which are detected by the microstructures, remain undetectable by the macroscopically averaged

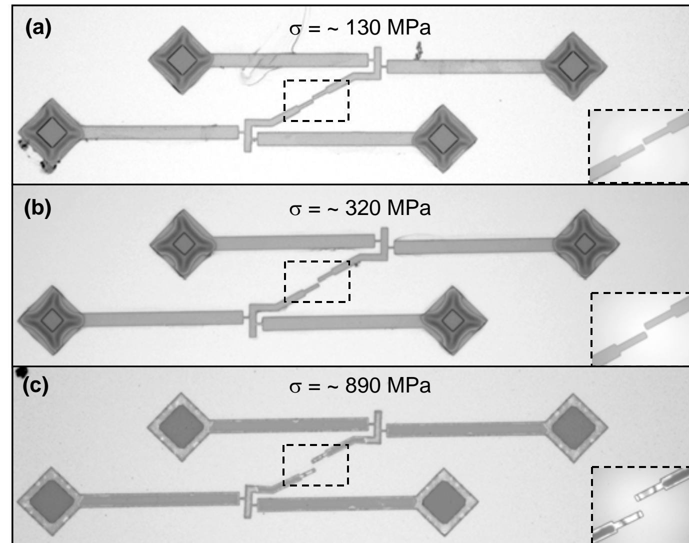

Figure 5.4: *MEMS structures for detecting silicon nitride microstress at different lateral positions on the wafer. (a) silicon nitride layer deposited at* 60 °*C with* +130 MPa *bulk stress. (b) and (c) show stressed layers with* +320 MPa *and* +890 MPa*, respectively.*

stress measurement techniques. Therefore, the local stress evaluation is of utmost importance when implementing microdevices.

The detected microstress and the averaged macrostress are correlated, in the sense that the average of the sum of all microstress values along one direction should agree with the measured macrostress value (for this direction). In order to compare these two methods, a weakly stressed silicon dioxide layer on silicon substrate ($\Psi = 0.481$) is considered, since relative stress fluctuations can be detected more precisely at small absolute stress values. The macroscopically averaged stress is measured along three directions on the wafer ($< 100 >, < 111 >, < 110 >$) corresponding to the defined angles of the measurement set-up ($0°, 45°$and $90°$), respectively (Figure 5.5). The standard deviation of these three measurements are included as error bounds. The microscopically detected stress is measured on different closely neighboring points on the wafer. The stress average value of points within the narrow area defining one direction is compared to the corresponding macrostress. In this case, error bounds are formed from standard deviation of many points within this area and stress values of microstructures located close to the wafer border are considered.

Figure 5.5 shows the results of this comparison. It can be seen that the microscopically detected and macroscopically averaged stress values do not differ significantly, and thus macroscopically averaged stress method will be sufficient for stress estimation. Microscopic stress detection, on the other hand, seems to be a reliable low cost method to generate process control structures for precise stress evaluation and for detecting the inhomogeneity in various defined positions on the wafer close to the microdevices. Finally, fabrication tolerances and requirements of the micromachining applications dictate the choise of micro- or macrostress detection measurement techniques.

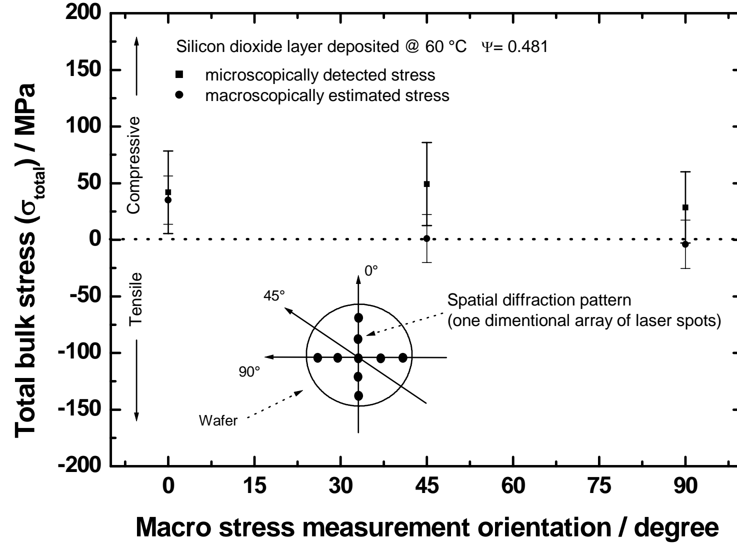

Figure 5.5: *Evaluation of the correlation between the microstress detection and the macrostress averaging by considering a low stressed silicon dioxide layer deposited at* 60 °*C.*

5.2 Impact of stress on optical and mechanical layer properties

The impact of stress on released membranes in air-gap microcavities is highly significant and may affect the functionality of the devices. Thus, optical characteristics in air-gap microcavity devices (Fabry-Pérot filters, VCSELs, detectors, etc.), such as tuning efficiency and light coupling factor in the cavity, are strongly affected by the mechanical behavior of the suspended membranes. Sophisticated novel devices, such as tunable air-gap VCSELs, involve several complex correlations and require careful adjustments of their optical properties (e.g. gain profile, wave propagation, light coupling and tuning efficiency) and their mechanical properties (e.g. cavity length, shape and ROC). For instance, the optical excitation of these devices is strongly dominated by the shape of the suspended membrane [99]. Thus, successful implementation of such devices requires precise tailoring to achieve the best agreement on all these properties. The geometry and the stress in the microstructures (membranes) influence several highly relevant device characteristics, such as L_{cav}, ROC, $FWHM$ as well as the resonance frequency (channel selection). These device characteristics can thus be adjusted by varying the geometry and the stress in the microstructures.

For this purpose, Fabry-Pérot air-gap filter devices[1] consisting of 5 periods of Si_3N_4−H/SiO_2 bottom DBR and 5.5 periods Si_3N_4−H / SiO_2 suspended DBR membrane are implemented. The effect of the design of these devices on the mechanical and optical properties is investigated using two geometries (Figure 5.6). The membrane described in Figure 5.6(a) is implemented by the technology previously described in Figure 4.1(e-h), whereas the membrane in Figure 5.6(b) is fabricated by the technolo-

[1] The technological implementation of these devices is shown in details in appendix B.

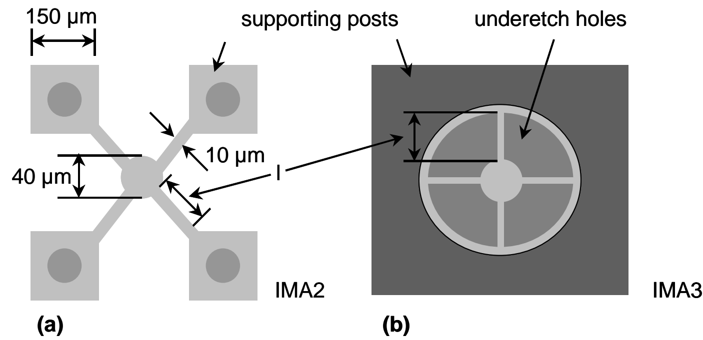

Figure 5.6: *Shematic top view of the two membrane designs. (a) by using the mask set IMA2 (technology described in figure 4.1(e-h)) and (b) by using the set IMA3 (technology described in figure 4.1(a-d)).*

gical approach in Figure 4.1(a-d). Two mask sets are therefore necessary: IMA2 [100] and IMA3 [101], which correspond to the membranes in Figures 5.6(a) and 5.6(b), respectively. The circular membrane (40 μm diameter) is fixed (in the lateral plane) by four suspensions of 10 μm lateral width. The length of the suspensions varies between 10 μm and 80 μm for the mask set IMA2 and between 10 μm and 60 μm for IMA3. In the case of IMA2, the suspensions are connected to four square shaped supporting posts of $150 \cdot 150\,\mu\text{m}^2$. Figure 5.7 shows a three dimensional view of a membrane implemented by using the mask set IMA2.

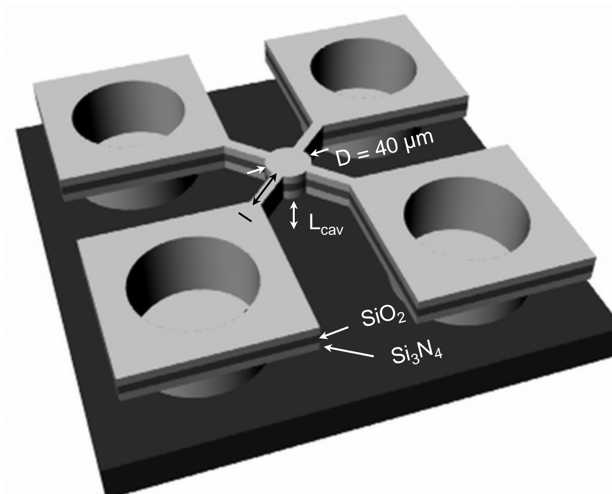

Figure 5.7: *Three dimensional view of the Fabry-Pérot filter membrane implemented by the mask set IMA2.*

5.2.1 Cavity length

Cavity length control is achieved in this case by varying the geometrical design (e.g. suspension lengths) and the stress gradient in the layers for both mask sets. Since the stress of silicon dioxide is weakly affected by the duty cycle Ψ, only the stress of silicon nitride is varied. The variation of Ψ throughout the investigation in this chapter is related to the duty cycle variation during the silicon nitride deposition. Using different combinations of these parameters, a wide range of passive cavity tuning is achieved. The term passive cavity tuning is defined in this thesis as the tuning by means of different parameters for several devices (i.e. not by micromechanical actuation).

Figure 5.8 shows the dependence of the cavity length L_{cav} on the suspension length l at different Ψ values for the membrane design IMA2. The cavity length, measured using the white light interferometry, can be varied in a wide range between 360 nm (l=10 μm and $\Psi = -1$) and 12.8 μm (l=80 μm and $\Psi = 0.25$). Normally, for a positive stress gradient, the cavity length should increase with increasing suspension length; consequently, a decrease in the cavity length with increase in suspension length should be observed if the stress gradient is negative. However, it is very difficult in our case to correlate the cavity length only with the stress gradient, because the geometry and the motion dynamics of the membrane when this is released play a major role.

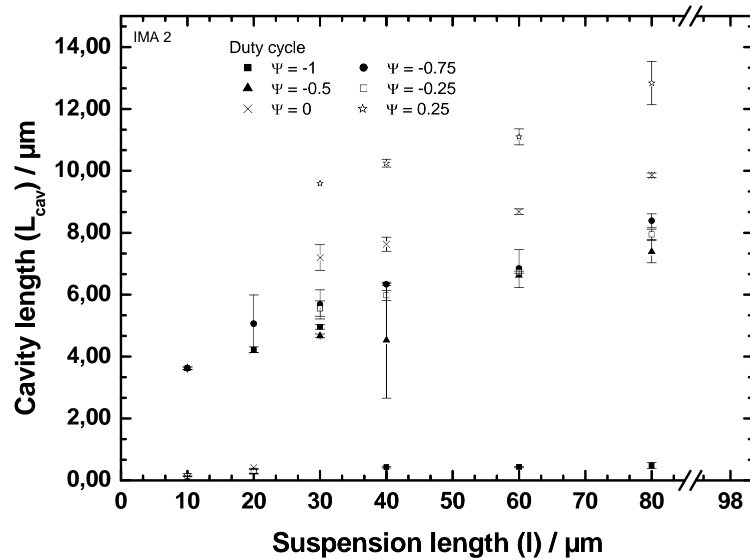

Figure 5.8: *The dependence of the cavity length L_{cav} on the suspension length l at different duty cycle (Ψ) values of silicon nitride. The filters are implemented using the design IMA2 and consist of a cavity embedded between two bottom and top DBRs of 5 and 5.5 periods (Si_3N_4 / SiO_2), respectively.*

The motion dynamics during the release of a membrane are extremely complicated and require highly sophisticated theoretical models in order to be understood. These theoretical model based calculations are not within the scope of this thesis. Nevertheless, these dynamics can be explained empirically by studying a relatively simple membrane. Figure 5.9 shows such a released membrane implemented by the design

IMA2 and consisting of three supporting posts and suspensions. A break in symmetry is introduced in order to study the effect of the geometry on the released membrane. The membrane is held by three suspensions that are attached to the three supporting posts (1,2 and 3). While two suspensions are symmetrically attached to the corners of supporting posts (2) and (3), the third suspension is connected to the middle of the edge of supporting post (1).

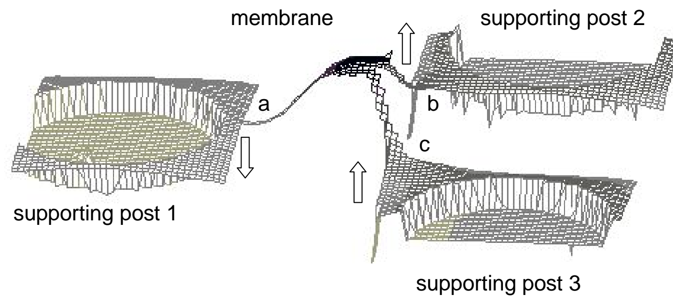

Figure 5.9: *A released membrane implemented by the mask set IMA2. The membrane is unsymmetrically supported by three suspensions connected to edge a and corners b and c.*

When the membrane is in a state of static equilibrium (Figure 5.9), two main observations can be made. First, the membrane is bent upwards, and second, the stress gradient of the supporting posts (1, 2 and 3) is negative and all edges (except the ones which are connected to the suspensions (2 and 3)) tend to pull down towards the substrate. Corners (b) and (c) show a positive gradient, whereas the gradient of border edge (a) is negative. In this case, it is difficult to find out whether the structure exhibits a positive or a negative gradient.

When the membrane is released, independent of the geometry of the membrane, two scenarios are possible for the stress distribution along the vertical structure of the membrane:

- a distribution with a negative gradient
- a distribution with a positive gradient.

In the first scenario, where the gradient is negative, the released areas of the supporting posts of the membrane tend to pull down towards the substrate. However, due to the length of the suspensions, it may happen that the membrane reaches the substrate without finding a relaxation optimum, which forces the membrane to deflect upwards, searching for an equilibrium. In this case, the corners (b) and (c), where the deflection forces are weak due to the small area, deflect upwards. Border edge (a) of the supporting post (1) still deflects downwards because of the enormous forces applied to it. Figure 5.9 shows the equilibrium status in this case. Here, it is important to note that, depending on the stress distribution, several equilibriums are possible.

In the second scenario, the stress gradient is positive and the deflection is upwards. Corners (b) and (c) and the membrane deflect upwards after the release. Because the

suspensions are not long enough for the system to reach an equilibrium, the suspension connected to border edge (a) pulls down forcing this border downwards. An equilibrium is then reached. However, this scenario is less probable due to two main facts. First, the other edges and corners should exhibit a positive gradient and pull upwards and second, corners (b) and (c) should pull downwards first due to their small mechanical resistance. This is indeed not the case, and thus it can be concluded that the gradient is negative.

Figure 5.10 shows the relationship between the suspension lengths and the cavity length at different Ψ values for the design IMA3. For this design, the absolute cavity length variations are smaller than for IMA2. The smaller absolute passive tuning of the cavity length is due to the dimension of the supporting posts. For design IMA3, the area of the supporting posts is bigger and thus, they are less influenced by the stress than are those of IMA2.

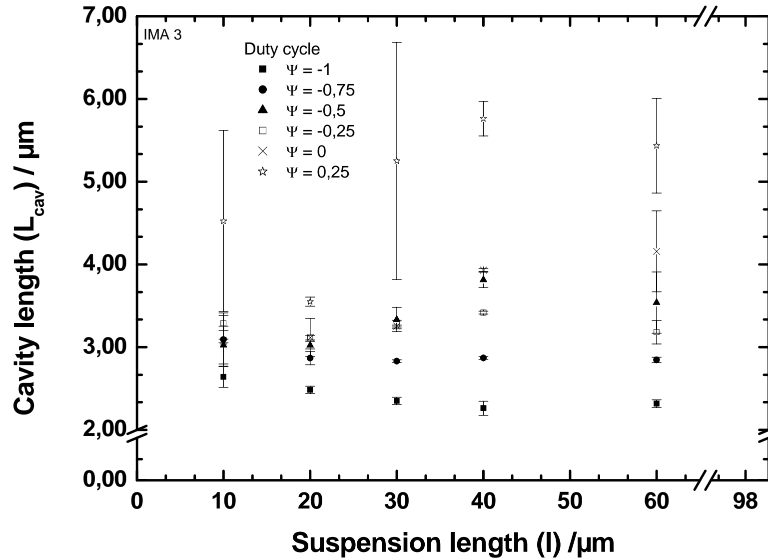

Figure 5.10: *The dependence of the cavity length L_{cav} on the suspension length l at different duty cycle (Ψ) values of silicon nitride. The filters are implemented using the design IMA3 and consist of a cavity embedded between two bottom and top DBRs of* 5 *and* 5.5 *periods* (Si_3N_4 / SiO_2)*, respectively.*

Even though these results demonstrate the capability of a passive cavity length tuning and control over a wide range, accurate predictions can only be made using theoretical dynamic model calculations. The dependence of the cavity length of the Fabry-Pérot filters implemented by both designs, IMA2 and IMA3, on the silicon nitride duty cycle Ψ at different suspensions length l can be found in appendix F.

5.2.2 Radius of curvature

The stability of a Fabry-Pérot resonator was discussed in detail in chapter 2. It was shown that the radius of curvature of the membranes is very important for the function-

ality of the devices. Furthermore, the shape of the membrane is extremely important at a certain ROC absolute value. Thus, adjusting the ROC and the shape simultaneously, is a main goal of novel optoelectronics. To my best knowledge, no publications dealing with the passive tuning of the shape and the ROC of the membranes exist.

By applying the same technology and designs as in the investigation of the cavity length, the shape and the ROC are tuned passively in a wide range. Figures 5.11 and 5.12 show the dependence of the ROC on the suspension length and on the duty cycle Ψ for the designs IMA2 and IMA3. Three possible membrane shapes are included in the Figures:

- flat membranes
- concave membranes
- convex membranes.

Flatness of the membrane can approximated by either low concavity or low convexity. The design IMA3 (Figure 5.12) enables a wider ROC range tuning than the IMA2 design. However, control of the ROC in the design IMA2 is more precise. Here, the ROC is controlled between -0.994 mm and $+2.718$ mm, whereas $+110\,\mu$m convex and $-548\,\mu$m concave membranes are reached. In the case of IMA3 design, the ROC is controlled between -8.746 mm and $+15.17$ mm reaching $+183\,\mu$m convex and -1.8 mm concave membranes.

The dependence of the radius of curvature of the filter membranes for the designs IMA2 and IMA3 on the duty cycle Ψ at different suspensions length can be found in appendix F.

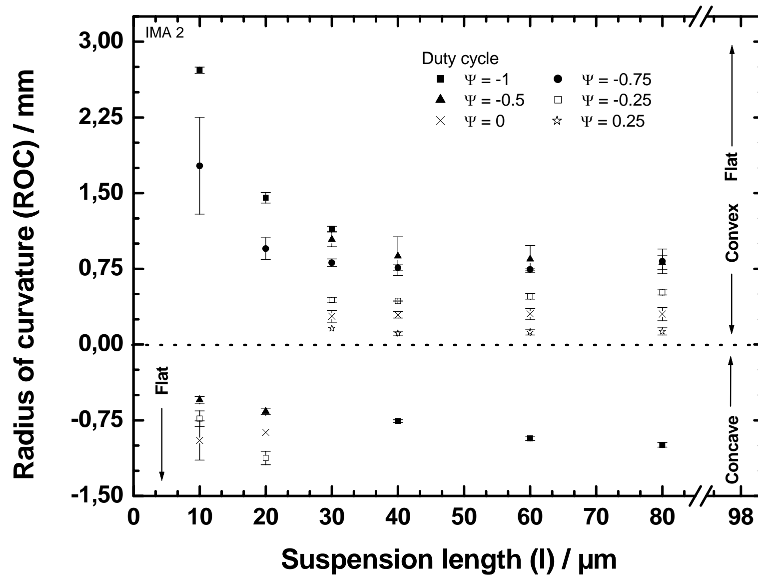

Figure 5.11: *The dependence of the radius of curvature ROC on the suspension length l at different duty cycle (Ψ) values of silicon nitride. The membrane is implemented using the design IMA2 and consists of* 5.5 *periods (Si_3N_4 / SiO_2).*

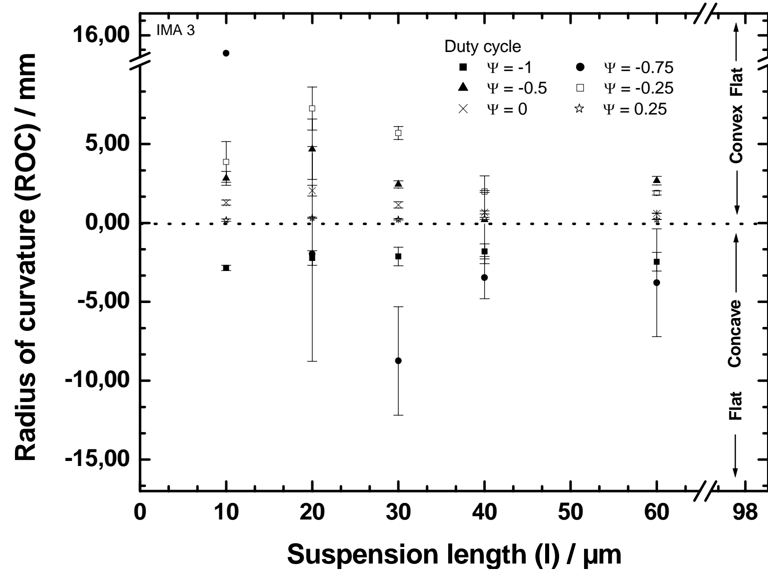

Figure 5.12: The dependence of the radius of curvature ROC on the suspension length l at different duty cycle (Ψ) values of silicon nitride. The membrane is implemented using the design IMA3 and consists of 5.5 *periods* (Si_3N_4 / SiO_2).

5.2.3 Filter characteristics

The full width at half maximum (FWHM) is an essential parameter when evaluating a Fabry-Pérot filter. Lower values of the FWHM are needed for precise channel selection in DWDM systems, while higher values are required for other applications. From the industrial and commercial point of view, it is desirable to implement filters for several wavelengths with different FWHM using the least technological investments, costs and time. These points are investigated during this thesis. The first results show that by varying the design (here, IMA2 and IMA3), the suspension length (l) and the stress (here by using Ψ), a wide range of the FWHM and the resonance wavelengths can be achieved by a single batch process.

Figures 5.13 and 5.14 show the dependence of the FWHM on the suspension length and stress (by varying the duty cycle Ψ) for the designs IMA2 and IMA3. For the design IMA2, the FWHM varies between 1.5 nm and 64.25 nm. The design IMA3 enables a FWHM variation between 2.75 nm and 44.25 nm. However, these FWHM are not deduced from resonances of fixed wavelengths. The dependence of the FWHM of the filters implemented by the designs IMA2 and IMA3 on the duty cycle Ψ for different suspension lengths l can be found in appendix F.

The variation of the resonance wavelength for both designs, IMA2 and IMA3, is seen in Figures 5.15 and 5.16, respectively. For the first design, the resonance wavelength is varied between 1455 nm and 1595.75 nm, whereas the variation in the second case is between 1450 nm and 1649 nm. The wavelength span is $\Delta\lambda_{IMA2} = 140.25$ nm for the design IMA2 and $\Delta\lambda_{IMA3} = 199$ nm for the design IMA3. The dependence of the

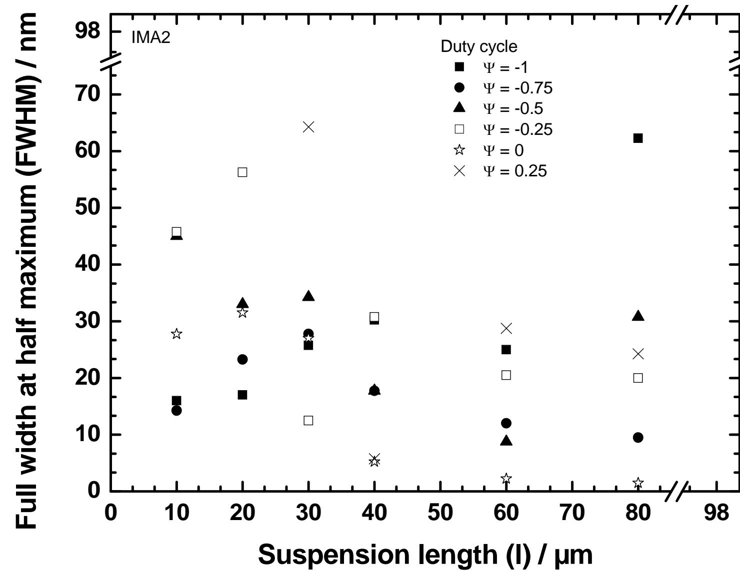

Figure 5.13: *The dependence of the FWHM of the filters on the suspension length l at different duty cycle (Ψ) values of silicon nitride. The filters are implemented using the design IMA2 and consist of a cavity and two bottom and top DBRs of 5 and 5.5 periods (Si_3N_4 / SiO_2), respectively.*

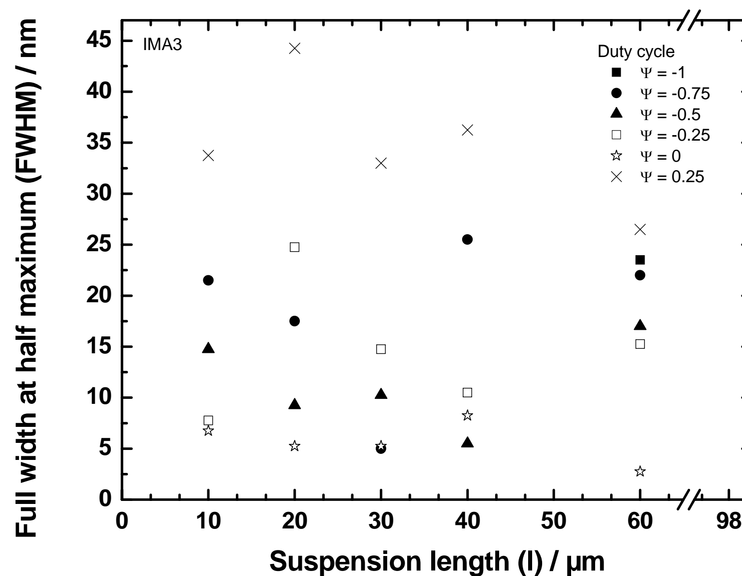

Figure 5.14: *The dependence of the FWHM of the filters on the suspension length l at different duty cycle (Ψ) values of silicon nitride. The filters are implemented using the design IMA3 and consist of a cavity and two bottom and top DBRs of 5 and 5.5 periods (Si_3N_4 / SiO_2), respectively.*

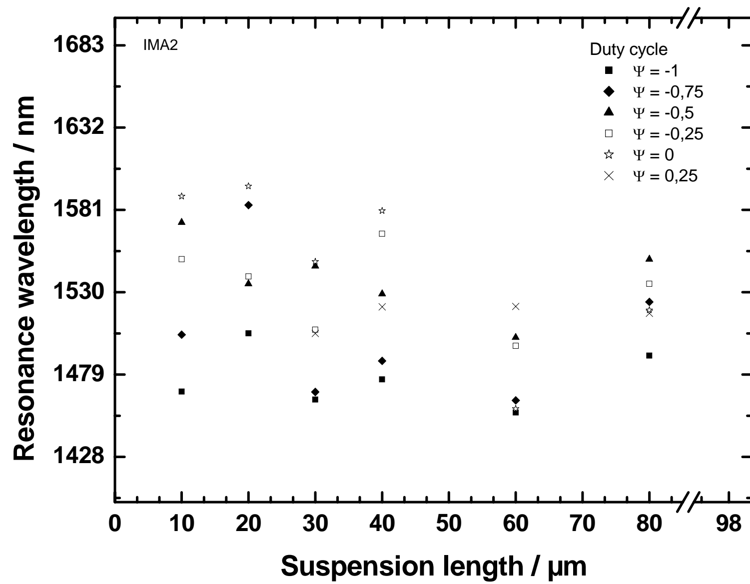

Figure 5.15: *The dependence of the resonant wavelengths of the filters on the suspension length l at different duty cycle (Ψ) values of silicon nitride. The filters are implemented using the design IMA2 and consist of a cavity and two bottom and top DBRs of* 5 *and* 5.5 *periods* (Si_3N_4 / SiO_2)*, respectively.*

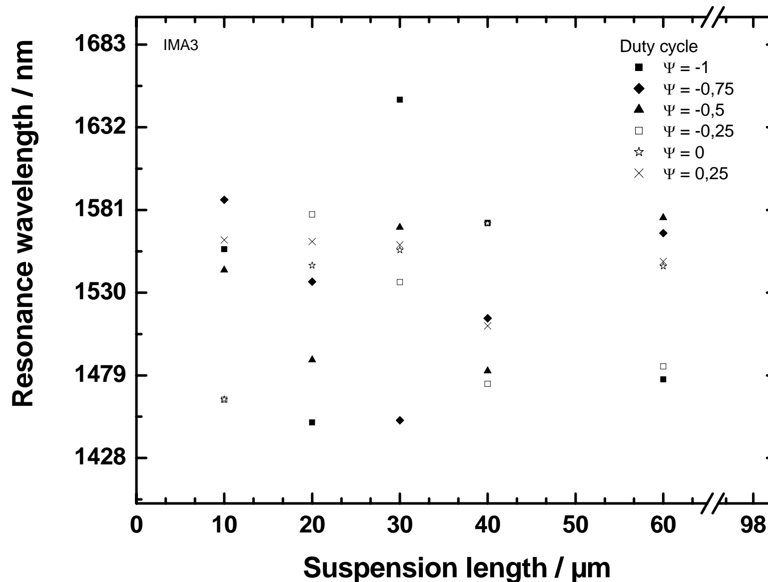

Figure 5.16: *The dependence of filters resonant wavelength on the suspension length l at different duty cycle (Ψ) values of silicon nitride. The filters are implemented using the design IMA3 and consist of a cavity and two bottom and top DBRs of* 5 *and* 5.5 *periods* (Si_3N_4 / SiO_2)*, respectively.*

resonance wavelength of the filters for the designs IMA2 and IMA3 on the duty cycle Ψ at different suspensions length l can be found in appendix F.

Figure 5.17 shows white light interferometer pictures of differently shaped membranes. A concave membrane shape with $ROC = -0.31\,\mathrm{mm}$ is shown in Figure 5.17 (a), a flat membrane with $ROC = -184.71\,\mathrm{mm}$ in Figure 5.17 (b) and a convex one with $ROC = 0.19\,\mathrm{mm}$ is shown in Figure 5.17 (c).

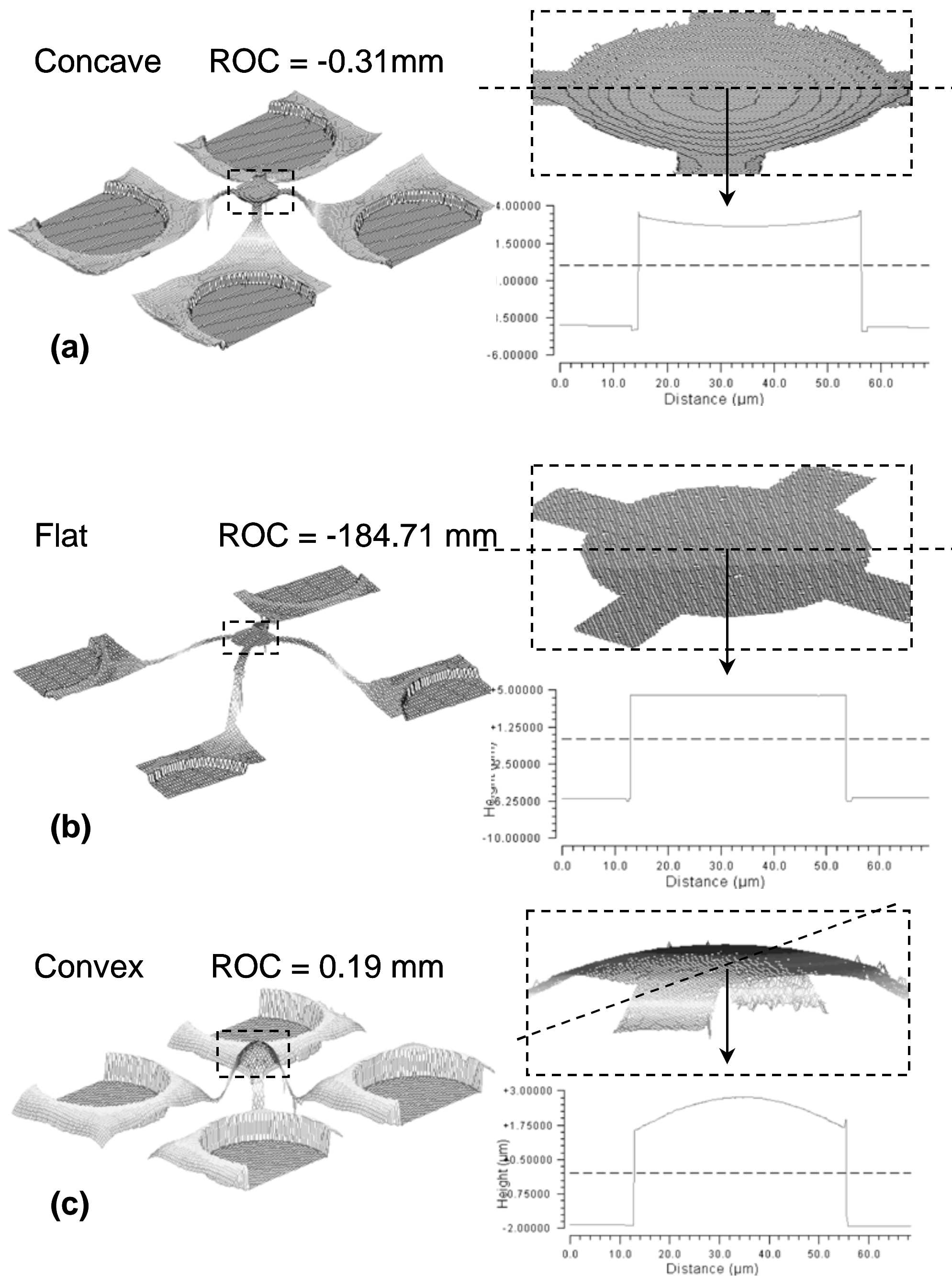

Figure 5.17: White light interferometer pictures of a concave (a), flat (b) and convex (c) suspended dielectric DBR membrane.

Chapter 6

Results of microcavity devices

6.1 Non tunable Fabry-Pérot filter

6.1.1 Solid stack filters

Figure 6.1 shows the optical spectrum of a solid dielectric filter. The Fabry-Pérot filter is implemented by the PECVD at a temperature of 300 °C. It consists of a Si_3N_4 cavity (1λ optical length) embedded between two Si_3N_4/ SiO_2 DBRs. The bottom DBR consists of 7.5 periods of $\lambda/4$ (optical length) alternating layers, whereas the top DBR comprises 8 periods of the same material. The technological data of the filter can be found in appendix B.

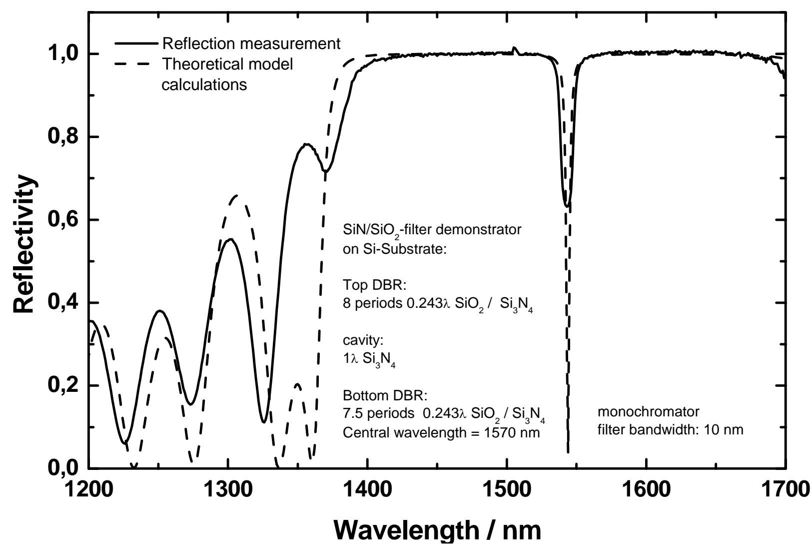

Figure 6.1: *Optical measurements and theoretical model calculations of a solid dielectric Fabry-Pérot filter deposited at* 300 *°C. The filter consists of a λ Si_3N_4 cavity, a bottom and top DBR of* 7.5 *and* 8 *periods, respectively. The design wavelength is* 1550 nm*. The monochromator resolution is* 10 nm*.*

The filter exhibits resonance at 1544 nm. At the resonance wavelength, contrary to the theoretical prediction, the reflectivity seems to be only attenuated from 1 to 0.63.

This effect is due to the monochromator resolution of the optical spectrum analyzer, which is only 10 nm in this case. Thus, the filter line is not fully resolved.

Figure 6.2 shows the characteristics of the filter measured at another position of the chip using a better monochromator resolution. Theoretical model calculations have been used to fit the filter optical spectrum; by using 0.243λ instead of 0.25λ for the optical length of the DBR layers, a good match between the measured data and the theoretical values has been obtained. This shift in the thicknesses is due to the PECVD process shift and can be corrected by using an in-situ ellipsometer, for example.

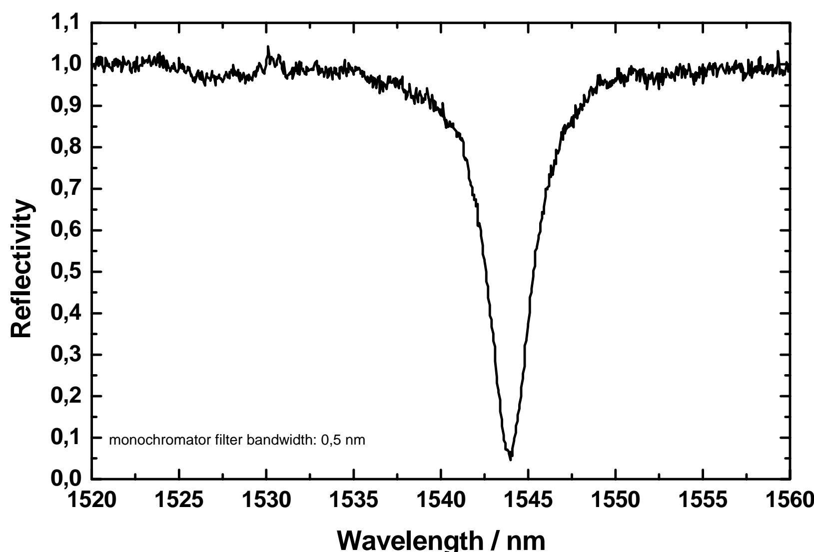

Figure 6.2: *Fabry-Pérot filter characteristics measured by using a high resolution (*0.5 nm*) of the optical spectrum analyzer monochromator.*

6.1.2 Air-gap filter

Based on the technology described in chapter 4 (Figure 4.1(a-d)), and using the design IMA3, an air-gap dielectric filter is implemented. The technological process used for the implementation of the air-gap filter is described in appendix B. The filter consists of two DBRs embedding an air-gap cavity. The bottom DBR is implemented at 300 °C and consists of 5 periods of Si_3N_4 / SiO_2. The top DBR is implemented by 5.5 periods of Si_3N_4 / SiO_2 deposited on a photoresist sacrificial layer (TI35ES) at 60 °C. After releasing the top membrane, the cavity length increases due to the stress induced buckling.

Figure 6.3 shows the spectrum of a filter (Tsn074II4) measured in transmission by the measurement set-up described in [102]. The filter membrane is positioned by four suspensions of 10 μm length. In this case, the cavity length is 3.54 μm (including the initial 2.1 μm thickness of the sacrificial layer) and the ROC is 1.92 mm. The transmission value of the filter is expressed in dB and the insertion loss of the filter is -0.19 dB. Reflection measurements and the calculated transmission (1-reflection) of two other filters (Tsn072II1V30X4Y3 and Tsn072II1V40X3Y2), also plotted in Figure

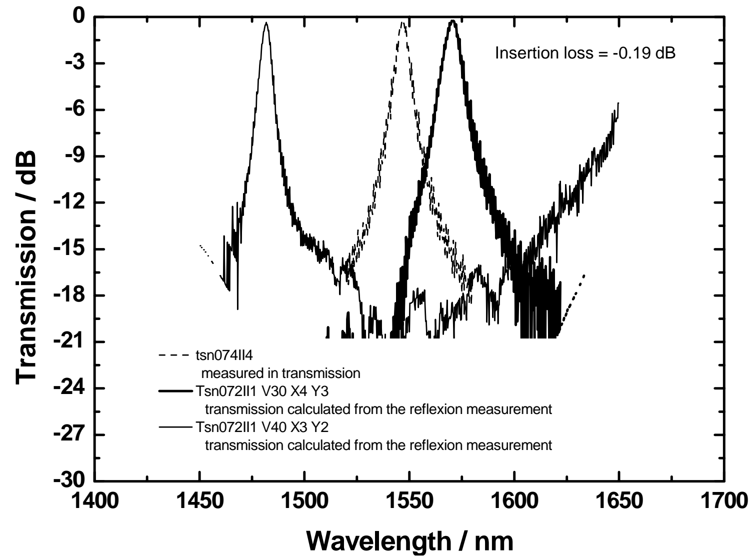

Figure 6.3: Optical spectra of air-gap Fabry-Pérot filters measured in transmission (Tsn074II4) and reflection (Tsn072II1V30X4Y3 and Tsn072II1V40X3Y2). The insertion loss of the filter Tsn074II4 is -0.19 *dB.*

6.3, show that the absorption is very low. Figure 6.4 shows the transmission and reflection characterization of the filter. The FWHM of the filter is 5 mm.

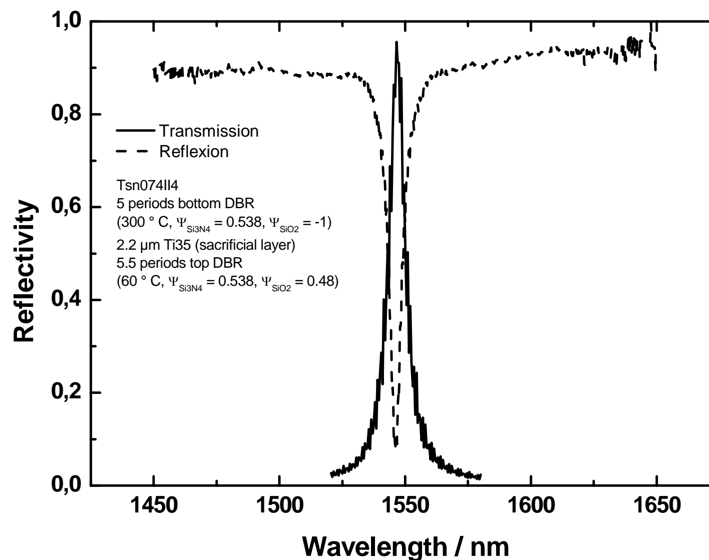

Figure 6.4: Measured optical spectra of the filter Tsn074II4. The transmission and reflection of the filter are compared. The filter exhibits a FWHM of 5 nm*.*

6.2 Tunable Fabry-Pérot filter

The technological approach used for the implementation of the tunable device is described earlier in chapter 4 (see Figure 2.4 (e-h)). Tuning of the device is achieved by an electrothermal actuation of the top membrane using microheaters placed on the top of the membrane. The vertical structure of the dielectric filters is similar to those described in 6.1.2. The upper DBR consists of 5.5 periods of $\lambda/4$ layers of Si_3N_4 and SiO_2, while the lower one comprises 5 periods. A detailed description of the technological implementation process can be found in appendix B. Figure 6.5(a) shows a microscopic top view picture of the filter. The membrane is supported by four suspensions of 40 μm length. A 100 nm Chromium thin film is sputtered on the top DBR and is wet chemically etched to define the meander like heaters (Figure 6.5(b)). After release of the top DBR using an O_2 plasma, the membrane bends upwards and increases the air-gap cavity length to 5.12 μm (Figure 6.5(c)). The radius of curvature of the circular membrane is 1.94 mm. The gradient stress of the whole upper DBR is calculated to be 307 MPa / μm, as a first approximation, by analyzing the upwards bent cantilevers (test structures near to the device) according to equation 2.65.

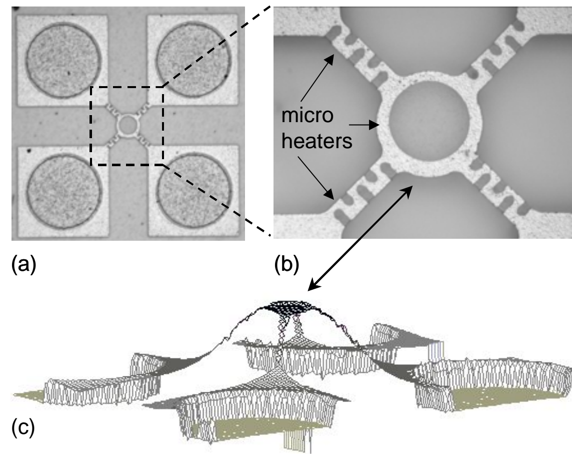

Figure 6.5: *(a) Microscopic top view picture of the tunable air-gap Fabry-Pérot filter (IMA2), (b)* 100 nm *thick meander like chromium microheaters on the top of the released DBR, (c) white light interferometry picture of the air-gap filter.*

Figures 6.6(a) and 6.6(b) show SEM micrographs of the tunable filter and the micro Chromium heaters on the suspensions and on the membrane borders, respectively. The filter exhibits a tunability of 15 nm / mA at a microheater resistance of 2 kΩ. Due to the low number of DBR periods, the filter exhibits a FWHM of 8 nm. The FWHM can be improved by increasing the number of DBR periods [103].

The spectral reflectivity (Figure 6.7 (a)) of the filter was measured using a single mode fibre set-up [102], an optical spectrum analyzer and an Erbium doped fibre amplifier (spectral range: 1.45 μm to 1.65 μm). In the spectral range studied, the

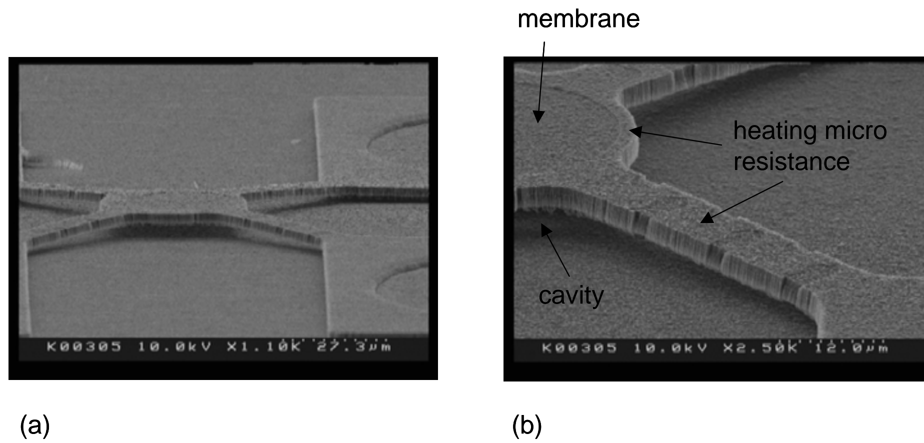

Figure 6.6: Scanning electron micrographs of: (a) the tunable Fabry-Pérot filter, (b) the released top DBR with the meander like chromium microheaters.

wavelength varies linearly with the heating current (Figure 6.7 (b)) and thus deliver a linear tuning characteristic.

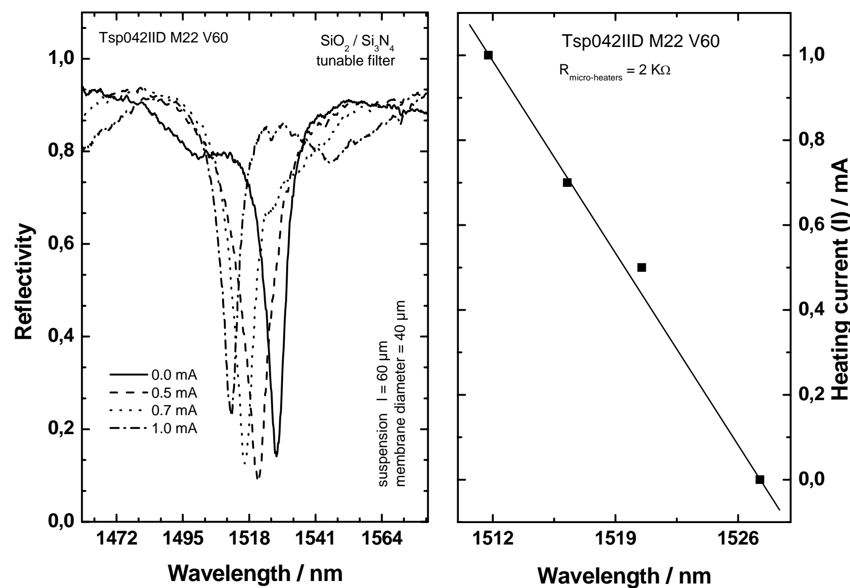

Figure 6.7: (a) Spectral characteristics of the tunable dielectric air-gap filter (measured in reflection), (b) the linear tuning characteristic.

6.3 Non tunable VCSELs

The non tunable VCSEL structure consists of an active region embedded between two PECVD dielectric DBRs. The DBRs are deposited at 300 °C using the parameters listed in table C.7. The bottom DBR, starting with SiO_2, comprises 12.5 periods of Si_3N_4 / SiO_2. The top DBR consists of 12 periods and is closed by a Si_3N_4 layer, enabling a high refractive index contrast to the air. The technological fabrication process of the VCSEL is described in Figure 6.8. The monolithic III-V (InP/InGaAsP) semiconductor structure is grown by metal organic vapor phase epitaxy in an Aixtron 200/4 reactor using Trimethylindium (TMIn), Trimethylgallium (TMGa), Phosphine (PH_3), and Arsine (AsH_3) as precursors. The growth temperature is 680 °C and the pressure is 100 mtorr. The structure consists of an InP substrate, a 200 nm thick InGaAs etch stop layer, and the active region (Figure 6.8(a)). On top of the active region, a 12.5 periods DBR of alternating optical $\lambda/4$ Si_3N_4 and SiO_2 layers is deposited (Figure 6.8(b)). In the next step, the whole structure is coated by 50 nm /300 nm Ti/Au respectively and is bonded up side down (using Indium) to a copper heat sink (Figure 6.8(c)). The Indium bonding of the structure to the heat sink allows good heat dissipation, thus improving the functionality of the device. The InP substrate and the InGaAs are then removed selectively by wet chemical etching (Figure 6.8(d) and 6.8(e)). The last technological step is the deposition of a 12 periods DBR with the same dielectric materials as the bottom one (Figure 6.8(f)). The whole technological implementation process is described in detail in appendix B.

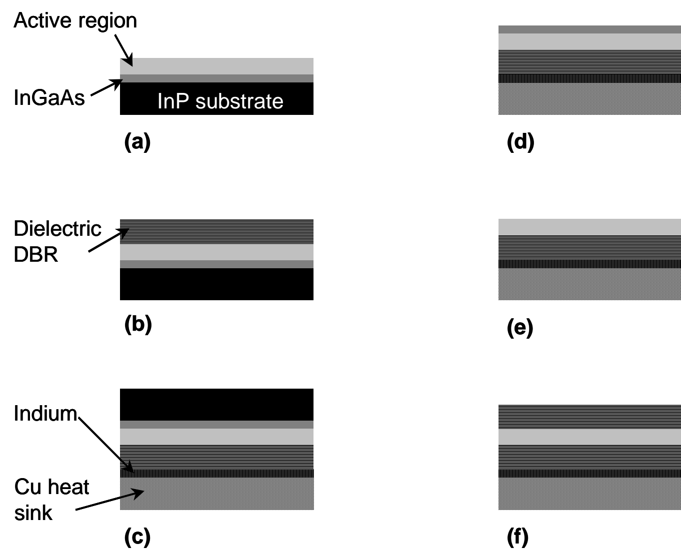

Figure 6.8: *Technological implementation of the non tunable VCSEL: (a) MOVPE growth of the active region and the etch stop layer, (b) PECVD deposition of the bottom dielectric Si_3N_4/SiO_2 DBR, (c) backside Indium bonding of the half VCSEL on a cupper heat sink, (d) bulk micromachining removal of the InP substrate, (e) removing of the etch stop layer, (f) PECVD deposition of the top dielectric Si_3N_4/SiO_2 DBR.*

The active region (Figure 6.9) is formed of three half-wave periods embedded

between two InP spacers. Each single period of the active region contains a strain compensated package of two $Ga_{0.21}In_{0.79}As_{0.75}P_{0.25}$ quantum wells (0.9 % compressive strain) and three $Ga_{0.47}In_{0.53}As_{0.75}P_{0.25}$ barriers. The two quantum wells packages are surrounded by two $Ga_{0.29}In_{0.71}As_{0.63}P_{0.37}$ cladding layers to position them at the antinode of the resonant field. The quantum wells, with a maximum room temperature photoluminescence (PL) at 1545 nm, are populated with photo induced carriers generated by absorption of the pump radiation (λ_{pump}˜980 nm) mainly in the cladding layers. The top and bottom InP spacer layers have an optical thickness of $\lambda/4$ in order to enhance the heat spreading of the active region.

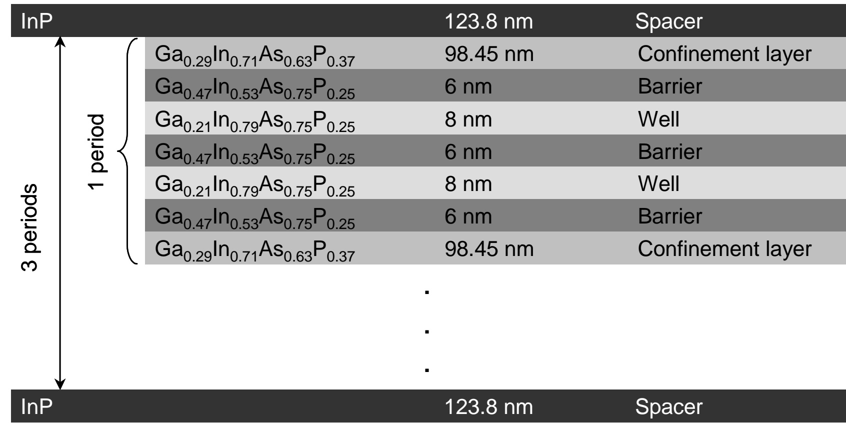

Figure 6.9: *Structure of the active region of the non tunable VCSEL, grown by MOVPE.*

Figure 6.10 shows the optical spectra of the dielectric DBRs, the half cavity resonance (bottom DBR and the active region) as well as the normalized VCSEL output power characteristic. The half cavity resonance peak is positioned at the photoluminescence maximum of the quantum wells. However, there is an offset between the design (1545 nm +5 nm offset) and the lasing wavelength (1556.7 nm). This wavelength shift at the lasing operation is due to several mechanism related either to the design or to the material properties. Concerning the material properties, we have to distinguish between the passive and the active ones. While the passive material exhibits linear dependence on the temperature, the active material shows different linear and non linear effects. Thus by increasing the temperature, the passive material expands, resulting in a cavity length extension. In this case, the resonance characteristic of the cavity shifts to longer wavelengths. Regarding the active material used in this device, two operations related to the wavelength shifting are highly relevant: the continuous and the pulsed optical or electrical pumping. The effect of both electrical pump operations on the wavelength shift is intensively studied in [104]. It has been shown that for a continuous pumping and by increasing the injection current, a blue and a red wavelength shift occur below and upon the threshold, respectively. In this case, the blue shift is due to the strong increase of the carrier density, whereas the red shift is related to the increase of the temperature in the device. For the pulsed operation case, a blue wavelength shift below and upon the threshold with different slopes is observed.

The blue wavelength shift upon the threshold is attributed to the low temperature operation of the device.

In order to ascertain whether the material properties or the design are responsible for the wavelength shift in the VCSEL, the dependence of the emission characteristic on the temperature should be considered.

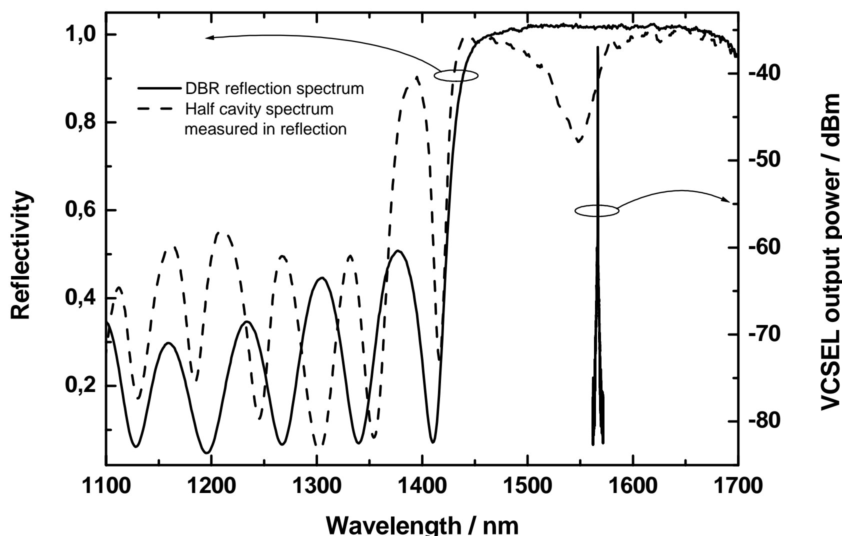

Figure 6.10: *Optical spectra of the dielectric DBRs, the half cavity resonance (Bottom DBR and the active region) as well as the normalized VCSEL output power characteristic.*

The VCSEL is optically pumped by a pulsed 980 nm laser. The pulse repetition interval (PRI) is 70 μs, whereas the pulse width is 4 μs. Figure 6.11 shows the spectral emission of the VCSEL at room temperature. The VCSEL emits at 1556.7 nm and exhibits a FWHM< 0.1 nm and a SMSR of 25 dBm. In the inset of this Figure, the dependence of the VCSEL emission wavelength on the pumping power can be seen. Since the VCSEL is pumped at room temperature, a red shift of the wavelength is expected with increasing pumping power. However, a blue shift with a slop $\Delta\lambda/\Delta p_{pump}$ 0.03 nm / mW is observed. This blue shift is due to the pulsed operation and the heat dissipation concept used for the VCSEL.

Assuming that the VCSEL is operated under low temperatures leading to a blue shift, we can exclude the possibility of passive material expansion. Thus, the red shift between the design and the implementation results is not related to the material properties but rather to design problems occurring due to the PECVD inhomogeneities during the deposition of the DBRs. It seems that parts of the DBRs contribute optically to an expansion of the optical length of the cavity.

Figure 6.12 shows the pump power - output power (P-P) curve of the optically pumped VCSEL. The VCSEL exhibits an output power of 0.5 μW at room temperature and has a threshold pump power of 35 mW. At 6 °C, the pump threshold power is 30 mW and the maximum output power is over 2 μW.

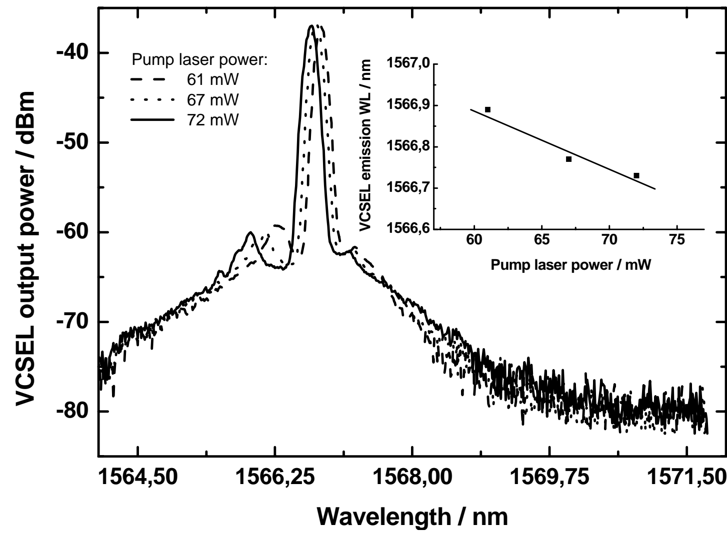

Figure 6.11: *Optical spectrum of the VCSEL during the optical excitation. The blue wavelength shift is due to the pulsed operation.*

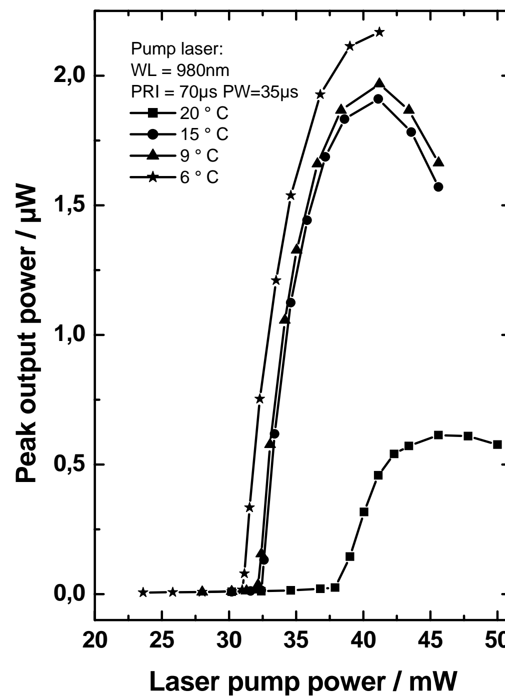

Figure 6.12: *Optical pumping power-output power dependence of the non tunable VCSEL at different operating temperatures.*

6.4 Tunable VCSEL

The tunable VCSEL is implemented by the two chip technological approach [16] and is described in previous work [105]. The two main chips of the device are the lower InP-based part[1] and the bent dielectric top DBR membrane[2]. The two chips were assembled[3] to form the tunable active device. A schematic cross section of the VCSEL is shown in Figure 6.13. The VCSEL consists mainly of an active region and an air-gap cavity embedded between two DBRs of different material systems. The total cavity length L_{cav} is defined by the length of the active region and the length of the air-gap L' between the curved dielectric mirror membrane and the solid part of the cavity.

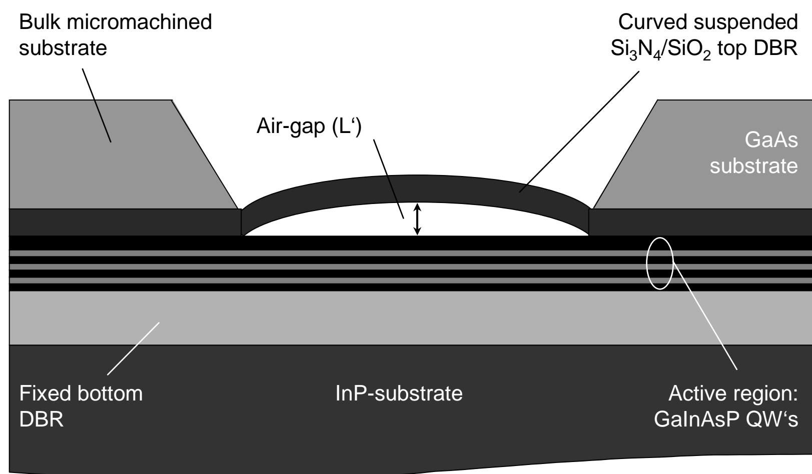

Figure 6.13: *Schematic cross section of the two-chip tunable VCSEL: the lower semiconductor chip comprises the bottom DBR and the active region, the upper part consists of a bent DBR with tailored intrinsic stress.*

The lower chip, comprising the bottom DBR and the active region, is grown monolithically by a low-pressure MOVPE from TMIn, TMGa, PH_3, and AsH_3 precursors. The bottom DBR is designed for a central wavelength (CWL) of 1575 nm and consists of 48 InP/InGaAsP pairs yielding 99.8% nominal reflectivity.

The semiconductor part of the resonator has an optical thickness of 4.5λ and consists of a periodic gain active region optimized for photopumping. The active region is similar to the one described in section 6.3 and is made up of three half-wave periods embedded between two InP layers (Figure 6.14). A strain compensated package of two $Ga_{0.21}In_{0.79}As_{0.75}P_{0.25}$ quantum wells (0.9% compressive strain) and three $Ga_{0.47}In_{0.53}As_{0.75}P_{0.25}$ barriers form one period. Two $Ga_{0.29}In_{0.71}As_{0.63}P_{0.37}$ cladding layers embed the two quantum wells packages. The quantum wells, with a maximum

[1] The lower part is delivered by the Royal Institute of Technology, Kista, Sweden.

[2] The top DBR is implemented by the Institute of Nanostructure Technology and Analytics (INA) at the University of Kassel, Germany.

[3] The assembly is done by the Technical University of Darmstadt (department of optical communications), Germany.

room temperature photoluminescence (PL) at 1545 nm, are populated with photo-induced carriers generated by absorption of the pump radiation ($\lambda_{pump} \sim 980$ nm) mainly in the cladding layers. The top InP layer has an optical thickness of 2.25λ to enhance the heat spreading [7] whereas the lower has a thickness of $0.75\ \lambda$. In this case, the InP spacers are thicker then those of the non tunable VCSEL, since the thermal conductivity of the dielectric DBRs are considered to be better than those of the semiconductor ones. The thermal shift of the gain during lasing is compensated by a tailored spectral detuning of 5 nm −30 nm between the PL and the CWL of the laser (5 nm detuning in the non tuned state and 30 nm in the maximum tuned state).

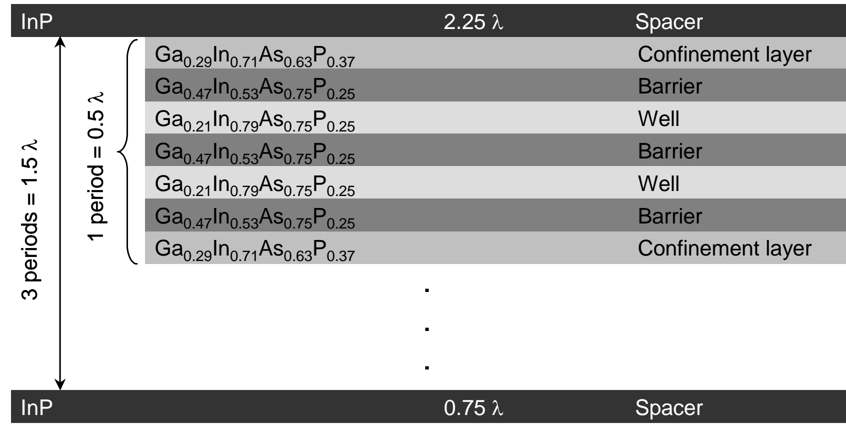

Figure 6.14: *Structure of the active region of the tunable VCSEL, grown by MOVPE.*

The vertical design of the dielectric top DBR is given in Figure 6.15. It consists of 12.5 periods of silicon nitride (Si_3N_4) and silicon dioxide (SiO_2) layers with an optical length of $\lambda/4$ for the designed lasing wavelength (1550 nm). However, the air-gap length L_{cav}, the membrane´s curvature as well as the deflection dynamics of the membrane are adjusted by precisely tailoring the intrinsic stress of the dielectric layers across the DBR. Relying on the PECVD stress investigation in chapter 5 (Figure 5.1), the stress is varied in the vertical direction across the top DBR from −150 MPa tensile (top layer Si_3N_4 (25)) to +400 MPa compressive (bottom layer Si_3N_4 (1)). Figure 5.1 is updated by inserting the values used for the DBR layers in the diagram (Figure 6.16).

After the bulk micromachined backside etching of the GaAs substrate, the membrane bends towards the GaAs substrate. Thus a radius of curvature of 4.5 mm and an air-gap length of 16 μm are obtained (Figure 6.17). According to equation 2.32 and Figure 2.2, this VCSEL is characterized by a half symmetric stable resonator. The circular membrane has a diameter of 300 μm and is fixed by 4 suspensions (600 μm length and 70 μm width) to the substrate.

The injection of a small heating current through a thin metallic layer on the top of the flexible suspensions enables micromechanical actuation of the membrane during the pumping. Thus spectral tuning can be achieved. The metallic layer acts as a heating resistor, converting the dissipated power into thermal heat which slightly increases the length of the suspension beams.

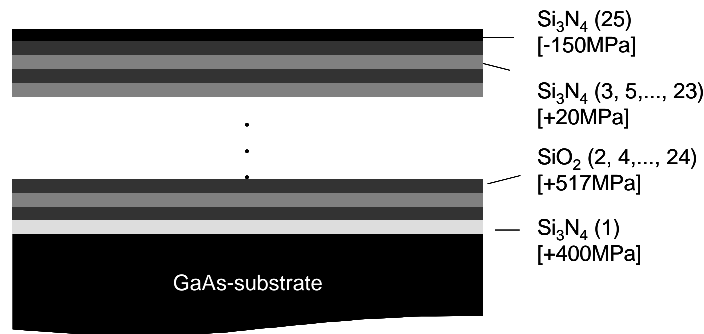

Figure 6.15: *Top dielectric Si_3N_4/SiO_2 DBR (upper chip) with tailored intrinsic stress. The stress of silicon nitride varies in the vertical direction during the deposition.*

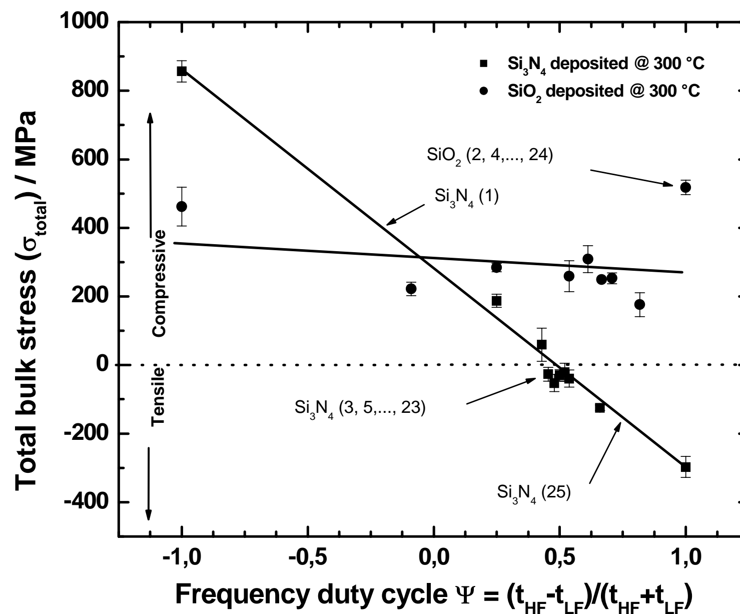

Figure 6.16: *Modified PECVD stress diagram (Figure 5.1) by including the stress values of Si_3N_4 and SiO_2 used along the bent top DBR.*

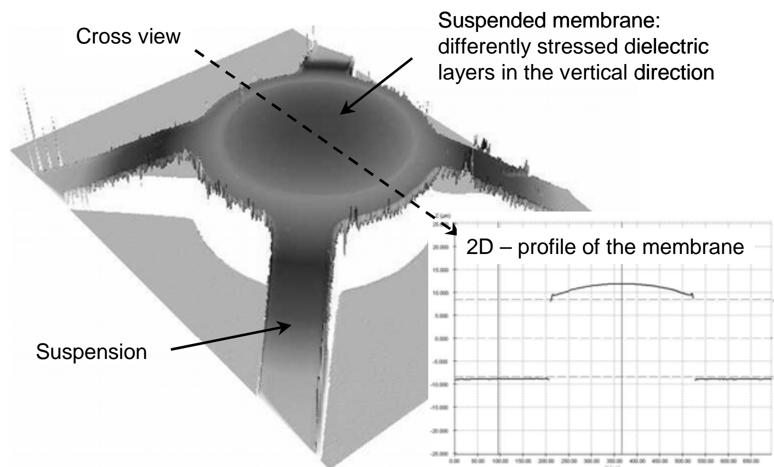

Figure 6.17: *White light interferometer picture of the bent top DBR.*

The optical characterization of the tunable VCSEL is carried out by a fiber-to-fiber transmission measurement set-up. The light of a pump laser (980 nm) is coupled into a lensed fiber, delivering a Gaussian beam with a waist of 20 μm diameter at the position of the active region. The beam waist is well adapted to the ROC and the cavity length according to equation 2.36, thus guaranteeing effective excitation of the fundamental mode and suppression of higher order modes. The output laser light is coupled into a second lensed fiber connected to an optical spectrum analyzer. The pump light is absorbed in the active region and the quaternary material of the bottom DBR so that there is no need to separate the pump light from the VCSEL output.

Figure 6.18 shows the optical spectrum of the tunable VCSEL under optical excitation (980 nm, $30 - 50$ mW) in CW-operation at room temperature. The continuous tuning range is 26 nm. The output power of the VCSEL from the bottom side is $300 - 400\,\mu$W. The device has a free spectral range of 47 nm and a side mode suppression ratio of 57dBm. The laser peak has a line width below the 0.1 nm resolution of the optical spectrum analyzer. The relation between wavelength tuning and heating power due to thermal actuation is exactly linear with a sensitivity of 7 nm/mW.

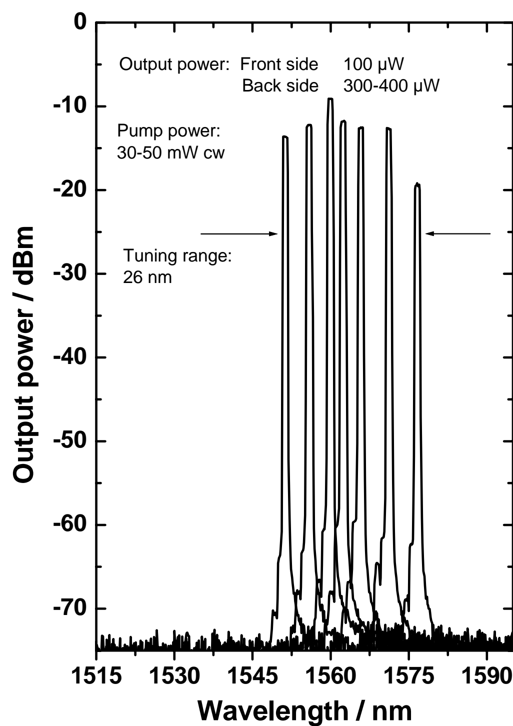

Figure 6.18: *Optical spectrum of the tunable VCSEL. A tuning range of* 26 nm *is achieved.*

6.5 Tunable high end receiver

The two-chip concept described in [16] is used for the implementation of a wavelength selective PIN photodiode. The results of this diodes have been recently published [106–108]. Similar to the device presented in section 6.4, the wavelength selective

diode consists of two main parts. The lower chip comprises the bottom dielectric DBR and the InP based PIN region. The upper part consists of a tailored bent dielectric DBR (Figure 6.19). The bent top DBR comprises 8.5 pairs of $\lambda/4$ alternating Si_3N_4 and SiO_2 layers deposited by the PECVD at 300 °C. After a bulk micromachining etch process of the InP substrate, the top DBR bends due to the tailored intrinsic stress in the layers. The radius of curvature is then 36 mm. The lower chip consists of a mesa structured PIN photodiode with top p-contacts and a 9 periods PECVD dielectric (Si_3N_4 and SiO_2) DBR, which is deposited on the backside of the thinned InP substrate. An antireflection coating is deposited by the PECVD on top of the PIN photodiode in order to avoid the back scattering of the non absorbed light in the absorbing layer. The antireflection coating simultaneously serves as a passivation layer. The electrical contacts are 50 Ω coplanar pads. The tuning occurs by thermomechanical actuation of the top membrane, similar to the device in section 6.4.

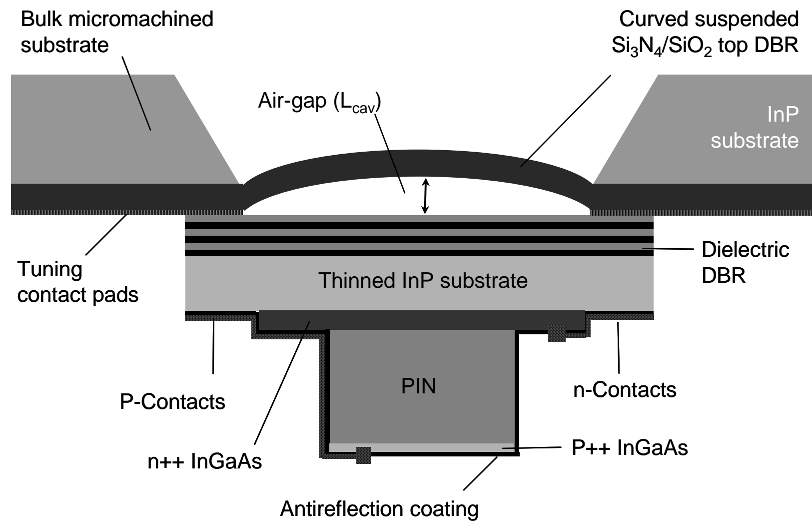

Figure 6.19: *Schematic cross section of the tunable two-chip PIN photodiode.*

Assembling the two chips results in a cavity length of $L_{cav} = 32\,\mu$m. Taking into account the cavity length and the radius of curvature of the top membrane, the beam waist of the incoming light can be calculated according to equation 2.36. A tunable laser, sweeping over the wavelength range of interest in 0.05 nm steps, is used to record the responsivity spectrum of the PIN photodiode. The responsivity of the PIN photodiode is tuned thermally (by actuating the top DBR) over the spectral wavelength range and is shown in Figure 6.20. A detailed consideration of the measurement set-up can be found in [109]. The photodiode shows a FSR of 35 nm, a FWHM below 0.15 nm, and a finesse exceeding 35. However, the tuning range is higher than the FSR. The tuning characteristic between the selected wavelength and the dissipated electrical power in the membrane suspensions is linear and has the value of 0.33 nm / mW. Furthermore, the device shows a peak responsivity (R_{peak}) of 0.30 A / W and an insertion loss of around 7 dB (3.5 dB in the optical domain). The photocurrent crosstalk from neighboring channels is calculated to be −40 dB over the whole tuning range, when assuming

a channel spacing of 0.8 nm. The side modes, which can be seen in Figure 6.20 are due to the mismatch between the incoming excitation light beam (a non Gaussian profile in this case) of the fibre and the resonator geometry.

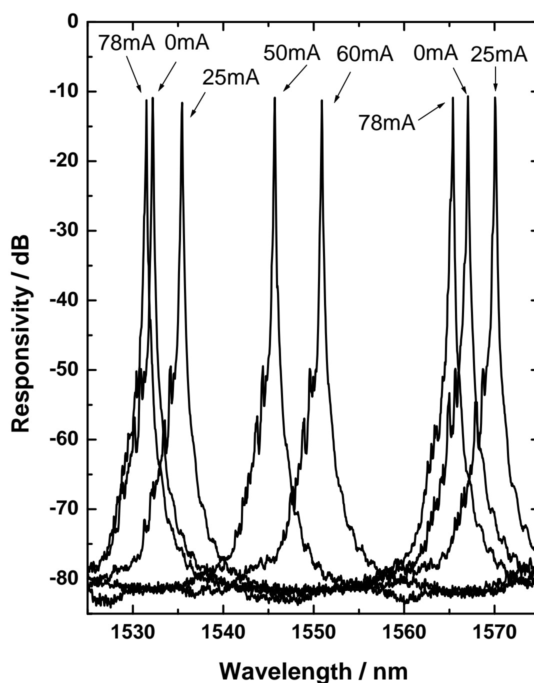

Figure 6.20: *Dependence of the responsivity of the tunable PIN photodiode on the wavelength by several tuning currents.*

Chapter 7

Related applications

7.1 Organic microcavities

7.1.1 PECVD materials and DBRs

Based on the results in chapters 5 and 6, we investigate the possibility of integrating organic light emitting macromolecules in microcavity devices. The goal is to establish a basic technology for novel organic microdevices like VCSELs and photodiodes. The work presented in this section should be considered as a basic investigation yielding promising first results.

In chapter 3, a low temperature PECVD deposition process was developed and presented. In this case, the mechanical properties of the deposited material were an important consideration as we optimized the technological aspect. However, regarding macromolecules in microcavities, the optical characteristics of the deposited material are predominant. For this reason, the absorption (by mean of the extinction coefficient k) of PECVD Si_3N_4 layers deposited at low temperatures (60 °C) is investigated by varying the duty cycle (Ψ). Silicon dioxide is not considered since the hydrogen bonds are, to our best knowledge, the reason for the absorption at a low temperature deposition (see chapter 3). Using spectroscopic ellipsometry, several refractive indeces and extinction coefficient dispersions are measured for different Ψ values. It has been shown that for a duty cycle $\Psi = -1$, the extinction coefficient (proportional to the absorption) of Si_3N_4 exhibits a minimum (Figure 7.2). Unfortunately, at this Ψ value, the refractive index is also at a minimum (Figure 7.1). Furthermore, the stress is highly compressive. However, at this point, the goal is to investigate the optical behavior of the macromolecules in the cavities and therefore, this duty cycle is considered for all the layers Si_3N_4 within this investigation. The effect of the stress on the mechanical properties of the light emitting material is investigated elsewhere [110, 111].

Spectroscopic ellipsometer measurements show difficulties fitting the Psi and Delta data using a Cauchy model in the non absorbing wavelength range, leading to undulations in the extinction coefficient dispersion curves in Figure 7.2. Several effects, such as hydrogen absorption peaks, inhomogeneities the vertical and lateral directions in

the film structures as well as measurement artefacts, may be responsible for these undulations. Hydrogen absorption peaks and measurement artefacts can be excluded as direct undulation source. Furthermore, the amorphous nature of the material implies the absence of birefringence. Thus, the most probable explanation for the deviation of the Cauchy model causing the undulations are vertical inhomogeneities in the refractive index of the films, resulting from the deposition conditions.

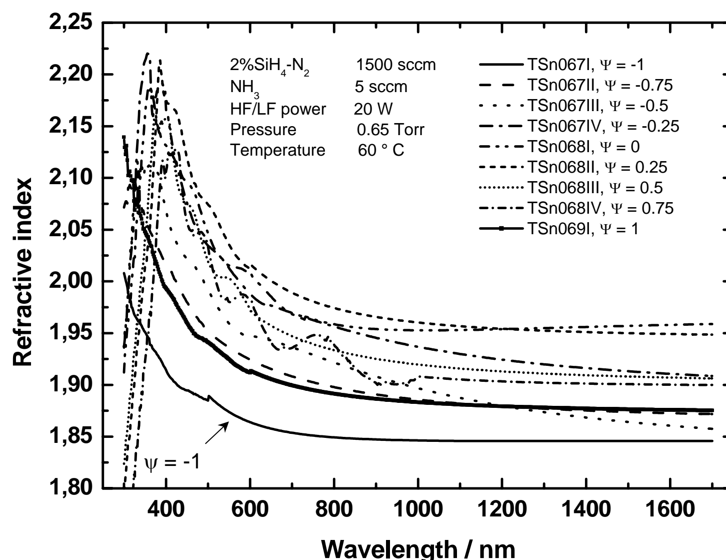

Figure 7.1: *The dependence of the refractive index dispersion of silicon nitride (deposited at 60 °C) on the PECVD duty cycle Ψ. The data have been obtained using a spectroscopic ellipsometer.*

Based on the optical properties of the investigated materials, several Bragg mirrors are implemented for the short wavelength range. Figure 7.3 shows the spectra of two such DBRs deposited at a temperature of 300 °C and designed for the wavelength range 350 nm − 500 nm. The technological implementation process can be found in appendix D. The two DBRs are measured by two different techniques, the spectroscopic ellipsometer (TQ067, incident angle = 15°) and the reflection measurement set-up (TQ069, incident angle = 0°). At this wavelength range, different incident angles result in a spectral shifting and an attenuation of the reflectivity.

The spectral shift is due to different optical paths at different incident angles. On the other hand, the reflection attenuation is due to the high absorption in the layers at this wavelength. Normally, the reflectivity of a DBR implemented by low absorbing material shows nearly no dependence on the measurement incident angle. For the case of a DBR with materials of high absorption coefficient, it can be assumed that the longer the optical path of the light, the higher is the absorption of the light. The dependence of the reflectivity on the incident angle is shown in Figure 7.4. Thus, the reflectivity of different DBRs decreases by increasing the incident angle. The slop of the reflectivity-incident angle curves seems to be the same for all the measured DBRs.

Figure 7.5 shows the spectra of DBRs implemented at high and low temperatures

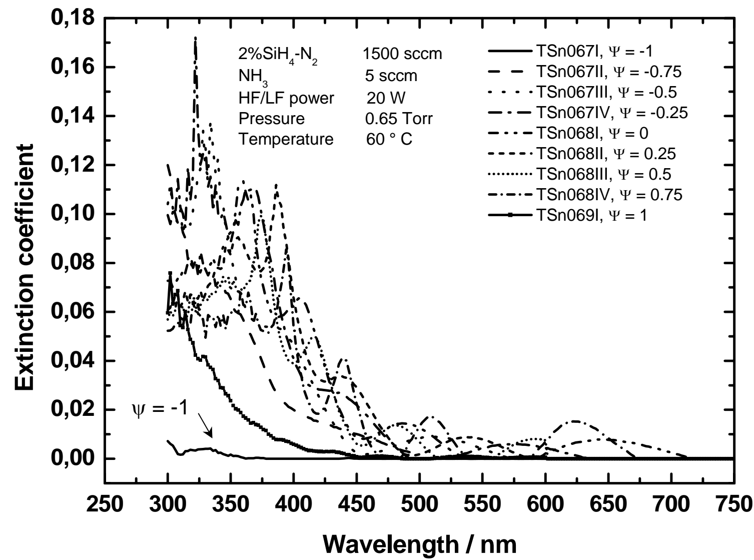

Figure 7.2: *The dependence of the extinction coefficient of silicon nitride (deposited at 60 °C) on the duty cycle Ψ. The data have been obtained using a spectroscopic ellipsometer.*

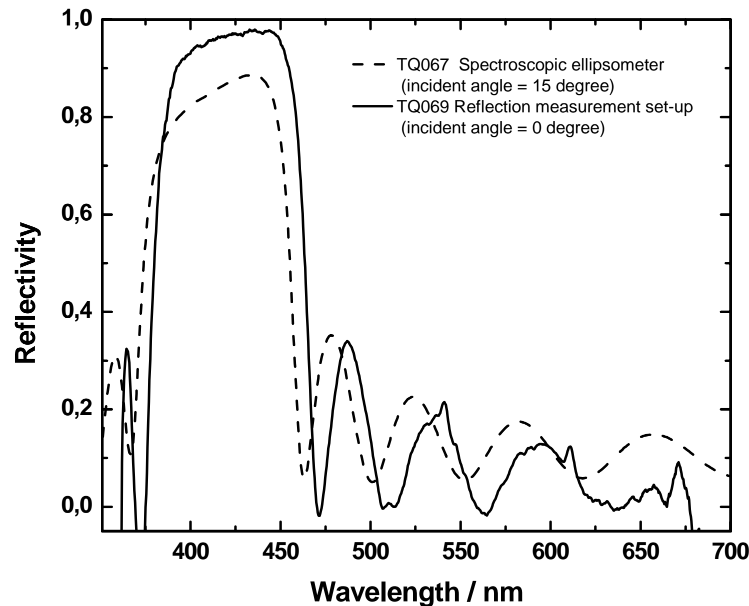

Figure 7.3: *PECVD distributed Bragg reflectors deposited at high temperatures (300 °C) for the short wavelength range.*

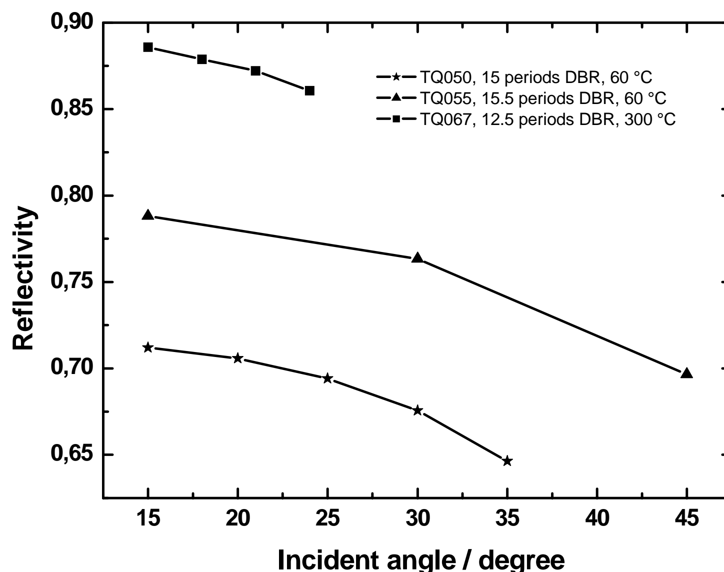

Figure 7.4: *Dependence of the DBR reflectivity at a fixed wavelength on the light incident angle.*

and measured ellipsometrically at an incident angle of 15°. The DBRs TQ067 and Tsn033I are deposited at 300 °C on glass and silicon substrates, respectively. It can be seen that the DBR deposited on the silicon substrate exhibits higher reflectivity. This is due to the deposition temperature coupling since the substrate absorbs the light at this wavelength. At 60 °C, the spectrum of the DBR TQ055 shows high material absorption, which affects the FWHM and the reflectivity of the DBR.

Several rapid thermal annealing processes are incorporated in order to enhance the reflectivity of such DBRs deposited at low temperatures. Even though the reflectivities are noticeably increased, the technological relevance of such step is very weak since the DBRs should be deposited on organic materials.

7.1.2 Organic half cavity

An organic solid state light emitting material should exhibit a high morphological stability, a high fluorescence quantum yield and a low reabsorption. These requirements are met by the class of Spiro linked oligophenyles, of which Spiro-Sexiphenyl (Spiro-6f) has already shown excellent results in amplified spontaneous emission (ASE) experiments performed on spin coated films [112]. The rigid molecular structure of these materials leads to amorphous glasses with high glass transition temperatures above 200 °C. The Spiro concept was extended by adding further oligophenyl chains, linked to the core molecule via additional Spiro junctions [113]. The molecular structure of the newly synthesized 4-Spiro^2 used in this investigation is shown in Figure 7.6.

Four biphenyl and two sexiphenyl units are incorporated in the chemical structure and thus form a stable amorphous glass with a glass transition temperature of 273 °C. The moderate molecular weight of 4-Spiro^2 when compared to polymeric materials

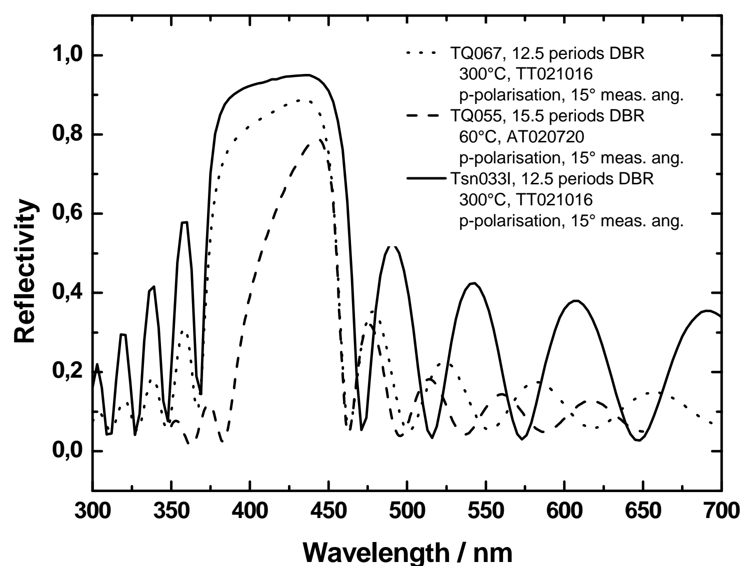

Figure 7.5: *Optical spectra of DBRs implemented by the PECVD at different temperatures and on different substrates.*

4- Spiro²: 2,2',7,7'-Tetra-(9,9'-spirobifluoren-2-yl)-9,9'-spirobifluorene

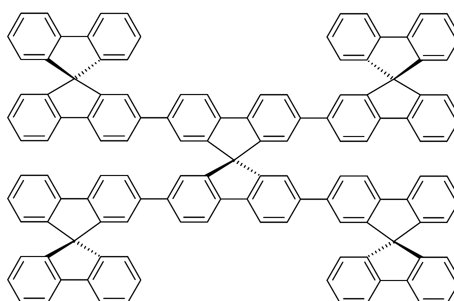

Physical properties		**Optical properties**	
T_g=273°C	T_m=447°C	λ_{abs}=353nm	λ_{em}=429nm

Figure 7.6: *Chemical structure of the light emitting material 4-Spiro^2. The glass and melt temperatures are 273 °C and 447 °C, respectively. The absorption maximum is located at* 353 nm, *whereas the emission occurs at* 429 nm. *With kind permission of the mmCmm group at the University of Kassel, Germany.*

allows the preparation of thin films by vacuum vapor deposition. The optical properties of 4-Spiro^2 are shown in Figure 7.7. The maximum intensity of the spontaneous emission is located at 429 nm, whereas the absorption has a maximum at 353 nm. The spectral shift of the absorption and emission characteristics ensures an optical pumping with a nitrogen laser at 337 nm, far away from the emission wavelength.

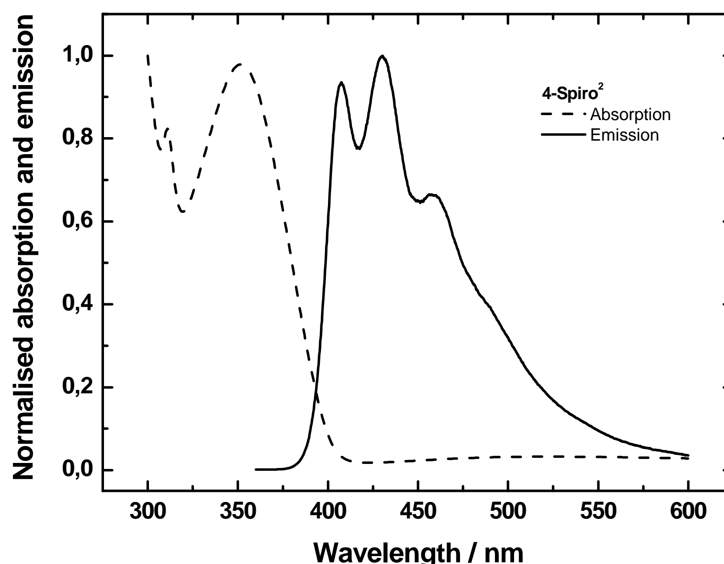

Figure 7.7: *Absorption and emission spectra of 4-Spiro^2. The results in this diagram are courtesy of the mmCmm (with kind permission).*

At a low pumping power density threshold of 3.2 μJ / cm^2, an amplified spontaneous emission (ASE) spectrum was observed [114] for a 106 nm thick film of 4-Spiro^2. Figure 7.8 shows the transition from the normal fluorescence spectrum to ASE for 4-Spiro^2 by varying the pumping power density. At a pumping energy of 10 μJ /cm^2, the ASE peak at 428 nm has a FWHM of 3.2 nm.

Using this material, a half cavity resonance is demonstrated. For this, a 15.5 periods Si_3N_4/SiO_2 DBR is deposited by the PECVD at 60 °C on a glass substrate. The nominal reflectivity of the DBR is approximately 80%. The cavity is implemented by 92.22 nm of 4−Spiro^2 and 56 nm Si_3N_4 serving as a cap layer and prohibiting the light emitting material from oxidizing. Figure 7.9 shows the optical spectra of the lower DBR and the half cavity resonance. However, the half cavity resonance is shifted to a higher wavelengths and matches with a reflectivity of 60% of the lower DBR. Furthermore, the half cavity resonance is located at approximately 450 nm, far away from the emission wavelength of the organic material (4−Spiro^2). In this case a lasing in a cavity is not possible.

It is extremely difficult to design and characterize an organic material in a microcavity since the wavelength used in the measurements set-ups strongly affects the optical and mechanical properties of these materials. Despite that, based on these

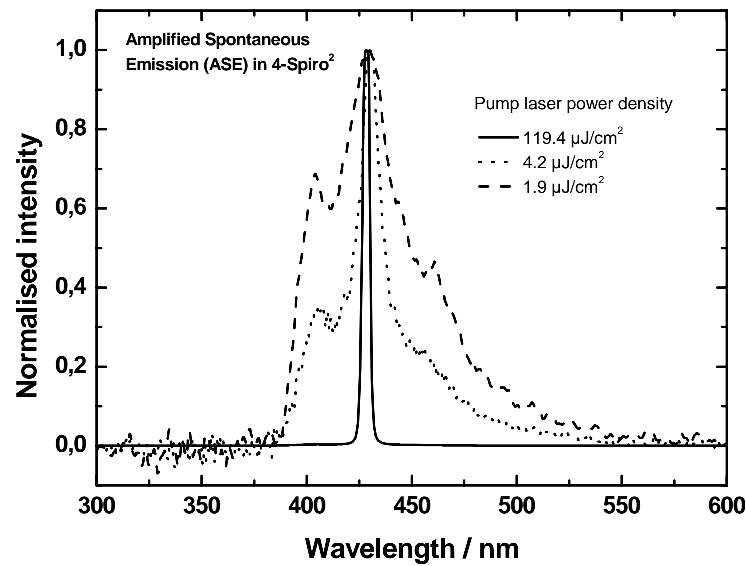

Figure 7.8: *Amplified spontaneous emission spectrum of 4-Spiro*^{2}*. The results in this diagram are courtesy of the mmCmm (with kind permission).*

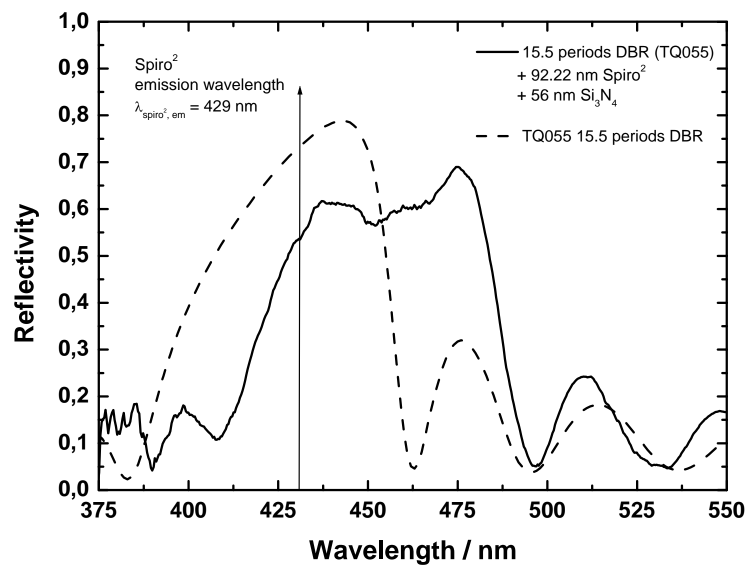

Figure 7.9: *Organic half cavity structure consisting of a 60 °C PECVD DBR (TQ055),* 92.22 nm *4-Spiro*^{2} *and* 56 nm Si_3N_4 *cap layer.*

results, a microcavity is implemented showing an ASE resonance. For this we used an organic light emitting material (Small-Spiro-Octo) similar to the 4-Spiro[2]. The Small-Spiro-Octo (2,2',4,4',7,7'-Hexaphenyl-9,9'-spirobifluoren, $C_{61}H_{40}$) shown in Figure 7.10 exhibits a glass and a melt temperatures of 181 °C and 291 °C, respectively.

Small-Spiro-Octo: 2,2',4,4',7,7'-Hexaphenyl-9,9'-spirobifluorene

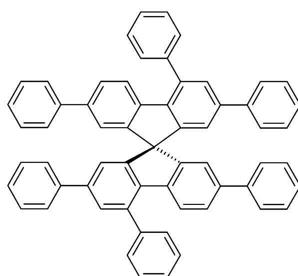

Physical properties T_g=181°C T_m=291°C

Figure 7.10: *Chemical structure of the Small-Spiro-Octo light emitting organic material. With kind permission of the mmCmm.*

The microcavity consists of a bottom PECVD DBR deposited at 120 °C, a cavity of Small-Spiro-Octo and a top DBR. Figure 7.11 shows the optical spectra of the DBRs, the half cavity resonance, the spontaneous emission of the Small-Spiro-Octo and the ASE resonance in the cavity. The half cavity resonance, the second emission maxima (Small-Spiro-Octo) and a reflectivity over 90% of the DBRs, coincide to narrow the emission at 412.5 nm. The FWHM of the ASE resonance is 2.8 nm.

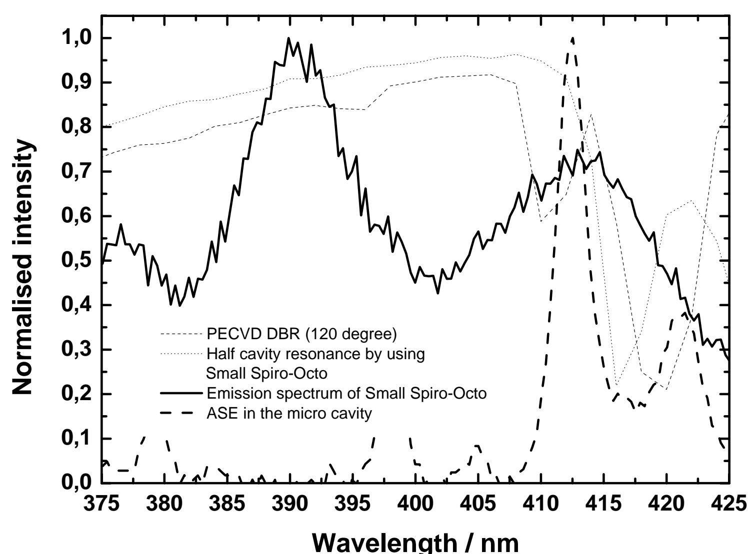

Figure 7.11: *Optical spectrum showing the reflectivity of the DBRs, the half cavity resonance and the ASE in a microcavity. As well as the spontaneous emission of the Small-Spiro-Octo.*

These results demonstrate the possibility of integrating organic light emitting materials in microcavities. This work was not pushed further in the context of this thesis. However, extensive research is in progress as a cooperation between the Institute of Nanostructure Technology and Analytics (INA) and the Institute for Macromolecular Chemistry and Molecular Materials (mmCmm), both at the University of Kassel, Germany.

Chapter 8

Conclusion

The aim of this thesis was to establish a low-cost technology enabling the effective integration of microcavity devices, e.g. into DWDM systems. Both parts, the technological optimization and the microcavity device implementation, are investigated within the scope of this research. For this purpose, a standard parallel plate PECVD reactor was employed. Besides the optical properties like the refractive index and the absorption, the bulk macrostress of silicon nitride and silicon dioxide (deposited at different temperatures) have been extensively studied. The bulk macrostress of silicon nitride has been explicitly controlled, by varying the plasma excitation frequency, in a wide range between +850 MPa (compressive) and −300 MPa (tensile) for 300 °C. The stress of silicon dioxide is quite independent of the frequency. Thus, several DBRs fulfilling specific optical and mechanical requirements were deposited.

Furthermore, a low-cost micromachining technology enabling the fabrication of microdevices by using a standard photoresist as a sacrificial layer has been developed. For this purpose, low temperature (60 °C) silicon nitride and silicon dioxide processes have been optimized. Based on this technology, MEMS structures for detecting the microstress on different neighboring positions along the wafer have been implemented and successfully applied.

Using differently designed air-gap devices (e.g. Fabry-Pérot filters) which are implemented by this low-cost technology, the effect of the stress on these membranes was extensively studied. For the first time, a batch process enabling the low-cost integration of differently shaped membranes (convex, concave and planar) with various radii of curvatures and enclosing different cavity lengths was established. Fabry-Pérot filters covering a spectral range over 190 nm and with several full width at half maxima between 1.5 nm and 64 nm have been demonstrated. The reliability of this novel low-cost technology was demonstrated with an electrothermally tunable Fabry-Pérot filter. The filter consists of an air-gap cavity embedded between a bottom and a bent top dielectric DBRs, respectively. The filter exhibits a tuning range of 15 nm.

These novel technological achievements are used to fabricate microcavity devices with tailored bendings of the top membranes. Thus, an optically pumped tunable VCSEL with an optimized bent suspended top DBR was fabricated for enhancing the

fundamental mode and for suppressing the higher order modes. The desired bending (radius of curvature, shape and cavity length) of the DBR is achieved by a specific selective silicon nitride stress distribution across the vertical direction. The top DBR is actuated electrothermally to achieve a tunability of 26 nm.

Based on the results of the tunable filter and the VCSEL, a tunable PIN photodetector was fabricated by using appropriate bent and non bent dielectric top and bottom DBRs, respectively. The air-gap resonator of the PIN photodiode with a bent membrane is tuned electrothermally and exhibits a responsivity tuning range of more than the 35 nm free spectral range.

Based on these results, the integration of light emitting organic materials in microcavities was investigated. Distributed Bragg reflectors for the short wavelength range (350 nm - 500 nm) have been optimized and deposited. Using two different organic light emitting materials within a microcavity, a half cavity resonance and an amplified spontaneous emission were observed, respectively.

Throughout this work, the crucial stress issue in tunable microcavity devices is adressed and studied. Tailored bent dielectric membranes with different shapes are fabricated. Using this, microcavity devices with organic and inorganic materials are demonstrated. On this basis, a considerable step is done in research towards the commercialisation of low-cost microcavity devices.

A further investigation of this technology, leading for instance to a monolithic integration of a tailored bent dielectric membrane with an electrically pumped VCSEL, is of high relevance for optical communications. Besides this, a main focus in subsequent works could be the integration of active and passive polymers in microcavity devices. Thus, organic microdevices such as VCSELs, photodetectors and filters, with integrated organic driver chips may be an alternative innovative future technology. Furthermore, these organic and inorganic devices could be applied in sensor and medical technologies as well as in the automotive industry.

Bibliography

[1] S.V. Kartalopoulos, *Introduction to DWDM Technology - Data in a Rainbow*, IEEE Press, 2000.

[2] R. Ramaswami and K.N. Sivarajan, *Optical Networks - A Practical Perspective*, Academic Press, second edition, 2002.

[3] Richard Cuningham, "Cooling DWDM market should heat up in 2002," *www.reed-electronics.com, elctronics news*, July 2001.

[4] WinterGreen Reaserch Inc., "DWDM market opportunities, strategies, and forecasts, 2003 to 2008," *www.gii.co.jp, electronics news*, November 2003.

[5] Pioneer Consulting, "Worldwide metro DWDM market to reach nearly $12.6 billion by 2006; slower growth expected through 2002, according to pioneer consulting," *www.pioneerconsulting.com*, March 2002.

[6] E. Mounier, "Optical MEMS and MOEMS for telecommunications," *Proceedings of SPIE*, vol. 4945, 2003.

[7] ElectroniCast Corp., "DWDM component market to reach $34.6 billion by 2009," *www.photonics.com*, May 2001.

[8] Photonics.Com, "$54 billion market forecast for DWDM, reports KMI," *www.pho-tonics.com, electronics news*, February 2001.

[9] S. Irmer, J. Daleiden, V. Rangelov, C. Prott, F. Römer, M. Strassner, A. Tarraf, and H. Hillmer, "Ultralow biased widely continuously tunable fabry-pérot filter," *IEEE Photonics Technology Letters*, vol. 15, no. 3, pp. 434–436, March 2003.

[10] M.C. Larson, B. Pezeshki, and J.S. Harris, "Vertical coupled-cavity microinterferometer on GaAs with deformable-membrane top mirror," *IEEE Photonics Technology Letters*, vol. 7, no. 4, pp. 382–384, April 1995.

[11] D. Hohlfeld and H. Zappe, "An all-dielectric tunable optical filter based on the thermo-optic effect," *IOP, Journal of Optics A: Pure and Applied Optics*, vol. 6, no. 6, pp. 504–511, June 2004.

[12] P. Tayebati, P. Wang, M. Azimi, L. Maflah, and D. Vakhshoori, "Microelectromechanical tunable filter with stable half symmetric cavity," *Electronics Letters*, vol. 34, no. 20, pp. 1967–1968, October 1998.

[13] D. Vakhshoori, P. Tayebati, C.-C. Lu, M. Azimi, P. Wang, J.-H. Zhou, and E. Canoglu, "2mW CW singlemode operation of a tunable1550nm vertical cavity surface emitting laser with 50nm tuning range," *Electronics Letters*, vol. 35, no. 11, pp. 1–2, May 1999.

[14] M. Maute, F. Riemenschneider, G. Boehm, H. Halbritter, M. Ortsiefer, P. Meissner, and M.-C. Amann, "Micro-mechanically tunable long wavelength VCSEL with a burried tunnel junction," *Electronics Letters*, vol. 40, pp. 430–431, April 2004.

[15] M. Ortsiefer, R. Shau, G. Boehm, F. Koehler, and M.-C. Amann, "Low-threshold index-guided 1.5 μm long-wavelength vertical-cavity surface-emitting laser with high efficiency," *Applied Physics Letters*, vol. 76, no. 16, pp. 2179–2181, April 2000.

[16] F. Riemenschneider, M. Aziz, H. Halbritter, I. Sagnes, and P. Meissner, "Low-cost electrothermally tunable optical microcavities based on GaAs," *IEEE Photonics Technology Letters*, vol. 14, no. 11, pp. 1566–1568, November 2002.

[17] F. Riemenschneider, M. Maute, H. Halbritter, G. Boehm, M.-C. Amann, and P. Meissner, "Continuously tunable long-wavelength MEMS-VCSEL with over 40-nm tuning range," *IEEE Photonics Technology Letters*, vol. 16, no. 10, pp. 2212–2214, October 2004.

[18] H.A. Macleod, *Thin-Films Optical Filters*, Institute of Physics IOP, third edition, 2001.

[19] T.E. Sale, *Vertical Cavity Surface Emitting Lasers*, Research Studies Press LTD., 1995.

[20] H. Li and K. Iga, *Vertical-Cavity Surface-Emitting Laser Devices*, Spinger, 2002.

[21] M.-C. Amann and J. Buus, *Tunable Laser Diodes*, Artech House, Inc., 1998.

[22] C.K. Madsen and J.H. Zhao, *Optical Filter Design and Analysis- A Signal Processing Approach*, Wiley-Interscience, 1999.

[23] H. Hillmer, J. Daleiden, C. Prott, F. Römer, S. Irmer, V. Rangelov, A. Tarraf, S. Schüler, and M. Strassner, "Potential for micromachined actuation of ultra-wide continuously tunable optical devices," *Applied Physics B*, vol. 75, pp. 3–13, 2002.

[24] S. Irmer, J. Daleiden, V. Rangelov, C. Prott, F. Römer, M. Strassner, A. Tarraf, and H. Hillmer, "Continuously tunable InP based multiple air-gap MOEMS filters with ultra wide tuning range," *SPIE Proceedings*, vol. 4945, pp. 21–29, 2002.

[25] J. Peerlings, *Mikromechanisch Abstimmbare Zweichip-Fabry-Pérot-Filter und -Empfänger Für Wellenlängenmultiplex-Systeme*, Ph.D. thesis, Technical University of Darmstadt, 1999.

[26] M. Aziz, *Mikromechanisch Abstimmbare WDM-Filter mit Halbsymmetrischem Resonator und Ihre Systemintegration*, Ph.D. thesis, Technical University of Darmstadt, 2002.

[27] H. Soda, K. Iga, C. Kitahara, and Y. Suematsu, "GaInAs/InP surface emitting injection lasers," *Japanese Journal of Applied Physics*, vol. 18, no. 12, pp. 2329–2330, 1979.

[28] G.S. Li, W. Yuen, and C.J. Chang-Hasnain, "Wide and continuously tunable (30 nm) detector with uniform characteristics over tuning range," *Electronics Letters*, vol. 33, pp. 1122–1123, 1997.

[29] F. Sugihwo, C.C. Lin, L.A. Eyres, M.M. Feyer, and J.S. Harris, "Broadly-tunable narrow-linewidth micromachined Laser/Photodetector and phototransistor," *Technical Digest of the Electron Devices Meeting (IEDM)*, pp. 665–668, December 1998.

[30] D. Zhou, M. Garrigues, J.L. Leclercq, J. Peng, and P. Viktorovitch, "A phase-matching and pseudoresonance-enhanced design for tunable micromachined photodetectors," *IEEE Photonics Technology Letters*, vol. 15, no. 10, pp. 1443–1445, October 2003.

[31] M.S. Wu, E.C. Vail, G.S. Yuen, and C.J. Chang-Hasnain, "Widely and continuously tunable micromachined resonant cavity detector with wavelength tracking," *IEEE Photonics Technology Letters*, vol. 8, no. 1, pp. 98–100, January 1996.

[32] F.J. Duarte, *Tunable Lasers Handbook*, Optics and Photonics, 1995.

[33] Y. Bäcklung, "Micromechanics in optical microsystems-with focus on telecom systems," *IOP, Journal of Micromechanics and Microengineering*, vol. 7, no. 3, pp. 93–98, September 1997.

[34] J.A. Walker, "The future of MEMS in telecommunications networks," *IOP, Journal of Micromechanics and Microengineering*, vol. 10, no. 3, pp. R1–R7, September 2000.

[35] C. Prott, F. Römer, E. Ataro, J. Daleiden, S. Irmer, A. Tarraf, and H. Hillmer, "Modeling of ultrawidely tunable vertical cavity air-gap filters and VCSELs," *IEEE Journal of Selected Topics in Quantum Electronics*, vol. 9, no. 3, pp. 918–928, May/June 2003.

[36] H. Guckel, D. Burnst, C. Rutigliano, E. Lovell, and B. Choi, "Diagnostic microstructures for the measurement of intrinsic strain in thin films," *IOP, Journal of Micromechanics and Microengineering*, vol. 2, no. 2, pp. 86–95, June 1992.

[37] N. Chitica, M. Strassner, and J. Daleiden, "Quantitative evaluation of growth-induced residual stress in InP epitaxial micromechanical structures," *Applied Physics Letters*, vol. 77, no. 2, pp. 202–204, July 2000.

[38] L. Elbrecht, U. Storm, R. Catanescu, and J. Binder, "Comparison of stress measurement techniques in surface micromachining," *IOP, Journal of Micromechanics and Microengineering*, vol. 7, no. 3, pp. 151–154, September 1997.

[39] M.T.-K. Hou, K.-M. Liao, H.-Z. Yeh, B.-W Cheng, P.-Y. Hong, and R. Chen, "Fabrication of micromachined focusing mirrors with seamless reflective surface," *Proceedings of SPIE*, vol. 4983, pp. 359–366, 2003.

[40] K. Cao, W. Liu, and J.J. Talghader, "Curvature compensation in micromirrors with high-reflectivity optical coatings," *Journal of Microelectromechanical Systems*, vol. 10, no. 3, pp. 409–417, September 2001.

[41] F.R. Gass, D.J. Dagel, D.P. Adams, G.D. Grossetete, O.B. Spahn, S.A. Kemme, S.S. Mani, and K.J. Malloy, "Stress and curvature in MEMS mirrors," *Proceedings of SPIE*, vol. 4983, pp. 87–93, 2003.

[42] J.J. Talghader, "Shape control and heat transfer in optical MEMS," *IEEE/LEOS Newsletter*, vol. 16, pp. 3–8, August 2002.

[43] W. Becker and D. Gross, *Mechanik Elastischer Körper und Strukturen*, Springer, 2002.

[44] H. Göldner and F. Holzweißig, *Leitfaden der Technischen Mechanik*, Dr. Dietrich Steinkopff Verlag-Darmstadt, fifth edition, 1976.

[45] F. Ziegler, *Mechanics of Solids and Fluids*, Springer-Verlag, second edition, 1995.

[46] J. Wittenburg and E. Pestel, *Festigkeitslehre, Ein Lehr- und Arbeitsbuch*, Springer, third edition, 2001.

[47] A. Degen, *Investigation of Stress in Silicon Membranes*, Ph.D. thesis, University of Kassel, Germany, 2001.

[48] D.L. Smith, A.S. Alimonda, and F.J. Von Preissig, "Mechanism of SiN_xH_y deposition from $N_2 - SiH_4$ plasma," *Journal of Vacuum Science Technology B*, vol. 8, no. 3, pp. 551–557, May/June 1990.

[49] H. Windischmann, "An intrinsic stress scaling law for polycrystalline thin films prepared by ion beam sputtering," *Journal of Applied Physics*, vol. 62, no. 5, pp. 1800–1807, September 1987.

[50] C.A. Davis, "A simple model for the formation of compressive stress in thin films by ion bombardement," *Thin Solid Films*, vol. 226, pp. 30–34, 1993.

[51] C.L.G. Alzar, "Mechanical stress reduction in PECVD a-Si:H thin films," *Materials Science and Engineering B*, vol. 65, pp. 123–126, 1999.

[52] A. Tarraf, J. Daleiden, D. Prasai, and H. Hillmer, "Stress investigation of PECVD dielectric layers for advanced optical MEMS," *IOP, Journal of Micromechanics and Microengineering*, vol. 14, no. 3, pp. 317–323, March 2003.

[53] K.H. Yang, "An optical imaging methode for wafer warpage measurements," *Journal of Electrochemical Society, Solid-State Science and Technology*, vol. 132, no. 5, pp. 1214–1218, May 1985.

[54] A. Degen, J. Voigt, M. Kratzenberg, F. Shi, J. Butschke, H. Löscher, R. Kaesmaier, A. Ehrmann, and I.W. Rangelow, "Stress engineering of SOI silicon stencil masks by boron doping concentration," *SPIE Proceedings*, vol. 3997, 2000.

[55] F. Ericson, S. Greek, J. Söderkvist, and J.-A. Schweitz, "High-sensitivity surface micromachined structures for internal stress and stress gradient evaluation," *IOP, Journal of Micromechanics and Microengineering*, vol. 7, no. 1, pp. 30–36, March 1997.

[56] L. Nicu, P. Temple-Boyer, C. Bergaud, E. Scheid, and A. Martinez, "Energy study of buckled micromachined beams for thin-film stress measurements applied to SiO2," *IOP, Journal of Micromechanics and Microengineering*, vol. 9, no. 4, pp. 414–421, December 1999.

[57] W. Fang, C.-H. Lee, and H.-H. Hu, "On the bucling behavior of micromachined beams," *IOP, Journal of Micromechanics and Microengineering*, vol. 9, no. 3, pp. 236–244, September 1999.

[58] C. Tsou and W. Fang, "The effect of residual stresses on the deformation of semi-circular micromachined beams," *IOP, Journal of Micromechanics and Microengineering*, vol. 10, no. 1, pp. 34–41, March 2000.

[59] Y.-H. Min and Y.-K. Kim, "In situ measurement of residual stress in micromachined thin films using a specimen with composite-layered cantilevers," *IOP, Journal of Micromechanics and Microengineering*, vol. 10, no. 3, pp. 314–321, September 2000.

[60] E.I. Bromley, J.N. Randall, D.C. Flanders, and R.W. Mountain, "A technique for the determination of stress in thin films," *Journal of Vacuum Science Technology B*, vol. 1, no. 4, pp. 1364–1366, December 1983.

[61] W. Fang and J.A. Wickert, "Determining mean and gradient residual stresses in thin films using micromachined cantilevers," *IOP, Journal of Micromechanics and Microengineering*, vol. 6, no. 3, pp. 301–309, September 1996.

[62] C.H. Pan, "A simple method for determining linear thermal expansion coefficients of thin films," *IOP, Journal of Micromechanics and Microengineering*, vol. 12, no. 5, pp. 548–555, September 2002.

[63] C.-L. Dai, "In situ electrostatic microactuators for measuring the Youngs modulus of CMOS thin films," *IOP, Journal of Micromechanics and Microengineering*, vol. 13, no. 5, pp. 563–567, September 2003.

[64] W. Fang, "Determination of the elastic modulus of thin film materials using self-deformed micromachined cantilevers," *IOP, Journal of Micromechanics and Microengineering*, vol. 9, no. 3, pp. 230–235, September 1999.

[65] M.W. Donhoff, "A measurement of Youngs modulus and residual stress in MEMS bridges using a surface profiler," *IOP, Journal of Micromechanics and Microengineering*, vol. 13, no. 5, pp. 686–692, September 2003.

[66] S. Greek, F. Ericson, S. Johanson, M. Fürtsch, and A. Rump, "Mechanical characterization of thick polysilicon films: Youngs modulus and fracture strength evaluated with microstructures," *IOP, Journal of Micromechanics and Microengineering*, vol. 9, no. 3, pp. 245–251, September 1999.

[67] F.H.P.M. Habraken and A.E.T. Kuiper, "Silicon nitride and oxynitride films," *Materials Science and Engineering*, vol. R12, no. 3, pp. 123–170, July 1994.

[68] R. E. Williams, *Modern GaAs Processing Methods*, Artech House Inc., second edition, 1990.

[69] T. Yoshimi, H. Sakai, and K. Tanaka, "Analysis of hydrogen content in plasma silicon nitride film," *Journal of the Electrochemical Society: Solid-State Science and Technology*, vol. 127, pp. 1853–1854, August 1980.

[70] G.M. Samuelson and K.M. Mar, "The correlations between physical and electrical properties of PECVD SiN with their composition ratios," *Journal of the Electrochemical Society: Solid-State Science and Technology*, vol. 129, no. 8, pp. 1773–1778, August 1982.

[71] W.A.P. Classen, W.G.J.N. Valkenburg, F.H.P.M. Habraken, and Y. Tamminga, "Characterization of plasma silicon nitride layers," *Journal of the Electrochemical Society: Solid-State Science and Technology*, vol. 130, no. 12, pp. 2419–2423, December 1983.

[72] W.A.P. Claassen, W.G.J.N. Valkenburg, M.F.C. Willemsen, and W.M.V.D. Wijgert, "Influence of deposition temperature, gas pressure, gas phase composition, and RF frequency on composition and mechanical stress of plasma silicon nitride layers," *Journal of the Electrochemical Society: Solid-State Science and Technology*, vol. 132, no. 4, pp. 893–898, April 1985.

[73] E. Bustarret, M. Bensouda, M.C. Habrad, J.C. Bruyère, S. Poulin, and S.C. Gujrathi, "Configurational statistics in $a-Si_xN_yH_z$ alloys: A quantitative bonding analysis," *Physical Review B*, vol. 38, no. 12, pp. 8171–8182, October 1988.

[74] T.J. Cotler and J. Chapple-Sokol, "High quality plasma-enhanced chemical vapour deposition silicon nitride films," *Journal of the Electrochemical Society*, vol. 140, no. 7, pp. 2071–2075, July 1993.

[75] W.A. Lanford and M.J. Rand, "The hydrogen content of plasma-deposited silicon nitride," *Journal of Applied Physics*, vol. 49, no. 4, pp. 2473–2477, April 1978.

[76] J.A. Taylor, "The mechanical properties and microstructure of plasma enhanced chemical vapour deposited silicon nitride films," *Journal of Vacuum Science and Technology A*, vol. 9, no. 4, pp. 2464–2468, August 1991.

[77] CVD Inc., "Fundamentals of chemical vapor deposition: Silicon dioxide, properties and applications," *Electronic Publishing, TimeDomain CVD Inc.*

[78] P.J. French and P.M. Sarro, "Surface versus bulk micromachining: The contest for suitable applications," *IOP, Journal of Micromechanics and Microengineering*, vol. 8, no. 2, pp. 45–53, June 1998.

[79] M. Hoffmann and E. Voges, "Bulk silicon micromachining for MEMS in optical communication systems," *IOP, Journal of Micromechanics and Microengineering*, vol. 12, no. 4, pp. 349–360, July 2002.

[80] C. Linder, L. Paratte, M.-A. Grétillat, V.P. Jaecklin, and N.F. de Rooij, "Surface micromachining," *IOP, Journal of Micromechanics and Microengineering*, vol. 2, no. 3, pp. 122–132, September 1992.

[81] K. Hjort, "Sacrificial etching of III-V compounds for micromechanical devices," *IOP, Journal of Micromechanics and Microengineering*, vol. 6, no. 4, pp. 370–375, December 1996.

[82] J.-L. Leclercq, M. Garrigues, X. Letartre, C. Seassal, and P. Viktorovitch, "InP-based MOEMS and related topics," *IOP, Journal of Micromechanics and Microengineering*, vol. 10, no. 2, pp. 287–292, June 2000.

[83] C. Seassal, J.L. Leclercq, and P. Viktorovitch, "Fabrication of InP-based freestanding microstructures by surface micromachining," *IOP, Journal of Micromechanics and Microengineering*, vol. 6, no. 2, pp. 261–265, June 1996.

[84] Z. Cui and R.A. Lawes, "A new sacrificial layer process for the fabrication of micromechanical systems," *IOP, Journal of Micromechanics and Microengineering*, vol. 7, no. 3, pp. 128–130, September 1997.

[85] M. Bartek and R.F. Wolffenbuttel, "Dry release of metal structures in oxygen plasma: Process characterization and optimization," *IOP, Journal of Micromechanics and Microengineering*, vol. 8, no. 2, pp. 91–94, June 1998.

[86] K.J. Winchester and J.M. Dell, "Tunable fabry-pérot cavities fabricated from PECVD silicon nitride employing zinc sulphide as the sacrificial layer," *IOP,*

Journal of Micromechanics and Microengineering, vol. 11, no. 5, pp. 589–594, September 2001.

[87] J. Bühler, F.-P. Steiner, and H. Baltes, "Silicon dioxide sacrificial layer etching in surface micromachining," *IOP, Journal of Micromechanics and Microengineering*, vol. 7, no. 1, pp. R1–R13, March 1997.

[88] T.E. Bell, P.T.J. Gennissen, D. DeMunter, and M. Kuhl, "Porous silicon as a sacrificial material," *IOP, Journal of Micromechanics and Microengineering*, vol. 6, no. 4, pp. 361–369, December 1996.

[89] S. Deladi, M.J. de Boer, G. Krijnen, D. Rosén, and M.C. Elwenspoek, "Innovative process development for a new micro-tribosensor using surface micromachining," *IOP, Journal of Micromechanics and Microengineering*, vol. 13, no. 4, pp. S17–S22, July 2003.

[90] Z. Li, G. Zhang, W. Wang, Y. Hao, T. Li, and G. Wu, "Study on the application of silicide in surface micromachining," *IOP, Journal of Micromechanics and Microengineering*, vol. 12, no. 2, pp. 162–167, March 2002.

[91] M.A. Benitez, J.A. Plaza, S.Q. Sheng, and J. Esteve, "A new process for releasing micromechanical structures in surface micromachining," *IOP, Journal of Micromechanics and Microengineering*, vol. 6, no. 1, pp. 36–39, March 1996.

[92] D. Westberg, O. Paul, G. Andersson, and H. Baltes, "Surface micromachining by sacrificial aluminium etching," *IOP, Journal of Micromechanics and Microengineering*, vol. 6, no. 4, pp. 376–384, December 1996.

[93] Z. Xiao, Y. Hao, T. Li, G. Zhang, S. Liu, and G. Wu, "A new release process for polysilicon surface micromachining using sacrificial polysilicon anchor and photolithography after sacrificial etching," *IOP, Journal of Micromechanics and Microengineering*, vol. 9, no. 4, pp. 300–304, December 1999.

[94] A. Bagolini, L. Pakula, T.L.M. Scholtes, H.T.M. Pham, P.J. French, and P.M. Sarro, "Polyimide sacrificial layer and novel materials for post-processing surface micromachining," *IOP, Journal of Micromechanics and Microengineering*, vol. 12, no. 4, pp. 385–389, July 2002.

[95] N. Tas, T. Sonnenberg, H. Jansen, R. Legtenberg, and M. Elwenspoek, "Stiction in surface micromachining," *IOP, Journal of Micromechanics and Microengineering*, vol. 6, no. 4, pp. 385–397, December 1996.

[96] T. Takagi, K. Takechi, Y. Watabe, and S. Nishida, "High rate deposition of a-Si:H and $a-SiN_x:H$ by VHF PECVD," *Vacuum*, vol. 51, no. 4, pp. 751–755, 1998.

[97] R. Etemadi, C. Godet, M. Kildemo, J.E. Bourée, R. Brenot, and B. Drévillon, "Dual-mode radio frequency/microwave plasma deposition of amorphous silicon oxide thin films," *Journal of non-Crystalline Solids*, vol. 187, pp. 70–74, 1995.

[98] D.W. Hess, "Plasma-enhanced CVD: Oxides, nitrides, transition metals, and transition metal silicides," *Journal of Vacuum Science Technology A*, vol. 2, no. 2, pp. 244–252, April/June 1984.

[99] M. Aziz, J. Pfeiffer, and P. Meissner, "Modal behaviour of passive, stable microcavities," *Physica Status Solidi A*, vol. 188, no. 9, pp. 79–82, 2001.

[100] S. Schüler, "Technologische Realisierung optischer Filter basierend auf Multiairgapstrukturen in Indium-Phosphid," *Diplomarbeit an der Universität Kassel*, 2001.

[101] P.-U. Archaow, "Optimization and fabrication of tunable airgap InP based filters," *Diplomarbeit an der Universität Kassel*, April 2003.

[102] F. Römer, "Charakterisierung und simulation optischer eigenschaften von mikromechanisch abstimmbaren filterbauelementen," *PhD thesis, Universität Kassel, Germany*, 2005.

[103] A. Tarraf, J. Daleiden, F. Römer, C. Prott, S. Irmer, E. Ataro, and H. Hillmer, "A novel low-cost tunable dielectric air-gap filter," *IEEE/LEOS proceedings of the international Conference on Optical MEMS*, pp. 175–176, 2002.

[104] H. Hillmer, S. Hansmann, H. Bukhard, H. Walter, A. Krost, and D. Bimberg, "Study of wavelength shift in InGaAs/InAlGaAs QW DFB lasers based on laser parameters from a comparison of experiment and theory," *IEEE Journal of Quantum Electronics*, vol. 30, no. 10, pp. 2251–2261, October 1994.

[105] A. Tarraf, F. Riemenschneider, M. Strassner, J. Daleiden, S. Irmer, H. Halbritter, H. Hillmer, and P. Meissner, "Continuously tunable 1.55 μm VCSEL implemented by precisely curved dielectric top DBR involving tailored stress," *IEEE Photonics Technology Letters*, vol. 16, no. 3, pp. 720–722, March 2004.

[106] H. Halbritter, F. Riemenschneider, S. Syguda, C. Dhanavantri, M. Strassner, A. Tarraf, B.R. Singh, I. Sagnes, and P. Meissner, "Tunable and wavelength selective pin photodiode," *Electronics Letters*, vol. 40, no. 6, pp. 388–390, 2004.

[107] H. Halbritter, C. Dhanavantri, M. Strassner, A. Tarraf, M. Aziz, F. Riemenschneider, S. Syguda, B.R. Singh, I. Sagnes, and P. Meissner, "Tunable and wavelength selective pin diodes," *SPIE proceedings*, vol. 5277, pp. 129–127, december 2003.

[108] H. Halbritter, F. Riemenschneider, B. Kögel, A. Tarraf, M. Strassner, S. Irmer, H. Hillmer, I. Sagnes, and P. Meissner, "MEMS-tunable and wavelength selective receiver front end," *Proceedings of the 18th international IEEE conference on micro-electro-mechanical systems (MEMS)*, pp. 68–71, 2005.

[109] H. Halbritter, "Entwicklung und Charakterisierung mikromechanisch abstimmbarer Komponenten für optische Kommunikationssysteme," *PhD thesis, Technische Universität Darmstadt, Germany*, 2005.

[110] M. Müller-Wiegand, G. Georgiev, E. Oesterschulze, T. Fuhrmann, and J. Salbeck, "Spinodal patterning in organic-inorganic hybrid laser systems," *Applied Physics Letters*, vol. 81, no. 26, pp. 4940, 2002.

[111] M. Müller-Wiegand, "Spontane Strukturierung in Mehrschichtsystemen unter Verwendung molekularer Gläser," *PhD Thesis, University of Kassel*, October 2003.

[112] N. Johansson, J. Salbeck, J. Bauer, F. Weissoertel, P. Broems, A. Andersson, and W.R. Salaneck, "Solid-state amplified spontaneous emission in some spiro-type molecules: A new concept for the design of solid state lasing molecules," *Advanced Materials*, vol. 10, pp. 1136, 1998.

[113] K.H. Weinfurtner, F. Weissörtel, G. Harmgarth, and J. Salbeck, "Novel amorphous molecular materials for organic light-emitting devices," *Proceedings of SPIE*, vol. 3476, pp. 40–48, 1998.

[114] J. Salbeck, M. Schörner, and T. Fuhrmann, "Optical amplification in spiro-type molecular glasses," *Thin solid films*, vol. 417, pp. 20–25, 2002.

[115] J. Bryzek, K. Petersen, and W. McCulley, "Micromachines on the march," *IEEE Spectrum*, pp. 20–31, May 1999.

[116] R. Bischoffberger, M. Cucinelli, and G. Staufert, "New ways to make micromachines," *Vacuum Solutions*, pp. 15–18, 1997.

[117] E.C. Vail, M.S. Wu, G.S. Li, L. Eng, and C.J. Chang-Hasnain, "GaAs micromachined widely tunable fabry-pérot filters," *Electronics Letters*, vol. 31, no. 3, pp. 228–229, February 1995.

[118] A.T.T.D. Tran, Y.H. Lo, Z.H. Zhu, D. Haronian, and E. Mozdy, "Surface micromachined fabry-pérot tunable filter," *IEEE Photonics Technology Letters*, vol. 8, no. 3, pp. 393–395, March 1996.

[119] J. Peerlings, A. Dehe, A. Vogt, M. Tilsch, C. Hebeler, F. Langenhan, P. Meissner, and H.L. Hartnagel, "Long resonator micromachined tunable GaAs-AlAs fabry-pérot filter," *IEEE Photonics Technology Letters*, vol. 9, no. 9, pp. 1235–1237, September 1997.

[120] P. Tayebati, P.D. Wang, D.Vakhshoori, and R.N. Sacks, "Widely tunable fabry-pérot filter using $Ga(Al)As$-AlO_x deformable mirrors," *IEEE Photonics Technology Letters*, vol. 10, no. 3, pp. 394–396, March 1998.

[121] A. Spisser, R. Ledantec, C. Seassal, J.L. Leclerq, T. Benyattou, D. Rondi, R. Blondeau, G. Guillot, and P. Viktorovitch, "Highly selective and widely tunable 1.55-μm InP/Air-gap micromachined fabry-pérot filter for optical communications," *IEEE Photonics Technology Letters*, vol. 10, no. 9, pp. 1259–1261, September 1998.

[122] N. Chitica, J. Daleiden, M. Strassner, and K. Streubel, "Monolithic, InP based tunable filter with 10 nm bandwidth for optical data interconnects in the 1550 nm band," *IEEE Photonics Technology Letters*, vol. 11, no. 5, pp. 584–586, May 1999.

[123] M. Strassner, J. Daleiden, N. Chitica, D. Keiper, B. Stalnacke, S. Greek, and K. Hjort, "III-V semiconductor material for tunable fabry-pérot filters for coarse and dense WDM systems," *Sensors and Actuators*, vol. 85, pp. 249–255, 2000.

[124] M. Aziz, J. Pfeiffer, M. Wohlfarth, K. Lubers, S. Wu, and P. Meissner, "A new and simple tunable two-chip microcavity for filter applications in WDM systems," *IEEE Photonics Technology Letters*, vol. 12, no. 11, pp. 1522–1524, November 2000.

[125] C.F.R. Mateus, C.-H. Chang, L. Chrostowski, S. Yang, D. Sun AndR. Pathak, and C. J. Chang-Hasnain, "Widely tunable torsional optical filter," *IEEE Photonics Technology Letters*, vol. 14, no. 6, pp. 819–821, June 2002.

[126] H. Halbritter, M. Aziz, F. Riemenschneider, and P. Meissner, "Electrothermally tunable two-chip optical filter with very low-cost and simple concept," *Electronics Letters*, vol. 38, no. 20, pp. 1201–1202, September 2002.

[127] J. Daleiden, V. Rangelov, S. Irmer, F. Römer, M. Strassner, C. Prott, A. Tarraf, and H. Hillmer, "Record tuning of InP-based multiple air-gap MOEMS filter," *Electronics Letters*, vol. 21, no. 21, October 2002.

[128] M. Strassner, C. Luber, A. Tarraf, and N. Chitica, "Widely tunable-constant bandwidth monolithic fabry-pérot filter with a stable cavity design for WDM systems," *IEEE Photonics Technology Letters*, vol. 14, no. 11, pp. 1548–1550, November 2002.

[129] N. Kanbara, K. Suzuki, T. Watanabe, and H. Iwaoka, "Precisely tunable fabry-pérot filter for optical communications," *IEEE/LEOS proceedings of the International Conference on Optical MEMS*, pp. 173–174, 2002.

[130] S. Irmer, K. Alex, J. Daleiden, I. Kommallein, M. Oliveira, F. Römer, A. Tarraf, and H. Hillmer, "Surface micromachined optical low-cost all-air-gap filters based on stress-optimized Si_3N_4 layers," *IOP, Journal of Micromechanics and Microengineering*, vol. 15, no. 4, pp. 867–872, April 2005.

[131] S.-S. Yun and J.-H. Lee, "A micromachined in-plane tunable optical filter using the thermo-optic effect of crystalline silicon," *IOP, Journal of Micromechanics and Microengineering*, vol. 13, no. 5, pp. 721–725, June 2003.

[132] F. Solomonsson, *Processing Technology For Long-Wavelength Vertical-Cavity Lasers*, Ph.D. thesis, Royal Institute of Technology, Sweden, 2001.

[133] H.W. Song, D.S. Song, I.Y. Han, C.K. Kim, H.Y. Ryu, and Y.H. Lee, "1.5μm vertical-cavity surface-emitting lasers utilising low loss $Al_xO_y/GaAs$ mirrors," *Electronics Letters*, vol. 35, no. 4, February 1999.

[134] J.-H. Baek, W.S. Han, H.K. Cho, B. Lee, and I.H. Choi, "Optically pumped continuous-wave operation of InAlGaAs/InAlAs/InP based 1.55μm vertical-cavity surface-emitting laser with SiO_2/TiO_2 dielectric mirror," *Electronics Letters*, vol. 35, no. 10, May 1999.

[135] A. Keating, A. Black, A. Karim, Y.-J Chiu, P. Abraham, C. Harder, E. Hu, and J. Bowers, "High-temperature optically pumped 1.55-μm VCSEL operating at 6 Gb/S," *IEEE Photonics Technology Letters*, vol. 12, no. 2, pp. 116–118, February 2000.

[136] N. Chitica and M. Strassner, "Room-temperature operation of photopumped monolithic InP vertical-cavity laser with two air-gap bragg reflectors," *Applied Physics Letters*, vol. 78, no. 25, pp. 3935–3937, June 2001.

[137] J. Geske, D. Leonard, M. H. MacDougal, B. Barnes, and J.E. Bowers, "CWDM vertical-cavity surface emitting laser array spanning 140 nm of the C, S, and L fiber transmission bands," *IEEE Photonics Technology Letters*, vol. 16, no. 5, pp. 1227–1229, May 2004.

[138] D.I. Babic, J.J. Dudley, K. Streubel, R.P. Mirin, J.E. Bowers, and E.L. Hu, "Double-fused 1.52-μm vertical-cavity lasers," *Applied Physics Letters*, vol. 66, no. 9, pp. 1030–1032, February 1995.

[139] D.I. Babic, K. Streubel, R.P. Mirin, N.M. Margalit, J.E. Bowers, E.L. Hu, D.E. Mars, L. Yang, and K. Carey, "Room-temperature continuous-wave operation of 1.54-μm vertical-cavity lasers," *IEEE Photonics Technology Letters*, vol. 7, no. 11, pp. 1225–1227, November 1995.

[140] N.M. Margalit, J. Piprek, S. Zhang, D.I. Babic, K. Streubel, R.P. Mirin, J.R. Wesselmann, J.E. Bowers, and E.L. Hu, "64 °C continuous-wave operation of 1.5-μm vertical-cavity laser," *Journal of Selected Topics in Quantum Electronics*, vol. 3, no. 2, pp. 359–365, April 1997.

[141] A. Syrbu, A. Mircea, A. Mereuta, A. Caliman, C.-A. Berseth, G. Suruceanu, V. Iakovlev, M. Achtenhagen, R. Rudra, and E. Kapon, "1.5-mW single mode operation of wafer-fused 1550-nm VCSELs," *IEEE Photonics Technology Letters*, vol. 16, no. 5, pp. 1230–1232, May 2004.

[142] A. Karim, A. Black, P. Abraham, D. Lofgreen, Y.J. Chiu, J. Piprek, and J.E. Bowers, "Superlattice barrier 1528-nm vertical-cavity laser with 85 °C continuous-wave operation," *IEEE Photonics Technology Letters*, vol. 12, no. 11, pp. 1438–1440, November 2000.

[143] K. Streubel, S. Rapp, J. Andre, and J. Wallin, "Room-temperature pulsed operation of 1.5-μm vertical cavity lasers with an InP-based bragg reflector," *IEEE Photonics Technology Letters*, vol. 8, no. 8, pp. 1121–1123, September 1996.

[144] Y. Ohiso, H. Okamoto, R. Iga, K. Kishi, K. Tateno, and C. Amano, "High performance of 1.55-μm buried-heterostructure vertical-cavity surface-emitting lasers," *IEEE Photonics Technology Letters*, vol. 13, no. 9, pp. 918–920, September 2001.

[145] D. Sun, W. Fan, P. Kner, T. Kageyama, R. Pathak, D. Zhang, and W. Yuen, "Sub-mA threshold 1.5-μm VCSELs with epitaxial and dielectric DBR mirrors," *IEEE Photonics Technology Letters*, vol. 15, no. 12, pp. 1677–1679, December 2003.

[146] C. Kazmierski, J.P. Debray, R. Madani, I. Sagnes, A. Ougazzaden, N. Bouadma, J. Etrillard, F. Alexandre, and M. Quillec, "+55 °C pulse lasing at 1.56μm of all-monolithic InGaAlAs/InP vertical cavity lasers," *Electronics Letters*, vol. 35, no. 10, May 1999.

[147] J. Boucart, C. Stark, F. Gaborit, A. Plais, N. Bouche, J.C. Remy, J. Bonnet-Gamard, L. Goldstein, C. Fortin, D. Carpentier, P. Salet, F. Brillouet, and J. Jacquet, "Metamorphic DBR and tunnel-junction injection: A CW RT monolithic long-wavelength VCSEL," *IEEE Journal of Selected Topics in Quantum Electronics*, vol. 5, no. 3, pp. 520–529, May/June 1999.

[148] J. Boucart, C. Starck, F. Gaborit, A. Plais, N. Bouche, E. Derouin, L. Goldstein, C. Fortin, D. Carpentier, and J. Jacquet, "1-mW CW-RT monolithic VCSEL at 1.55 μm," *IEEE Photonics Technology Letters*, vol. 11, no. 6, pp. 629–631, June 1999.

[149] W. Yuen, G.S. Li, R.F. Nabiev, J. Boucart, P. Kner, R.J. Stone, D. Zhang, M. Beaudoin, T. Zheng, C. He, K. Yu, M. Jansen, D.P. Worland, and C.J. Chang-Hasnain, "High-performance 1.6μm single-epitaxy top-emitting VCSEL," *Electronics Letters*, vol. 36, no. 13, pp. 1121–1123, June 2000.

[150] E. Hall, S. Nakagawa, G. Almuneau, J.K. Kim, and L.A. Coldren, "Room-temperature, CW operation of lattice-matched long-wavelength VCSELs," *Electronics Letters*, vol. 36, no. 17, August 2000.

[151] O.-K. Kwon, B.-S. Yoo, J.-H. Shin, J.-H. Baek, and B. Lee, "Pulse operation and threshold characteristics of 1.55-μm InAlGaAs-InAlAs VCSELs," *IEEE Photonics Technology Letters*, vol. 12, no. 9, pp. 1132–1134, September 2000.

[152] A. Syrbu, V. Iakovlev, G. Suruceanu, A. Caliman, A. Rudra, A. Mircea, A. Mereuta, S. Tadeoni, C. Berseth, M. Achtenhagen, J. Boucart, and E. Kapon, "1.55-μm optically pumped wafer-fused tunable VCSELs with 32-nm tuning range," *IEEE Photonics Technology Letters*, vol. 16, no. 9, pp. 1991–1993, September 2004.

[153] J. Boucart, R. Pathak, D. Zhang, M. Beaudoin, P. Kner, D. Sun, R. Stone, R.F. Nabiev, and W. Yuen, "Long wavelength MEMS tunable VCSEL with InP-InAlGaAs bottom DBR," *IEEE Photonics Technology Letters*, vol. 15, no. 9, pp. 1186–1188, September 2003.

[154] P.Kner, T. Kageyama, J. Boucart, R. Stone, D. Sun, R.F. Nabiev, R Pathak, and W. Yuen, "A long-wavelength MEMS tunable VCSEL incorporating a tunnel junction," *IEEE Photonics Technology Letters*, vol. 15, no. 9, pp. 1183–1185, September 2003.

[155] M.Y. Li, W. Yuen, G.S. Li, and C.J. Chang-Hasnain, "Top-emitting micromechanical VCSEL with a 31.6-nm tuning range," *IEEE Photonics Technology Letters*, vol. 10, no. 1, pp. 18–20, January 1998.

[156] D. Sun, W. Fan, P. Kner, J. Boucart, T. Kageyama, D. Zhang, R. Phatak, R. Nabiev, and W. Yuen, "Long wavelength-tunable VCSELs with optimized MEMS bridge tuning structure," *IEEE Photonics Technology Letters*, vol. 16, no. 3, pp. 714–716, March 2004.

[157] C.J. Chang-Hasnain, "Tunable VCSEL," *IEEE Journal on Selected Topics in Quantum Electronics*, vol. 6, no. 6, pp. 978–987, November-December 2000.

Appendix A

State of the art: detailed description

Microcavity devices for the optical communications combine the advantages for mechanics and optics resulting from the miniaturization. These advantages are difficult to understand if we consider our macroworld only. In this macroworld we are living in, machine dimensions span from the sub-mm range (parts in precision mechanisms) to the km range (large electron accelerating rings). We can readily appreciate the advantages of miniaturization in silicon based microelectronics (e.g. microchips and electronic devices), which are involved in high speed personal computers, novel digital electronics (e.g. television, hi-fi electronics, digital cameras, etc.). The smaller the devices, the faster the computers and the smaller the equipment. In this case, the microcomponents are part of a system whose main functionality remains unchanged. A digital camera still delivers pictures, like the one 30 years ago did. However, if we consider the quality, the price, the size, and the impact on our daily life quality, we appreciate the added value and performance.

Passive consumer acceptance is then challenged when the miniaturization is applied to a mechanical system. Thus, it is difficult to imagine that somebody can drive to work with a car of $2\,\mu$m length. Nowadays, micromechanics are used as microcomponents in macrosystems (e.g. air-bag sensors, environmental gas detectors and metrology). However, micromechanics exhibit huge advantages or even some novel functionality when compared to the well known macromechanics. Thus, downscaling the dimensions linearly results in a nonlinear changing of the forces impacting the system [23]. To see this, consider a microbridge of $100\,\mu$m length, $0.5\,\mu$m thickness and $10\,\mu$m width. In micromechanics, this bridge is considered to be a robust free hanging system. Scaling up this system to the macroworld dimensions (e.g. meters), a bridge of 1000 m length, 5 m thickness, and 100 m width is obtained. Such a bridge is unstable and will collapse. Therefore, many actuated systems (e.g. tunable VCSEL and FPF filters) can be implemented only by using micromechanics and microcomponents. Thus, in recent years, MEMS and MOEMS became very interesting for a wide range of systems integration [115, 116]. On one hand, they reveal the same advantages as microelectronics (e.g. low-cost mass production, low power consumption and small size) and

on the other hand, they benefit from the novel effects of the miniaturization. In this thesis, the focus is on implementing micromechanically tunable microdevices such as VCSELs, FPFs and PIN photodetectors. These components are the core of the new dynamic DWDM systems. In the following, a summary of the devices which have been implemented in the recent years will be presented.

A.1 Fabry-Pérot filter

Several approaches dealing with non tunable and tunable Fabry-Pérot filters have been previously published. Even though the filter is a simple device, its tunability is still a major technological challenge. However, tunable filters are attractive since they present a low-cost solution for dynamic DWDM systems.

Based on a GaAs/AlAs bottom DBR and an Au/SiN_xH_y/GaAs top movable membrane, Larson et. al. [10] presented a tunability of 32 nm by a 14 V tuning voltage at a central wavelength of 932 nm. The membrane is actuated electrostatically and the FWHM of the filter resonance is 3 nm. Vail et. al. [117] show a tunability of 70 nm by a 5 V tuning voltage. The top movable DBR is implemented by a cantilever, whereas the central wavelength is 950 nm. A tunable filter, based on Si/SiO_2 DBRs with 60 nm tuning range is demonstrated by Tran et. al. [118] for a 1.517 μm central wavelength. The FWHM of the filter characteristic is 3.2 nm. A GaAs/AlAs two-chip concept filter with a FSR of 46.7 nm, a FWHM of 1.2 nm, an electrostatic tuning range of 103 nm (by a tuning voltage of 35 V), and a 1.517 μm central wavelength has been presented by Peerlings et. al. [119]. Tayebati et. al. [120] show a GaAlAs/AlO_x air-gap based filter with 59 nm tuning range at 50 V tuning voltage (FWHM=0.5 nm) and 83 nm tuning range at 25 V tuning voltage (FWHM=2.0 nm). However, multimode operation is observed in this case. Using a Fabry-Pérot filter with a stable half symmetric cavity design [12], the same author shows a tunability of 70 nm by a tuning voltage of 14 V. The filter consists of two SiO_2/TiO_2 DBRs separated by an air-gap cavity. The radius of curvature of the top membrane is around 310 μm. The FWHM of the filter characteristics is 0.27 nm. Spisser et. al. [121] demonstrate for the first time a tunable filter based on InP/air DBRs. The filter operates at 1.55 μm and exhibits a tunability of 62 nm by a 14 V tuning voltage. A FWHM of 0.4 nm is observed over 40 nm tuning range. A hybrid Si/SiO_2 and InGaAsP based tunable filter is presented by Chitica et. al. [122]. A tuning range of 40 nm has been reached by applying 40 V tuning voltage. In this case, the FWHM is 10 nm. A tunability of 0.3Å/V^2 of a InP/air based filter is demonstrated by Strassner et. al. [123]. Here, the mechanical properties (like stress) have been intensively studied. Aziz et. al. [124] present a tunability of over 20 nm by a tuning voltage of 100 V. The two chip based filter consists of two Si_3N_4/SiO_2 dielectric DBRs and the FWHM of the filter characteristic is below 0.1 nm. An AlGaAs cantilever based filter with a tuning range of over 100 nm by a 18 V-20 V tuning voltage is demonstrated by Mateus et. al. [125]. Halbritter et. al. [126] show an electrothermally tuned filter with a tuning range of over 34 nm by using a Si_3N_4/SiO_2 top DBR membrane. The filter exhibits a FWHM of 0.16 nm. An

InP/air-gap based filter with 112 nm tuning range and 3.5 nm FWHM is achieved by Daleiden et. al. [127]. The tuning voltage is only 5 V. Strassner et. al. [128] demonstrate an electrostatic tuning to longer wavelengths by an InP/air based filter. The filter characteristic remains unchanged over the 65 nm tuning range. The FWHM is 4.3 nm, whereas the tuning voltage is 21 V. The author of this thesis [103] presents a low-cost solution of an electrothermally tuned filter with Si_3N_4/SiO_2 dielectric DBRs. The tunability is 15 nm / mA with a tuning range of 15 nm. The FWHM as predicted by theoretical model calculation 8 nm. A silicon based filter presented by Kanbara et. al. [129] exhibits a FWHM of 0.5 nm and an FSR of 35 nm. In this case, the tuning range of 30 nm is reached by a tuning voltage of 29 V. Irmer et. al. [9] present a continuously widely tunable InP/air based filter with 140 nm tuning range. The tuning voltage is 3.2 V, whereas the FWHM is between 3 nm and 5 nm. The same author recently presented [130] a non tunable low-cost all dielectric air-gap filter with 1.5 nm FWHM. Yun et. al. [131] present a tunable in-plane Si/air filter with 9 nm thermooptical tuning range by a tuning temperature of 392 K. A FWHM of 1.1 nm is achieved. Hohlfeld et. al. [11] present a tunable filter based on the thermooptical effect. The filter consists of a silicon cavity and two Si_3N_4/SiO_2 DBRs and shows a tunability of 3.5 nm and a FWHM of 1.19 nm.

A.2 Vertical cavity surface emitting laser

Simply spoken, a vertical cavity surface emitting laser device is a light emitting active region embedded vertically between two DBRs. However, this approximation is in fact extremely simplistic when we consider all the optical and the mechanical aspects leading to a lasing in a VCSEL. The main feature distinguishing a VCSEL from an edge emitting laser is the fact that the laser oscillation as well as the laser light emission occur in a direction perpendicular to the wafer surface. This feature enables a better design of the emission pattern (usually a circular shape) resulting in low light divergence and efficient fiber coupling. Further advantages of a VCSEL are the wafer scale batch fabrication, the in-plane characterization, the simple packaging and the high yield of the device. Thus, compared to the edge emitting lasers, VCSELs present a low-cost solution for optical communications.

In this case, a single longitudinal mode operation is needed. This can be easily obtained due to the small overall cavity length (some few μm), typically of the same order of the emission wavelength. This fact results in a small gain region leading to smaller drive currents. Even though higher differential resistance is mostly the consequence of a voltage drop over the DBRs, the wall-plug efficiency of a VCSEL is much higher than that of any other semiconductor laser device[1] [132]. However, due to the short active region length, the stimulated light can only benefit from a small

[1] When discussing the efficiency of the whole laser, the expression wall-plug efficiency is often used. The wall-plug efficiency equals the output light energy divided by the electrical energy into the wall plug.

gain path. Therefore, very high reflective DBRs are needed and stringent optical and mechanical requirements for the active material should be achieved.

Since the first demonstration of a VCSEL operation by Soda et al. in 1979 [27], countless publications have documented the successful research of several groups. Absolutely dominating are VCSELs for the short wavelength range below 1 μm. As the interest in DWDM systems increases, VCSELs for the long haul wavelength range (1.3 μm and 1.5 μm) became highly desired. However, the technological implementation of such devices is still a major challenge due to the material properties at this wavelengths. Until now, several optically and electrically pumped, non tunable and tunable VCSELs for the 1.55 μm range have been reported. Note, that optically pumped non tunable devices are easier to implement compared to the electrically pumped tunable ones, since no micromechanics and no electrical confinements are used.

Song et. al. [133] present a wafer bonded VCSEL with a InGaAs/InGaAsP QWs system. The top and bottom DBRs consist of a GaAs/Al_xO_y and GaAs/AlAs multilayers, respectively. An optical threshold pump power of 1.4 mW at RT corresponding to a threshold current of 1.2 mA for a 5 μm aperture device, leads to a cw operation with a line width below 0.2 nm. An optically cw pumped VCSEL with hybrid DBRs is presented by Baek et. al. [134]. The device consists mainly of a periodic gain structure with 27 InGaAs/InAlGaAs QWs located in an active region embedded between a InAlAs/InAlGaAs bottom DBR and a dielectric TiO_2/SiO_2 top DBR. A minimum threshold pump power of 17 mW at 220 K is observed. This corresponds to a calculated threshold power density of 3.4 kW/cm^2. The line width of the laser characteristic at 1553 nm is below 0.6 nm and a maximum power of above 100 μW is achieved. Keating et. al. fabricate a wafer fused VCSEL with InGaAsP based QWs and GaAs/AlAs DBRs [135]. The device exhibits an output power of 1.95 mW at RT and at 1547 nm emission wavelength with a SMSR of 61dB. A novel all air-gap monolithically grown InP based VCSEL is presented by Chitica et. al. [136]. The cavity comprising the GaInAsP QWs is embedded between to InP/air DBRs. The threshold is reached at RT by an optical pump power density of 370 W / cm^2. A maximum output power of 110 μW and a cw operation up to 32 °C are reached. Recently, Geske et. al. presented a VCSEL array with 140 nm spanning emission wavelength range with 20 nm channel spacing [137]. The wafer bonded device is optically pumped and shows a cw operation above 65°C and a 36 dB SMSR as well as an average output power of -3 dB.

Many approaches towards electrically pumped non tunable wafer fused VCSELs have been published. Babic et. al. [138] demonstrate a wafer fused InGaAsP based VCSEL with two AlAs/GaAs DBRs. The threshold current density is in the order of 3 kA / cm^2 at 1.52 μm emission wavelength. A 12 mA threshold current characterizes laser sizes from 9 to 60 μm, whereby a single mode operation could be observed for the 9 μm VCSEL only. The same author later presents a double fused VCSEL operating continuously at RT and emitting at 1.54 μm [139]. The active region containing the InGaAsP is located between a top AlGaAs/GaAs DBR and a bottom AlAs/GaAs one. Devices with aperture sizes between 8 and 20 μm are fabricated and operate

continuously at RT. The 8 μm device possesses the lowest threshold current of 2.3 mA and a maximum output power of approximately 10 μW. A double fused VCSEL, with two AlGaAs/GaAs DBRs and an InGaAsP/InP active region is reported by Margalit et. al. [140]. The device operates in a cw and pulsed mode up to 64 °C and 100 °C, respectively. The lowest threshold current at RT is measured to be 0.8 mA and the maximum output power is 1 mW at 15 °C. Syrbu et. al. [141] demonstrate a single mode wafer fused 1.55 μm VCSEL exhibiting 1.5 mW output power at RT and a SMSR of 30 dB. A double fused 1.528 μm VCSEL with cw operation up to 85 °C and a maximum output power of 0.65 mW at RT is presented by Karim et. al. [142].

Electrically pumped non tunable VCSEL with hybrid DBRs are reported by several groups. K. Streubel and co-workers [143] present a 1.55 μm VCSEL with a bottom GaInAsP/InP DBR and a Si/SiO_2 top DBR. The GaInAsP based device shows a pulsed operation within a temperature range between −160 °C to +43 °C, while a cw operation was observed up to −25 °C only. Ortsiefer et. al. [15] fabricate an InGaAlAs based 1.55 μmVCSEL with 1.6 mW output power. The bottom and top DBRs are implemented by a InGaAlAs/InAlAs and MgF_2/a-Si multilayers, respectively. A low resistance of 70 Ω assures a threshold current of 4 mA. A double fused 1.55 μm VCSEL with InGaAsP QWs between a bottom GaAs/AlAs and a combined SiO_2/TiO_2-InP/InGaAsP top DBRs is presented by Ohiso et. al. [144]. Using different device aperture sizes, a maximum output power of 2.1 mW and a low threshold current of 380 μA have been demonstrated in a cw operation at RT. Sun et. al. [145] implement a cw 1.55 μm VCSEL device with a minimum threshold current of 0.8 mA at RT. The device consists of an InAlGaAs QWs stack and an InAlGaAs/InAlAs bottom DBR as well as TiO_2/SiO_2 top DBR.

Monolithically grown electrically pumped VCSELs for commercial purposes have gained importance since they enable a technological batch processing and an in-plane characterization. Furthermore, such devices are electrically driven and thus suitable for system integration. Over the past years, several such devices were presented by many groups. Kazmierski et. al. [146] present a monolithic grown InGaAlAs based VCSEL with InGaAlAs/InAlAs DBRs. A pulse operation at 1.56 μm and up to +55 °C is obtained. A device with a metamorphic bottom InP/InGaAsP DBR and GaAs/AlAs top one as well as 1 mW cw output power at RT is presented by Boucart et. al. [147,148]. Yuen et. al. [149] demonstrated a cw operation up to +55 °C with 0.45 mW output power at RT. The active region containing the InGaAs QWs is sandwiched between the InAlGaAs/InAlAs bottom DBR and the metamorphic AlGaAs/GaAs top DBR. A tunnel junction VCSEL with InGaAs QWs and AlGaAsSb/AlAsSb DBRs has been fabricated by Hall et. al. [150]. A maximum output power of 100 μW and a current threshold of 6.2 mA (1.97 kA / cm^2 current density) at RT is reached. Kwon et. al. [151] implemented a fully monolithic VCSEL with InAlGaAs/InAlAs DBRs. A minimum threshold current density of 2.93 kA / cm^2 at 1.57 μm is observed.

However, tunable optically and electrically pumped micromachined VCSELs for the long haul wavelength range are very rare, due to the undesirable side effects generated

from the micromachining process (e.g. stress and buckling). Vakhshoori et. al. [13] presented a 1.55 μm tunable cw VCSEL with 2 mW output power and 50 nm tuning range. The novelty of this work was the implementation of a stable resonator by a curved top DBR with a ROC of 300 μm. The tuning occurs electrostatically. However, the authors did not reveal either the material system nor the technological implementation details of the curved mirrors. The author of this thesis [105] published an optically tunable two chip 1.55 μm VCSEL with a curved top dielectric DBR. The lower part of the device consists of a GaInAsP based active region and an InP/InGaAsP bottom DBR. The curvature design of the SiN_x/SiO_2 top DBR is described in detail. A tuning range of 26 nm, a maximum output power of 400 μW, a SMSR of 57 dBm and a FSR of 47 nm are reached. The tuning occurs by a thermal actuation of the micromachined top DBR. A wafer fused optically pumped 1.55 μm tunable InAlGaAs based VCSEL with 2 mW maximum output power with a power variation less than 1.5 dB across the 32 nm tuning and a SMSR higher than 30 dB is demonstrated by Syrbu et. al. [152]. The top and Bottom DBRs are fabricated using multilayers of AlGaAs and GaAs.

Recently, a few publications reporting progress in electrically pumped tunable VCSEL technology have appeared. Boucart et. al. [153] implemented a monolithically InAlGaAs based 1.55 μm VCSEL with InP/InAlGaAs and a movable GaAs/AlGaAs bottom and top DBRs, respectively. The device operates up to temperatures exceeding +75 °C and shows 0.9 mW output power at RT. The tuning range is 17 nm, while the SMSR exceeds 30 dB. A tunable version of the VCSEL structure described in [149] is fabricated by Kner et. al. [154]. The electrostatically tunable top DBR is implemented by a cantilever according to [155]. The VCSEL shows an output power higher than 0.28 mW over 10 nm tuning range and a threshold current lower than 1 mA. The electrically pumped tunable VCSEL described by Sun et. al. [156] consists of InAlGaAs QWs between a InAlGaAs bottom DBR and a movable AlGaAs/GaAs top one. The electrostatic actuation of the top membrane delivers 22 nm tuning range and 1.3 mW output power in cw operation at +15 °C. Maute et. al. [14] produced an electrically tunable VCSEL, whose active region has already been described in [15]. The bottom mirror consists of CaF_2/a-Si multilayer and gold, the top movable mirror is a doped GaAs/AlGaAs DBR. The tuning of the two-chip [16] based device is done electrothermally. The device shows a single mode operation across 30 nm tuning with a SMSR better than 30 dB and a maximum output power of 76 μW. By the same technological implementation process, Riemenschneider et. al. [17] increased the tunability to 40 nm and the output power to 100 μW. Furthermore, an overview of VCSEL tunability is presented in [157].

Appendix B

Diagram supplements

B.1 PECVD technological investigation

Table B.1: *The used abbreviation*

Abbreviation	Parameter	Unit
T_{dep}	Deposition temperature	$^{\circ}C$
n	Refractive index	
$\mathrm{Si}\,H_4$	2% $\mathrm{Si}\,H_4 - N_2$ flow	sccm
NH_3	NH_3 flow	sccm
p_{dep}	Deposition pressure	E^{-3} torr
DR	Deposition rate	$\mathrm{nm\,min^{-1}}$
σ	Bulk stress	MPa
σ_{er}	Bulk stress standard deviation	MPa
N_2O	N_2O flow	sccm

Table B.2: *The dependence of the silicon nitride refractive index, deposition rate and stress on the process temperature*

T_{dep}	n	DR	σ	σ_{er}
230	1.928	15.64	−100.8	31
290	1.968	14.43	−79.9	20
300	1.963	14.25	−11.3	39
320	1.984	13.94	−80	20

Table B.3: *The dependence of the silicon nitride refractive index, deposition rate and stress on the silane flow*

$SiH4$	n	DR	σ	σ_{er}
800	1.936	14.58	−94.9	31.6
900	1.958	14.47	−85	16.6
1000	1.974	14.51	−12.3	5.6
1100	1.99	14.5	−100.9	12.7
1200	2.004	14.41	−129	36.5

Table B.4: *The dependence of the silicon nitride refractive index, deposition rate and stress on the amonia flow*

NH_3	n	DR	σ	σ_{er}
15	2.018	13.86	-61	28.9
20	1.966	14.12	-76.7	11.5
25	1.932	13.6	-77.2	6.5
30	1.911	13.94	-198.6	0.66

Table B.5: *The dependence of the silicon nitride refractive index, deposition rate and stress on the process pressure*

p_{dep}	n	DR	σ	σ_{er}
0.5	1.928	12.52	$-$	$-$
0.65	1.966	14.12	$-76,7$	$11,5$
0.8	1.989	15.34	$-$	$-$
1.1	1.988	12.04	$307,36$	38
1.3	2.024	14.13	$-302,4$	$1,3$

Table B.6: *The dependence of the silicon dioxide refractive index, deposition rate and stress on the process temperature*

T_{dep}	n	DR	σ	σ_{er}
230	1.464	63.40	232.31	13.22
290	1.466	66.52	184.32	12.27
300	1.467	67.97	176.5	13.65
320	1.467	69.07	135.32	12.2

Table B.7: *The dependence of the silicon dioxide refractive index, deposition rate and stress on the silane flow*

NH_3	n	DR	σ	σ_{er}
400	1.468	66.82	164.7	15.4
430	1.472	67.52	197.4	16.3
460	1.472	68.94	166.2	14.6
520	1.487	70.72	83	2

Table B.8: *The dependence of the silicon dioxide refractive index, deposition rate and stress on the nitrous oxide flow*

N_2O	n	DR	σ	σ_{er}
630	1.479	68.32	194.2	11.93
670	1.469	68.8	140.4	16.51
750	1.473	67.5	163.7	20.9
850	1.471	66.30	187.9	1.2

Table B.9: *The dependence of the silicon dioxide refractive index, deposition rate and stress on the process pressure*

p_{dep}	n	DR	σ	σ_{er}
0.5	1.381	51.96	238.7	10.5
0.7	1.472	60.97	187.1	20
1	1.472	67.33	124	15.33
1.5	1.468	62.76	179.5	16.4
2	1.466	57.70	105.5	85.78

B.2 Stress investigations

Table B.10: *The dependence of the silicon nitride and silicon dioxide stress on the PECVD duty cycle of the plasma excitation frequencies (process temperature : 300 °C)*

Si_3N_4

Ψ	σ	σ_{er}
−1	856.56	31.11
0.25	187	19.16
0.428	59.33	48.19
0.454	−26.85	19.98
0.478	−52.74	24.97
0.5	−30.22	16.61
0.52	−20.72	26.21
0.538	−39.48	24.83
0.66	−124.72	7.689
1	−297.44	30.66

SiO_2

Ψ	σ	σ_{er}
−1	461.98	56.51
−0.09	222.40	19.56
0.25	284.52	12.24
0.538	258.80	45.11
0.612	309.15	39.09
0.666	249.17	0
0.707	252.90	15.88
0.818	175.98	34.60
1	517.94	21.02

Table B.11: *The dependence of the silicon nitride and silicon dioxide stress on the PECVD duty cycle of the plasma excitation frequencies (process temperature : 60 °C)*

Si_3N_4

Ψ	σ	σ_{er}
0.555	121.11	36.24
0.571	78.66	29.34
0.586	47.54	58.49
0.6	49.24	27.65
0.612	−36.25	77.23

SiO_2

Ψ	σ	σ_{er}
0.428	30.33	20
0.481	20.93	37
0.538	42.05	4.9
0.578	12.24	9.7
0.6	46.51	11.8
0.621	08.06	13.2
0.666	14.50	43.6

B.3 Stress impact on mechanical and optical properties

Table B.12: *The dependence of the cavity length of the FPFs on the suspension length l at different PECVD duty cycles ψ (Design IMA2)*

	$\Psi = -1$		$\Psi = -0.75$		$\Psi = -0.5$	
l	L_{cav}	$L_{cav,er}$	L_{cav}	$L_{cav,er}$	L_{cav}	$L_{cav,er}$
10	3.62367	0.04216	3.62367	0.04216	3.62367	0.04216
20	4.22467	0.0905	5.05875	0.93395	0.27775	0.07133
30	4.95933	0.07438	5.6844	0.4708	4.6685	0.06096
40	0.43033	0.02656	6.33233	0.0368	4.5305	1.87521
60	0.4315	0.02294	6.84526	0.6107	6.62425	0
80	0.4815	0.09938	8.38806	0.2261	7.39092	0.35823

	$\Psi = -0.25$		$\Psi = 0$		$\Psi = 0.25$	
l	L_{cav}	$L_{cav,er}$	L_{cav}	$L_{cav,er}$	L_{cav}	$L_{cav,er}$
10	0.13267	0.01358	0.09733	0.119	–	–
20	0.30767	0.0725	0.415	0	–	–
30	5.552	0.24747	7.20067	0.4135	9.597	0
40	5.98133	0.16359	7.63167	0.22719	10.248	0.12834
60	6.72758	0.03236	8.68478	0.08834	11.1	0.25795
80	7.94625	0.16996	9.86178	0.07094	12.837	0.70139

Table B.13: *The dependence of the cavity length of the FPFs on the suspension length l at different PECVD duty cycles ψ (Design IMA3)*

	$\Psi = -1$		$\Psi = -0.75$		$\Psi = -0.5$	
l	L_{cav}	$L_{cav,er}$	L_{cav}	$L_{cav,er}$	L_{cav}	$L_{cav,er}$
10	2.63933	0.12568	3.092	0.3225	3.02433	0.22813
20	2.48367	0.04464	2.86775	0.08136	3.02267	0.04479
30	2.35	0.0444	2.83125	0.01735	3.334	0.1465
40	2.262	0.08586	2.86975	0.01709	3.81433	0.0935
60	2.31767	0.04588	2.8455	0.03225	3.53833	0.37051

	$\Psi = -0.25$		$\Psi = 0$		$\Psi = 0.25$	
l	L_{cav}	$L_{cav,er}$	L_{cav}	$L_{cav,er}$	L_{cav}	$L_{cav,er}$
10	3.28967	0.09084	3.07367	0.0216	4.52467	1.09449
20	3.116	0.02762	3.11633	0.2308	3.55	0.05444
30	3.27467	0.05152	3.254	0.0115	5.25167	1.43386
40	3.418	0.01735	3.93267	0.017	5.76267	0.2092
60	3.18167	0.14272	4.15867	0.4896	5.43567	0.57239

Table B.14: *The dependence of the radius of curvature (ROC) of the FPF membranes on the suspensions length l at different PECVD duty cycles ψ (Design IMA2)*

	$\Psi = -1$		$\Psi = -0.75$		$\Psi = -0.5$	
l	ROC	ROC_{er}	ROC	ROC_{er}	ROC	ROC_{er}
10	2.718	0.03033	1.77	0.47765	−0.548	0.03271
20	1.454	0.05225	0.95	0.10794	−0.662	0.03114
30	1.148	0.0249	0.81	0.03808	1.042	0.07294
40	−0.758	0.01304	0.76	0.02916	0.876	0.19191
60	−0.93	0.02121	0.74333	0.00577	0.846	0.13465
80	−0.994	0.02302	0.824	0.12321	0.81	0.06892

	$\Psi = -0.25$		$\Psi = 0$		$\Psi = 0.25$	
l	ROC	ROC_{er}	ROC	ROC_{er}	ROC	ROC_{er}
10	−0, 734	0, 07765	−0, 95	0, 19391	–	–
20	−1, 124	0, 06656	−0, 87	0	–	–
30	0, 442	0, 0228	0, 28	0, 05745	0, 16	0
40	0, 432	0, 00837	0, 294	0, 03209	0, 11	0, 01732
60	0, 478	0, 02775	0, 304	0, 05459	0, 12333	0, 02887
80	0, 516	0, 0251	0, 302	0, 06611	0, 13	0, 03606

Table B.15: *The dependence of the radius of curvature (ROC) of the FPF membranes on the suspensions length l at different PECVD duty cycles ψ (Design IMA3)*

	$\Psi = -1$		$\Psi = -0.75$		$\Psi = -0.5$	
l	ROC	ROC_{er}	ROC	ROC_{er}	ROC	ROC_{er}
10	−2.85	0.16325	15.17667	–	2.83	0.43841
20	−2.226	0.46079	−1.964	6.80512	4.675	1.91626
30	−2.122	0.59116	−8.746	3.43705	2.445	0.22576
40	−1.802	0.48111	−3.468	1.339	0.2075	2.7831
60	−2.46	0.58991	−3.79143	3.41535	2.68667	0.27209

	$\Psi = -0.25$		$\Psi = 0$		$\Psi = 0.25$	
l	ROC	ROC_{er}	ROC	ROC_{er}	ROC	ROC_{er}
10	3.87333	1.29063	1.288	0.16193	0.18333	0.07506
20	7.25667	1.36676	2.05	0.34547	0.32	0.04
30	5.70333	0.41004	1.144	0.19616	0.22667	0.04042
40	1.99333	0.05508	0.67	0.09849	0.29	0.07
60	1.90333	0.13051	0.608	0.00837	0.22667	0.00577

Table B.16: *The dependence of the FWHM of the FPFs on the suspensions length l at different PECVD duty cycles ψ (Design IMA2)*

	$\Psi = -1$	$\Psi = -0.75$	$\Psi = -0.5$	$\Psi = -0.25$	$\Psi = 0$	$\Psi = 0.25$
l	$FWHM$	$FWHM$	$FWHM$	$FWHM$	$FWHM$	$FWHM$
10	16	14.25	45	45.75	27.75	–
20	17	23.25	33	56.25	31.5	–
30	25.75	27.75	34.25	12.5	27	64.25
40	30.25	17.75	17.75	30.75	5.25	5.75
60	25	12	8.75	20.5	2.25	28.75
80	62.25	9.5	30.75	20	1.5	24.25

Table B.17: *The dependence of the FWHM of the FPFs on the suspensions length l at different PECVD duty cycles ψ (Design IMA3)*

	$\Psi = -1$	$\Psi = -0.75$	$\Psi = -0.5$	$\Psi = -0.25$	$\Psi = 0$	$\Psi = 0.25$
l	$FWHM$	$FWHM$	$FWHM$	$FWHM$	$FWHM$	$FWHM$
10	–	21.5	14.75	7.75	6.75	33.75
20	–	17.5	9.25	24.75	5.25	44.25
30	–	5	10.25	14.75	5.25	33
40	–	25.5	5.5	10.5	8.25	36.25
60	23.5	22	17	15.25	2.75	26.5

Table B.18: *The dependence of the RW of the FPFs on the suspensions length l at different PECVD duty cycles ψ (Design IMA2 and IMA3)*

IMA2	$\Psi = -1$	$\Psi = -0.75$	$\Psi = -0.5$	$\Psi = -0.25$	$\Psi = 0$	$\Psi = 0.25$
l	RW	RW	RW	RW	RW	RW
10	1468.5	1503.75	1573.25	1550.5	1589.5	–
20	1504.5	1584	1535.25	1539.75	1595.75	–
30	1463.5	1468.25	1546.25	1506.75	1549	1504.5
40	1476	1487.5	1529	1566.25	1580.5	1521
60	1455.5	1463	1502	1496.75	1457.75	1521.25
80	1490.75	1524	1550.5	1535.25	1519	1517

IMA3	$\Psi = -1$	$\Psi = -0.75$	$\Psi = -0.5$	$\Psi = -0.25$	$\Psi = 0$	$\Psi = 0.25$
l	RW	RW	RW	RW	RW	RW
10	1556.75	1587.25	1544	1464	1464.25	1562.5
20	1450	1536.75	1488.5	1578.25	1546.75	1561.5
30	1649	1451.25	1570.25	1536.5	1556.25	1559.5
40	1573	1514.25	1481.75	1473.75	1572.75	1509.5
60	1476.5	1566.75	1576.25	1484.5	1546.25	1549.25

Appendix C

Technological process flow

C.1 Air-gap Fabry-Pérot filters

C.1.1 Design IMA2

Table C.1: *Process technology data of the air-gap filter implemented using the design IMA2*

Process step	Parameter	Time
1 Substrate cleaning		
RCA	$H_2SO_4 : H_2O_2$ (3:1), $T = 90°C$	30 min
RCA	$NH_3 : H_2O_2 : H_2O$ (1:1:5), $T = 60°C$	30 min
RCA	$HCl : H_2O_2 : H_2O$ (1:1:5), $T = 60°C$	30 min
2 Deposition of the bottom DBR, 5 periods		
SiO_2	2% SiH_4-N_2 (430 sccm)	
	N_2O (710 sccm)	
	pressure ($1E^{-3}$ torr)	
	HF power (20 W)	
	Ψ (1)	
	T (300$°C$)	
	0.25λ @ 1450 nm, $n_{SiO_2} = 1.469$	
Si_3N_4	2% SiH_4-N_2 (1000 sccm)	10 min 17 s
	NH_3 (20 sccm)	
	pressure ($0.65E^{-3}$ torr)	
	HF & LFpower (20 W)	
	Ψ (0.538)	
	T (300$°C$)	
	0.25λ @ 1450 nm, $n_{Si_3N_4} = 1.933$	

Table C.2: *Continuation*

3 Sacrificial layer		
"Metall"	TI35ES / 4000rpm	2 min
	pre-bake, $T = 90°C$	2 min
	Exposure	35 s
	Waiting	10 min
	Reversal bake, $T = 130°C$	4 min
	Flood exposure	65 s
	Development, AZ826	40 s
O_2 ashing	pressure (0.7 mbar), power (250W)	1 min
Long bake	$T = 130°C$	8 h
4 Deposition of the top DBR, 5.5 periods		
SiO_2	2% SiH_4-N_2 (430 sccm)	
	N_2O (710 sccm)	
	pressure ($1E^{-3}$ torr)	
	HF & LF power (20 W)	
	Ψ (0.481)	
	T ($60°C$)	
	0.25λ @ 1450 nm, $n_{SiO_2} = 1.407$	
Si_3N_4	2% SiH_4-N_2 (1500 sccm)	
	NH_3 (5 sccm)	
	pressure ($0.65E^{-3}$ torr)	
	LF power (20 W)	
	Ψ (variable)	
	T ($60°C$)	
	0.25λ @ 1450 nm, $n_{Si_3N_4} = 1.832$	

Table C.3: *Continuation*

5 Mesa etching		
"Mesa"	AZ1518 / 4000rpm	2 min
	pre-bake, $T = 90°C$	5 min
	Exposure	8.5 s
	Development, KOH 0.8%	45 s
O_2 ashing	pressure (0.7 mbar), power (50W)	2 min
RIE	CHF3 (10.5 sccm)	
Si_3N_4	Ar (15.3 sccm)	
	Power (140 W)	
	pressure ($0.035E^{-3}$ torr)	
	T ($12°C$)	
6 Removal of the sacrificial layer		
Underetching	pressure (0.7 mbar), power (250W)	38 min

C.1.2 Design IMA3

Table C.4: *Process technology data of the air-gap filter implemented using the design IMA3*

Process step	Parameter	Time
1 Substrate cleaning		
RCA	$H_2SO_4 : H_2O_2$ (3:1), $T = 90°C$	30 min
RCA	$NH_3 : H_2O_2 : H_2O$ (1:1:5), $T = 60°C$	30 min
RCA	$HCl : H_2O_2 : H_2O$ (1:1:5), $T = 60°C$	30 min
2 Deposition of the bottom DBR, 5 periods		
SiO_2	2% SiH_4-N_2 (430 sccm)	
	N_2O (710 sccm)	
	pressure ($1E^{-3}$ torr)	
	HF power (20 W)	
	Ψ (1)	
	T (300°C)	
	0.25λ @ 1450 nm, $n_{SiO_2} = 1.469$	
Si_3N_4	2% SiH_4-N_2 (1000 sccm)	10 min 17 s
	NH_3 (20 sccm)	
	pressure ($0.65E^{-3}$ torr)	
	HF & LFpower (20 W)	
	Ψ (0.538)	
	T (300°C)	
	0.25λ @ 1450 nm, $n_{Si_3N_4} = 1.933$	

Table C.5: *Continuation*

3 Sacrificial layer		
"Protection"	TI35ES / 4000rpm	2 min
	pre-bake, $T = 90°C$	2 min
	Exposure	35 s
	Waiting	10 min
	Reversal bake, $T = 130°C$	4 min
	Flood exposure	65 s
	Development, AZ826	40 s
O_2 ashing	pressure (0.7 mbar), power (250W)	1 min
Long bake	$T = 130°C$	8 h
4 Deposition of the top DBR, 5.5 periods		
SiO_2	2% SiH_4-N_2 (430 sccm)	
	N_2O (710 sccm)	
	pressure ($1E^{-3}$ torr)	
	HF & LF power (20 W)	
	Ψ (0.481)	
	T ($60°C$)	
	0.25λ @ 1450 nm, $n_{SiO_2} = 1.407$	
Si_3N_4	2% SiH_4-N_2 (1500 sccm)	
	NH_3 (5 sccm)	
	pressure ($0.65E^{-3}$ torr)	
	LF power (20 W)	
	Ψ (variable)	
	T ($60°C$)	
	0.25λ @ 1450 nm, $n_{\mathrm{Si}_3 N_4} = 1.832$	

Table C.6: *Continuation*

5 Mesa etching		
"Mesa"	AZ1518 / 4000rpm	2 min
	pre-bake, $T = 90°C$	5 min
	Exposure	8.5 s
	Development, KOH 0.8%	45 s
O_2 ashing	pressure (0.7 mbar), power (50W)	2 min
RIE	CHF3 (10.5 sccm)	
Si_3N_4	Ar (15.3 sccm)	
	Power (140 W)	
	pressure ($0.035E^{-3}$ torr)	
	T ($12°C$)	
6 Removal of the sacrificial layer		
Underetching	pressure (0.7 mbar), power (250W)	38 min

C.2 Process flow of the tunable Fabry-Pérot filter

Table C.7: *Process technology data of the tunable air-gap filter implemented using the design IMA2*

Process step	Parameter	Time
1 Substrate cleaning		
RCA	$H_2SO_4 : H_2O_2$ (3:1), $T = 90°C$	30 min
RCA	$NH_3 : H_2O_2 : H_2O$ (1:1:5), $T = 60°C$	30 min
RCA	$HCl : H_2O_2 : H_2O$ (1:1:5), $T = 60°C$	30 min
2 Deposition of the bottom DBR, 5 periods		
SiO_2	2% SiH_4-N_2 (430 sccm)	6 min 20 s
	N_2O (710 sccm)	
	pressure ($1E^{-3}$ torr)	
	HF & LF power (20 W)	
	Ψ (0.481)	
	T ($60°C$)	
	0.25λ @ 1400 nm, $n_{SiO_2} = 1.3$	
Si_3N_4	2% SiH_4-N_2 (1500 sccm)	10 min 17 s
	NH_3 (5 sccm)	
	pressure ($0.65E^{-3}$ torr)	
	HF power (20 W)	
	Ψ (1)	
	T ($60°C$)	
	0.25λ @ 1400 nm, $n_{Si_3N_4} = 1.7$	
3 Sacrificial layer		
"contacts"	AZ5214e / 3000rpm	1 min
	pre-bake, $T = 90°C$	1 min
	Exposure	12 s
	Reversal bake, $T = 120°C$	2 min
	Flood exposure	12 s
	KOH, 0.8%	40 s
O_2 clean	pressure (0.7 mbar), power (250W)	1 min

Table C.8: *Continuation*

Process step	Parameter	Time
4 Deposition of the top DBR, 5.5 periods		
SiO_2	2% SiH_4-N_2 (430 sccm)	6 min 20 s
	N_2O (710 sccm)	
	pressure ($1E^{-3}$ torr)	
	HF & LF power (20 W)	
	Ψ (0.481)	
	T (60°C)	
	0.25λ @ 1400 nm, $n_{SiO_2} = 1.3$	
Si_3N_4	2% SiH_4-N_2 (1500 sccm)	10 min 17 s
	NH_3 (5 sccm)	
	pressure ($0.65E^{-3}$ torr)	
	HF power (20 W)	
	Ψ (1)	
	T (60°C)	
	0.25λ @ 1400 nm, $n_{Si_3N_4} = 1.7$	
5 Micro heaters		
Cr	100 nm	
"Heat"	AZ1518 / 4000rpm	1 min
	pre-bake, $T = 90°C$	5 min
	Exposure	5.5 s
	KOH, 0.8%	40 s
Cr etching	Cr etchant (7334) : H_2O (1:2)	1 min 33 s
PR removal	Aceton	2 min
"Test structure"	AZ1518 / 4000rpm	1 min
	pre-bake, $T = 90°C$	5 min
	Exposure	7 s
	KOH, 0.8%	40 s
Cr etching	Cr etchant (7334) : H_2O (1:2)	2 min 30 s

Table C.9: *Continuation*

Process step	Parameter	Time
6 MESA etching		
Si_3N_4 and SiO_2	Ar (5.1 sccm)	330 min
	CHF_3 (3.5 sccm)	
	pressure ($50E^{-3}$ torr)	
	DC bias (210 V)	
	RF level (30%)	
	T (12°C)	
7 Membrane release		
Polymer removal	pressure (0.7 mbar), power (50 W)	10 min
Underetching	pressure (0.7 mbar), power (250 W)	15 min

C.3 Process flow of the non tunable VCSEL

Table C.10: *Process parameters of the non tunable VCSEL*

Process step	Parameter	Time
2 Deposition of the bottom DBR, 12 periods		
SiO_2	2% SiH_4-N_2 (430 sccm)	
	N_2O (710 sccm)	
	pressure ($1E^{-3}$ torr)	
	HF power (20 W)	
	Ψ (1)	
	T (300°C)	
	0.25λ @ 1450 nm, $n_{SiO_2} = 1.469$	
Si_3N_4	2% SiH_4-N_2 (1000 sccm)	
	NH_3 (20 sccm)	
	pressure ($0.65E^{-3}$ torr)	
	HF & LF power (20 W)	
	Ψ (0.538)	
	T (300°C)	
	0.25λ @ 1450 nm, $n_{Si_3N_4} = 1.933$	
Ti/Au on the top of the DBR		
Ti/Au	50 nm /300 nm	
Bonding of the structure up side down by Indium		
Coating of sample borders with AZ4562		
InP etching	HCl (37%)	42 min
InGaAs etching	$FeCl_3$ (50 g+100 ml H_2O): H_2O [1 : 2]	30 s
PR removal	O_2 plasma, 400 W, 1.3 mbar, 0.7 sccm	30 min
Deposition of the top DBR, 12 periods, similar to the bottom DBR		

Appendix D

DBRs for the blue wavelength range

Table D.1: *Process flow of the short wavelength DBRs (TQ067 and TQ069)*

Process step	Parameter	Time
2 Deposition of DBR, 12.5 periods		
SiO_2	2% SiH_4-N_2 (430 sccm)	
	N_2O (710 sccm)	
	pressure ($1E^{-3}$ torr)	
	HF power (20 W)	
	Ψ (1)	
	T ($300°C$)	
	0.25λ @ 1450 nm, $n_{SiO_2} = 1.49$	
Si_3N_4	2% SiH_4-N_2 (1000 sccm)	
	NH_3 (20 sccm)	
	pressure ($0.65E^{-3}$ torr)	
	HF & LFpower (20 W)	
	Ψ (0.538)	
	T ($300°C$)	
	0.25λ @ 1450 nm, $n_{Si_3N_4} = 2.03$	

Appendix E

Abbreviations

Table E.1: *Abbreviations of the most frequently used expressions*

Abbreviation	**Description**
ASE	Amplified Spontaneous Emission
AMU	Automatic Matching Unit
AsH_3	Arsine
CAGR	Compound Annual Growth Rate
CDWDM	Coarse Dense Wavelength Division Multiplexing
CPD	Critical Point Drying
CWL	Central Wavelength
CW	Continuous Wave
DWDM	Dense Wavelength Division Multiplexing
DBR	Distributed Bragg Reflector
EDFA	Erbium Doped Fiber Amplifier
FPF	Fabry-Pérot Filter
FSR	Free Spectral Range
FWHM	Full Width at Half Maximum
GaAs	Gallium Arsenid
HF	High Frequency
ITU	International Telecommunications Union
InGaAsP	Indium Gallium Arsenid Phosphid
InP	Indium Phosphid
LF	Low Frequency
LPCVD	Liquid Phase Chemical Vapor Deposition
MAN	Metropolitan Area Networks
MEMS	Micro-Electro-Mechanical-System
MOEMS	Micro-Opto-Electro-Mechanical-System
MOVPE	Metal-Organic Vapor Phase Epitaxy
MFC	Mass Flow Controller
PECVD	Plasma Enhanced Chemical Vapor Deposition

Table E.1: Continuation

Abbreviation	Description
PH_3	Phosphine
PR	Photoresist
PL	Photoluminescence
PRI	Pulse Repetition Interval
QW	Quantum Well
ROC	Radius Of Curvature
RIE	Reactive Ion Etching
RT	Room Temperature
RW	Resonance Wavelength
SEM	Scanning Electron Microscope
SMSR	Side Modes Suppression Ratio
SiH_4	Silane
Si_3N_4	Silicon nitride
SiO_2	Silicon dioxide
Si	Silicon
T/R	Transmitter/Receiver
TMIn	Trimethylindium
TMGa	Trimethylgallium
VCSEL	Vertical Cavity Surface Emitting Laser
WDM	Wavelength Division Multiplexing
WWW	World Wide Web
WLI	White Light Interferometry

Appendix F

Stress impact on the ROC, L_{cav}, RW and FWHM

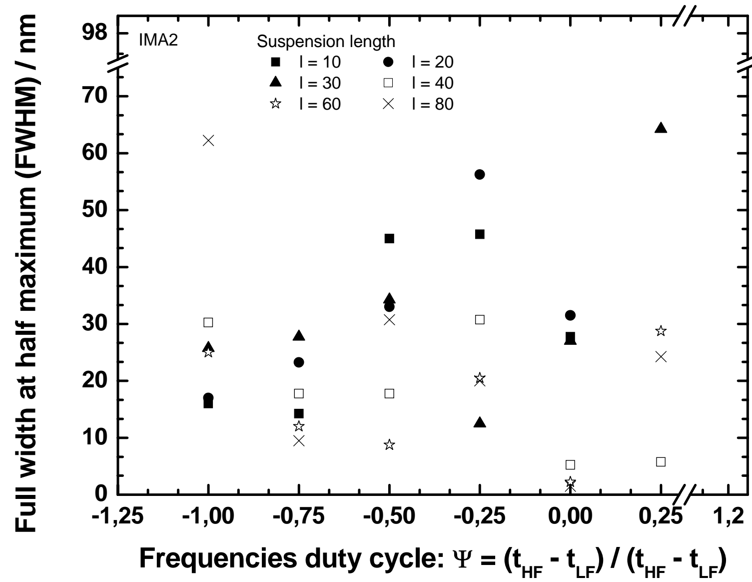

Figure F.1: *Dependence of the FWHM of the Fabry-Pérot filters on the duty cycle* Ψ *at different suspension lengths* l *for the design IMA2.*

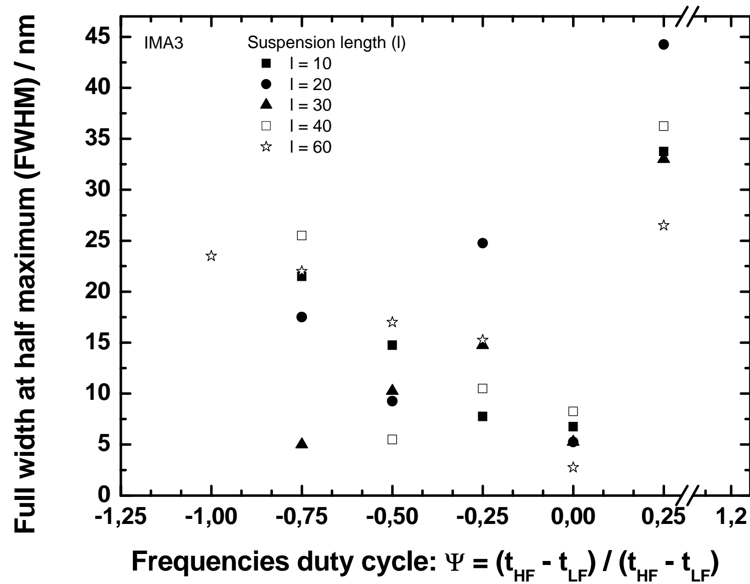

Figure F.2: *Dependence of the FWHM of the Fabry-Pérot filters on the duty cycle* Ψ *at different suspension lengths* l *for the design IMA3.*

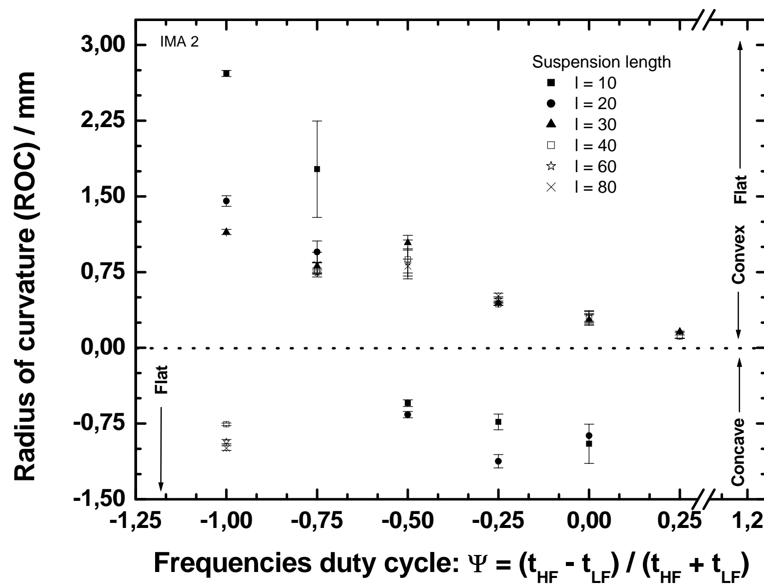

Figure F.3: *Dependence of the radius of curvature of the Fabry-Pérot filter membrane on the duty cycle* Ψ *at different suspension lengths* l *for the design IMA2.*

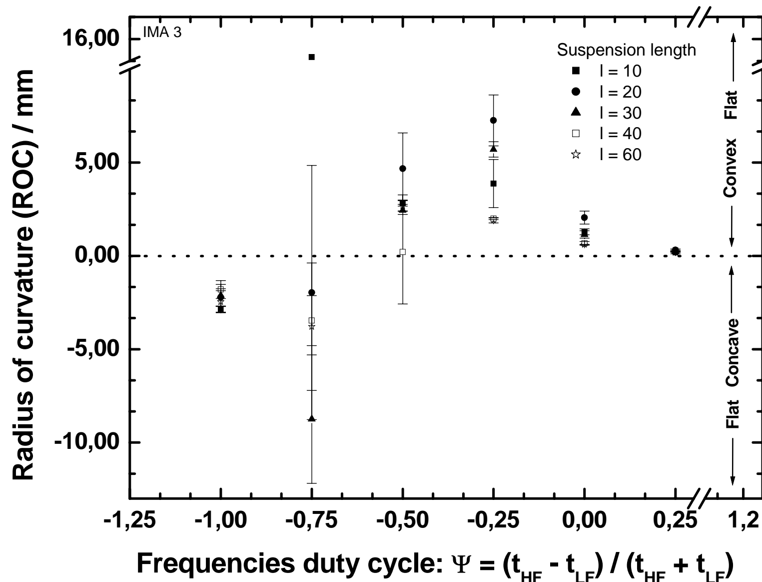

Figure F.4: *Dependence of the radius of curvature of the Fabry-Pérot filter membrane on the duty cycle* Ψ *at different suspension lengths* l *for the design IMA3.*

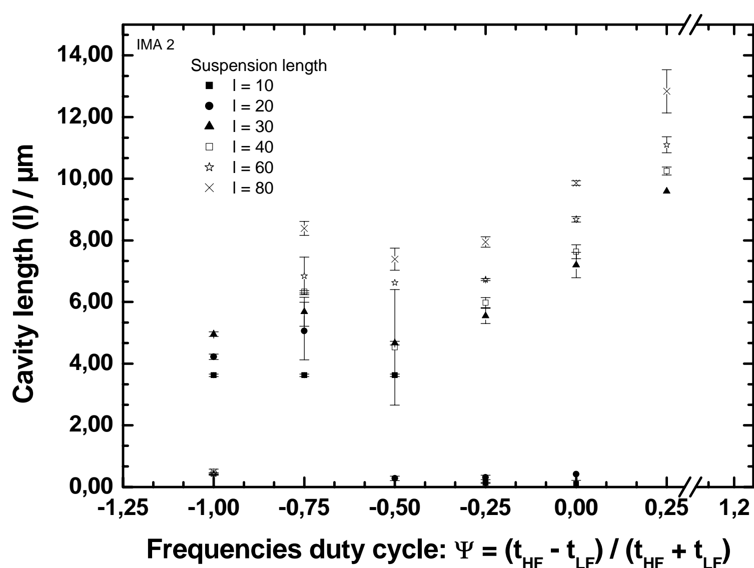

Figure F.5: *Dependence of the cavity length of the Fabry-Pérot filters on the duty cycle* Ψ *at different suspension lengths* l *for the design IMA2.*

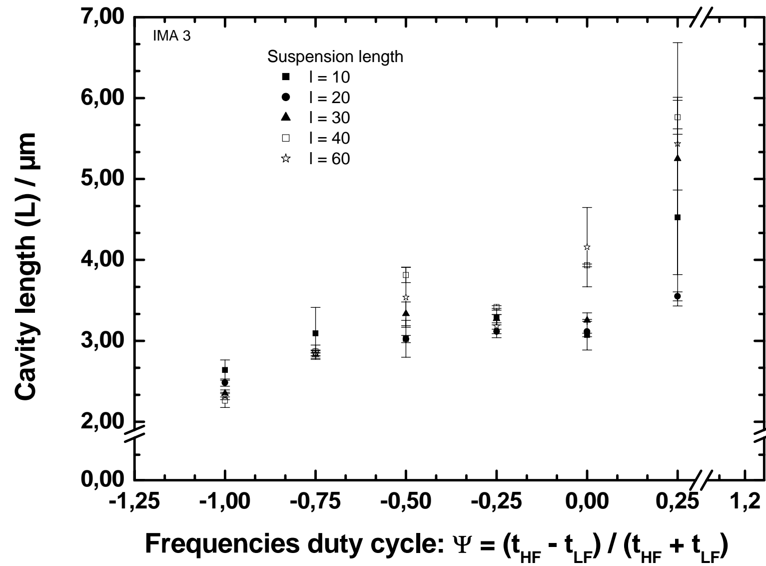

Figure F.6: *Dependence of the cavity length of the Fabry-Pérot filters on the duty cycle* Ψ *at different suspension lengths* l *for the design IMA3.*

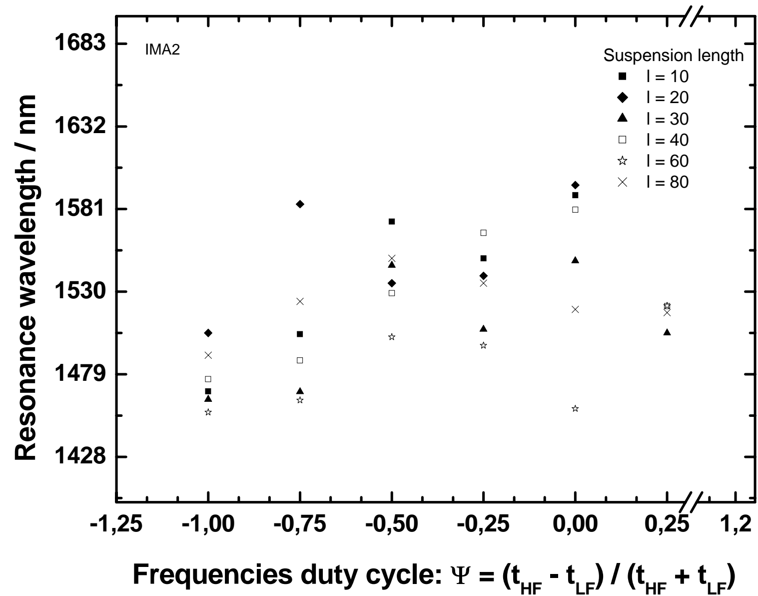

Figure F.7: *Dependence of the resonance wavelength of the Fabry-Pérot filters on the duty cycle* Ψ *at different suspension lengths* l *for the design IMA2.*

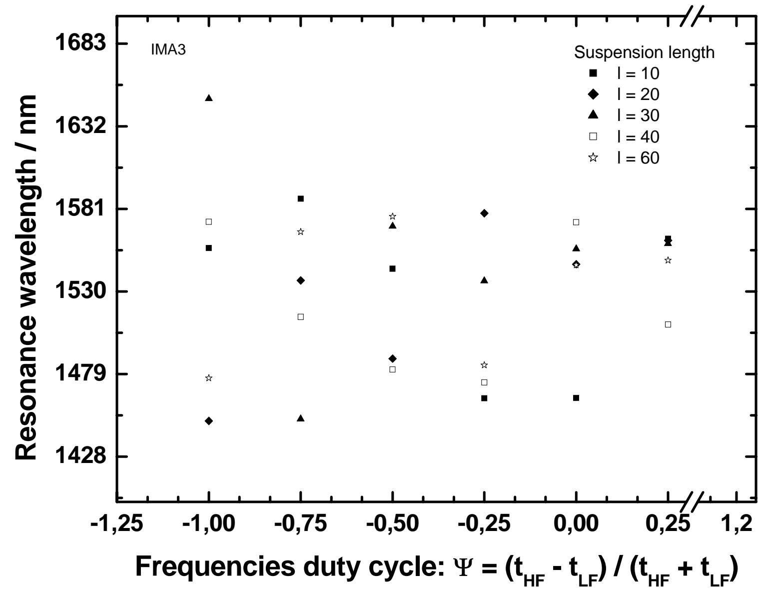

Figure F.8: *Dependence of the resonance wavelength of the Fabry-Pérot filters on the duty cycle* Ψ *at different suspension lengths* l *for the design IMA3.*